University of Southampton Research Repository

Copyright © and Moral Rights for this thesis and, where applicable, any accompanying data are retained by the author and/or other copyright owners. A copy can be downloaded for personal non-commercial research or study, without prior permission or charge. This thesis and the accompanying data cannot be reproduced or quoted extensively from without first obtaining permission in writing from the copyright holder/s. The content of the thesis and accompanying research data (where applicable) must not be changed in any way or sold commercially in any format or medium without the formal permission of the copyright holder/s.

When referring to this thesis and any accompanying data, full bibliographic details must be given, e.g.

Thesis: Author (Year of Submission) "Full thesis title", University of Southampton, name of the University Faculty or School or Department, PhD Thesis, pagination.

Data: Author (Year) Title. URI [dataset]

UNIVERSITY OF SOUTHAMPTON

Faculty of Engineering and Physical Sciences
School of Engineering
Computational Engineering and Design

Spatial variability of the dynamic response in periodic and non-homogeneous elastic media

by

Kevin Jose
MTech, BTech
ORCiD: 0000-0002-1268-4476

A thesis for the degree of
Doctor of Philosophy

June 2023

University of Southampton

Abstract

Faculty of Engineering and Physical Sciences
School of Engineering

Doctor of Philosophy

Spatial variability of the dynamic response in periodic and non-homogeneous elastic media

by Kevin Jose

The dynamics of elastic media and structures are of great practical interest due to their varied application in areas from ranging manufacturing to medicine. Surface structures like plates or shells or assemblies composed of constituent surface structures display a rich variety of spatial variability in their response to dynamic loading. In fact, the spatial variations observed in the dynamic response of vibrating plates, called Chladni's patterns, initiated the race to formulate the mathematics describing the dynamics of plates. Given the importance of structures such as beams, plates, and shells in practical applications, the spatial variability of their dynamic response is studied here in the context of (i) wave propagation in thin surface structures with randomly varying properties and (ii) modal vibrations of finite assemblies composed of beams, plates and shells.

In the first half of this work, the wave propagation of flexural waves in thin elastic plates and shells with non-uniform properties is studied. Particularly, the effect of spatially correlated random variation of thickness is considered. However, the results are shown to be generalisable to variations in other material and geometric properties. Initially, planar wavefronts undergo random focusing, and interesting branching structures, which lead to locations of large amplitudes, are observed in the path of propagation of the wavefront. A connection to the phenomenon called branched flows, hitherto unobserved in elasticity, is established. A scaling law is associated with the expected location of high amplitudes typified branched flows. In this work, it is established that this is observed in flexural waves supported by thin beams and shells too. This is despite the fact that markedly different equations of motion govern flexural elastic wave propagation in surface structures as compared to the other kinds of waves that show branched flows such as electromagnetic and shallow water waves. The emergence of branched flows and the associated scaling law is demonstrated theoretically from the analysis of partial, ordinary and stochastic differential equations. The phenomenon under question exists in the ray optics limit. Hence, the wave dynamics problem is approximated as a ray propagation problem using the WKB/eikonal approximation and solved numerically using a finite difference scheme. Finally, the full wave elastodynamics problem is solved using finite element simulations on high-performance clusters. This captures some of the subtleties, such as dispersion, that are missed by the ray approximation. The theoretical and numerical analyses are all found to be in excellent agreement. These results suggest a certain universality of branched flows in wave dynamics regardless of the physics involved.

Subsequently, the modal vibration of pillared plates is considered. These structures have attracted some interest as metamaterials. This has led to Bloch-Floquet-based analyses of their wave propagation characteristics. However, a study of the modal vibration of finite pillared plates is missing from the literature. There is a need to understand the modal vibration of such structures which can be understood as an abstraction of certain industrial assemblies such as fin-less heat exchangers. From numerical experiments, it is observed that small displacements of the based plate confer a spatial phase relationship to the tip deflection of the identical pillars, reminiscent of Chladni's patterns, within the degenerate frequency band corresponding to the resonance frequency of the pillars. This observation is leveraged to construct a Rayleigh quotient-based approximation of the modal vibration of such pillared plates. These are compared with finite element simulations which are found to be in excellent agreement. The use of the Hungarian algorithm, from combinatorics, to match modes from Rayleigh quotient-based approximation and those from FE simulations is discussed.

Finally, the modal vibration of tube-and-fin banks is studied. These are critical constituent elements of some heat exchangers. These structures are composed of numerous identical metallic tubes that are decorated with equally spaced thin metal plates or "fins". The fins increase the surface area available for heat exchange and are usually arranged perpendicular to the tube axes. Heat exchangers are often mounted onto engines that inevitably provide base excitation which excites lower vibrational modes of tube-and-fin banks. Therefore, understanding the modal vibration of tube-and-fin banks is of interest in designing heat exchangers. Based on some numerical experiments and physical arguments, it is ascertained that the lower vibrational mode shapes of tube-and-fin banks can be constructed as twisting and bending modes of some dynamically equivalent rod and beam respectively. Using this insight, Rayleigh quotient-based models of these mode shapes are set up which agree well with FE simulations. Moreover, these models are found to be very computationally efficient as compared to FE simulations. The role of the hexagonal and square lattice arrangement of tubes on fins is considered. The packaging of this proposed model as a graphical user interface for deployment in the industry is also discussed.

Contents

List of Figures ix

List of Tables xvii

Declaration of Authorship xix

Acknowledgements xxi

1 Introduction and literature survey 1

2 Flexural waves in random elastic plates: branched flows 9
- 2.1 Introduction and motivation 9
  - 2.1.1 Dynamics of elastic plates 10
  - 2.1.2 Elastic plates with non-uniform flexural stiffness 11
- 2.2 Branched flows in inhomogeneous media 12
- 2.3 Scaling from analysis of ray equations 15
- 2.4 Scaling from numerical ray integration 19
- 2.5 Remarks on generating the random field 22
- 2.6 Scaling from finite element simulation of wave elastodynamics 24
- 2.7 Wave propagation in uncorrelated vs correlated random media 31
- 2.8 Remarks on the FE simulations 36
- 2.9 Conclusions 37

3 Flexural waves in random elastic cylinders: branched flows 39
- 3.1 Introduction 39
- 3.2 Ray equations for radial displacement in thin cylindrical shells 43
  - 3.2.1 Ray equations from Pierce's formulation 43
  - 3.2.2 Ray equations from equations of motion due to Yu 47
- 3.3 Scaling law from the analysis of ray equations 54
- 3.4 Scaling law from numerical integration of ray equations 58
- 3.5 Scaling law from finite element elastodynamics 60
- 3.6 Remarks on numerical methods used 66
- 3.7 Conclusions 68

4 Standing waves in plates with periodically attached pillars: Chladni patterns 69
- 4.1 Analytical model of vibrational modes of a pillared plate 71
  - 4.1.1 Energy expressions for the base plate 72
  - 4.1.2 Energy expressions for pillar resonators 72

4.1.3 Global matrices of a pillared plate 74
4.2 Modal analysis using finite element simulations 75
4.3 Results and discussions 76
4.3.1 Modal Frequencies 76
4.3.2 Mode shapes (and their ordering) 76
4.3.3 Sonic crystals with "polarised" resonators 77
4.3.4 Density of states in the elastic plate-pillar system 79
4.3.5 Engineering Chladni vector fields 80
4.4 Conclusions 80

5 Long wave approximations for periodic structures: an industrial case study for tube-fin banks 83
5.1 Bending modes of a tube-fin assembly grouped on a rectangular lattice . 85
5.1.1 Discrete Model 86
5.1.2 Smeared Model 88
5.1.3 Comparison of the methods 90
5.1.4 Comparison with ANSYS FE predictions 91
5.2 Lower vibrational modes for tubes in a hexagonal lattice arrangement . 92
5.2.1 Bending type modes 94
5.2.2 Twisting type modes 94
5.2.3 Finite element simulations 97
5.3 Conclusions 99

6 Conclusions and future work 101

Appendix A Details of FEM simulations 103

Appendix B Tutorial: Application of Bloch's theorem in lattice vibrations 109
Appendix B.1 1D Lattice 110
Appendix B.1.1 Monatomic Chain 110
Appendix B.1.2 Diatomic chain 111
Appendix B.2 2D Lattice 113

References 117

List of Figures

2.1 Branched flows have been observed in many different physical contexts and length scales (L) Branched flow visible in Tohoku earthquake tsunami, 2011 [1]. (R) Branched flow in electron gas [2]. 13

2.2 (a) A schematic diagram of a piece of an exemplar thin non-uniform elastic plate under consideration. Thickness and its variation are greatly exaggerated for representational purposes. (b) The plate carries a pulse with a predominant wavelength $\lambda \ll L_c$, where L_c is the correlation length of randomness. (c) The randomness field $h(x, y)$ as a colormap, with $\langle h^2 \rangle = 9.06 \times 10^{-4}$, $L_c = 0.1$ m. 16

2.3 Evolution of rays in a plate with $\langle h^2 \rangle = 4.24 \times 10^{-4}$. Individual rays are plotted as translucent curves. Hence, caustics or focusing events, which correspond to overlapping rays, appear as regions of higher intensity. The location of first focusing is detected numerically (circular marker). . 20

2.4 Temporal evolution of the $k_y - y$ curve. The location of the first caustic is detected by finding the instance where the $k_y - y$ curve become multivalued (show in dark red here). 20

2.5 Scaling of the location of the first caustic location with $\langle h^2 \rangle$. The location of first focusing point (red translucent points) obtained from ray simulations. Mean $\langle \tilde{l}_f \rangle$ of each cluster is indicated by blue markers and a 2-standard-deviation width centered on the mean is indicated by a vertical blue line. The scaling $\langle \tilde{l}_f \rangle \sim \langle h^2 \rangle^{-1/3}$, indicated by the black dotted line on a semi-log plot, agrees extremely well with the simulations. . . . 21

2.6 Using the simulation results of $\tilde{L}_c = 1$ (red dots), and linear scaling with $\tilde{L}_c$, predictions are made for the other two cases (dotted lines) on a log-log plot. These predictions agree well with the scaling obtained from numerical ray integration (green and blue dots for $\tilde{L}_c = 0.7, 1.5$ respectively). 22

2.7 Scaling of $\langle l_f \rangle$ with wavelength λ. The location of the first caustic is independent of wavelength since even $\sim 200\%$ variation in wavelength shows no appreciable change in the expected location of the first caustic. 22

2.8 Examples of random fields $h(\tilde{x}, \tilde{y})$ generated for the simulations. Note the effect of change in correlation length $\tilde{L}_c$. In all 3 plots, $\sqrt{\langle h^2 \rangle} = 0.0066$ 23

2.9 A plot of excitation applied on left edge of the plate under consideration. The excitation consists of a one short single pulse near $t = 0$. The pulse consists of a sinusoid of angular frequency ω modulated by a Gaussian. Hence, the excitation is nearly 'monochromatic'. From the inset it can be seen that the pulse is an initial sharp excitation. 24

2.10 Fourier Transform of the pulse excitation show in Figure 2.9. The x-axis is frequency normalised with respect to the carrier frequency and the limits of the x-axis are governed by the Nyquist frequency of the signal. Note that most of the power in the signal is at or near the carrier frequency. 25

2.11 Spatio-temporal evolution of a Gaussian wave packet in a homogeneous plate. Transverse displacement of a thin homogeneous plate excited at the left edge by a pulse. Dispersion leading to a widening of the initially 'sharp' wavefront is apparent. The highest amplitude (marked by semi-transparent colored planes) at each time instant decreases monotonically. Branched flow is not observed. 25

2.12 Spatio-temporal evolution of a Gaussian wave packet. Transverse displacement of a thin inhomogeneous plate excited at the left edge by a pulse. The emergence of branches i.e rapid variation in wave amplitude in the $\tilde{y}$ direction, is seen after sufficient temporal evolution. The wave front, at different points of time, is zoomed into and shown on the right. The transparent plane marks the highest amplitude seen in a perfectly homogeneous plate, under the same excitation, at the corresponding instant of time. Branched flow disrupts the monotonically decreasing trend of highest amplitude. The randomness field describing the thickness has the standard deviation $\sqrt{\langle h^2 \rangle} = 0.0301$. 26

2.13 (Top) Plot of Scintillation Index (SI) corresponding to the case plotted in the bottom figure. It can clearly be seen that SI captures the variations in intensity (averaged along $\tilde{y}$). The location of the first focusing event is detected by finding the location (in the propagation direction) of the first significant peak in SI indicated by a circular marker in the plot. (Bottom) A plot of time-integrated intensity (normalised by mean along $\tilde{y}$). The emergence of focusing events is quite apparent. Note that the fluctuations are much higher than 5, but the scale is cut off at 5 to preserve detail in other regions. This corresponds to one of the simulations for $\tilde{L}_c = 1$, $\tilde{\lambda} = 0.1$, $\sqrt{\langle h^2 \rangle} = 0.0301$. 27

2.14 A plot of the location of first focusing events (red points). Mean $\langle \tilde{l}_f \rangle$ of each cluster is indicated by blue markers and a 2 standard deviation width centered on the mean is indicated by a vertical line. The scaling relationship of $\langle \tilde{l}_f \rangle \propto \langle h^2 \rangle^{-1/3}$, indicated by the black dotted line, agrees excellently with the simulations. 28

2.15 A plot of $\langle \tilde{l}_f \rangle$ vs $\langle h^2 \rangle$ for three wavelengths $\tilde{\lambda} = 0.1,\ 0.07,\ 0.7$ obtained from FE simulations. The scaling relationship of $\langle \tilde{l}_f \rangle \propto \langle h^2 \rangle^{-1/3}$, indicated by the black dotted line, agrees excellently with the simulations. This also demonstrates that $\langle \tilde{l}_f \rangle$ is independent of the wavelength as long as the wavelength is much smaller than the correlation length. Please note that unlike Figure 2.14, which has a y axis with a linear scale, the y axis in this plot is in log scale. This partially explains the apparent departure of the values of $\langle \tilde{l}_f \rangle$ from the predicted trend as log scale plots exaggerate distances at lower values. Nonetheless, some of the departure is also expected since the scaling relationship Equation 2.14 is predicated on weak scattering, a requirement that begins to be violated at higher values of $\langle h^2 \rangle$. 29

2.16 A plot of $\langle \tilde{l}_f \rangle$ vs $\sqrt{\langle h^2 \rangle}$ for three correlations lengths $\tilde{L}_c = 1,\ 0.7,\ 1.5$ obtained from FE simulations. Taking simulations of $\tilde{L}_c = 1$ as reference (red circular markers), dotted lines (blue and green) are plotted as predictions (for $\tilde{L}_c = 0.7$ & 1.5 respectively) assuming $\langle \tilde{l}_f \rangle$ scales linearly with $\tilde{L}_c$. It is seen that the FE simulations (green and blue circles) are in excellent agreement with the predicted trend. 30

2.17 Scaling of location of caustics for power law correlation function. Finite element elastodynamics simulations confirm that using a power law auto-correlation function of the form $(1 + (x^2 + y^2)/L_c^2)^{-2}$ instead of a Gaussian auto-correlation to construct $h(x, y)$ does not affect the predicted scaling of the location of the first caustic. Note that this a log-log plot. Marker indicates the mean. A two-standard-deviation width centered at the mean is indicated by a vertical line. 30

2.18 Colormap plots of $h(x, y)$ for a uniform plate (top), plate with uncorrelated randomness in thickness (middle) and plate with spatially isotropic correlated randomness in the thickness (bottom). Both random fields have the same standard deviation, $\sqrt{\langle h^2 \rangle} = 0.0301$. Zoomed in segments of the randomness are shown as insets. 33

2.19 Displacement profiles after some time t_r in the plates with uniform, uncorrelated random, and spatially correlated random thickness. The highest amplitudes seen in the plate with correlated randomness are more than double that seen in the other two cases. The wavefront (locations of highest amplitude) are zoomed into and shown on the right as 3D plots. 34

2.20 Distribution of amplitudes observed at time t_r and some reference location ($\tilde{x}_\mathrm{r}$) on the $\tilde{x}$ axis. Amplitude distribution in plate with spatially correlated randomness shows a heavy tail. 35

3.1 Spatial variation of thickness over the surface of an exemplar cylindrical waveguide. The radius of the cylindrical shell is R, axial length L_x, thickness H that varies spatially as per $H(x, s) = H_0(1 - h(x, s))$, where $\langle h \rangle = 0, \langle h^2 \rangle \ll 1$. Colormap shows the spatial variation of $h(x, s)$. Inset on the top left is an "unwrapped" view of $h(x, s)$. In the middle of the inset, a circle of radius L_c, equal to the correlation length, is shown. . . . 42

3.2 Comparison of thin shell ray equations and equations obtained from making the paraxial approximation for ray equations due to Pierce [3]. Left: Ray propagation using full thin shell theory and paraxial approximation of thin shell theory. Circular and cross markers indicate location of the first caustic. The $\tilde{s}$ axis has been "unwrapped" for representational purposes. Middle: Same ray propagation shown on the cylindrical surface. Right: Plot of the temporal evolution of quantities describing one of the rays. Here, markers indicate *temporal* location of the first caustic. It can be seen that, at higher values of $\langle h^2 \rangle$, the location of the first caustic detected from the paraxial approximation differs from thin shell. 46

3.3 Comparison of dispersion relations. Dispersion relations obtained from equation of motion of a cylindrical shell are plotted with blue dotted lines; the same dispersion relation at the $R \to \infty$ limit is shown with orange dotted lines; the dispersion relation obtained from the equation of motion of a flat plate is plotted with a yellow dotted line. It can be seen that, in the parameter regime of interest ($H_0 \ll \lambda \ll R$), the lowest branch of the dispersion relations from equation of motion a cylinder is approximated well by the dispersion relation obtained from equation of a flat plate. 49
3.4 Comparison of thin shell ray equations and equations obtained from making the paraxial approximation using Yu's formulation. Left: Ray propagation using full thin shell theory and paraxial approximation of thin shell theory. Circular and cross markers indicate location of the first caustic. The $\tilde{s}$ axis has been "unwrapped" for representational purposes. Middle: Same ray propagation shown on the cylindrical shell. Right: Plot of the temporal evolution of quantities describing the one of the rays. Here, markers indicate *temporal* location of the first caustic. It can be seen that, at higher values of $\langle h^2 \rangle$, complete back-scattering of rays is observed in the thin shell case. This not modelled by the paraxial approximation which assumes weak scattering. 54
3.5 Plot of $\alpha^{\text{Yu}}(\gamma, \epsilon)$ (Equation 3.22). This plot shows that in the parameter region of interest, α has a weak dependence on γ & ϵ. Green cross markers indicate the parameters used in studies reported here. 56
3.6 Plot of $\alpha^{\text{Pierce}}(\gamma, \epsilon)$. This plot shows that in the parameter region of interest, α has a weak dependence on γ & ϵ. Green cross markers indicate the parameters used in studies reported here. 57
3.7 Plot of the temporal evolution of the $\tilde{k}_{\tilde{s}} - \tilde{s}$ curve obtained from numerical ray simulations. Since values of $\tilde{k}_{\tilde{s}}$ are centered around zero, a constant positive offset is added for the purpose of visualisation. The first caustic is detected by finding the location where the $\tilde{k}_{\tilde{s}} - \tilde{s}$ curve folds over itself (shown in red). 59
3.8 Scaling of location of first caustic with 'severity' of randomness (top - Pierce, bottom - Yu). Individual data points are shown as red dots and the mean of each cluster is shown as a blue square with vertical lines indicating a width of two standard deviation. The expected location of the first caustic is in excellent agreement with the theoretical prediction, show with a grey line. 60
3.9 Scaling of location of the first caustic with correlation length of randomness (top - Pierce, bottom - Yu). Blue circular markers show the scaling of $\langle l_f \rangle$ for a reference correlation length. Predictions made assuming this as reference and a linear scaling with correlation length (dashed lines). The results of the numerical ray integration show (red and blue triangular markers) excellent agreement with this prediction. 61
3.10 Scaling of location of the first caustic (top - Pierce, bottom - Yu) with wavelength (top - Pierce, bottom - Yu). Note that $\langle l_f \rangle$ shows no sensitivity to almost a 100% change in the value of the wavelength. 62

3.11 Scaling of location of the expected location of the first focusing event (top - Pierce, bottom - Yu) with the radius of the cylinder. Scaling of the expected locations of the first caustic with radii from numerical ray integration. The expected location of the first caustic is independent of the radius in the parameter ranges of interest. 63

3.12 Comparison of $\langle l_f \rangle$ obtained from thin shell and paraxial ray equations from Pierce's and Yu's formulations. Thin shell equations from Yu's formulations shows significant deviation from the expected scaling at higher $\langle h^2 \rangle$, as expected. 63

3.13 Histograms of angular locations of the first focusing events obtained from numerical ray integration. Polar histograms of the angular locations, shown in blue, show no consistent appreciable angular bias. The green circle indicates the outline of a polar histogram with perfectly zero angular bias. The individual data-points used to construct the histograms are shown with orange dots. Their angular location is the one obtained from simulations; their radial position in the above plots is randomised in the interest of visualisation. 64

3.14 Emergence of branched flow of an initially plane wavefront in a thin cylinder of non-uniform thickness. Temporal evolution (a → b → c → d) of an initially plane flexural wave front in a thin elastic cylinder of non-uniform thickness. The full cylinder has been shown on the top of each panel. The regions of high amplitude at each time instant is indicated with colored lines and they been zoomed into and shown at the bottom of each panel. The emergence of branching leading to locations of extreme amplitudes and widening of the wavefront consistent with the dispersive character of this class of elastic waves is also observed. . . 64

3.15 Plot of integrated intensity (top) and scintillation index (bottom) of an exemplar FE simulation. Note that the integrated intensity has been normalised along by the mean along the circumferential direction for visually emphasise the locations of extreme amplitudes. The first prominent peak (circular marker) of the scintillation index ($SI(x)$) curve indicates the location of the first caustic (l_f). 65

3.16 Scaling of location of the expected location of the first focusing event with "severity" of randomness as obtained from finite element simulations. Circular markers indicate locations of first caustic from individual simulations. Square markers show the expected location of the first caustic. Vertical lines indicate 2 standard deviation (centered around the mean). The expected locations of the first caustic show the expected power law scaling with $\langle h^2 \rangle$. 65

3.17 Scaling of location of the expected location of the first focusing event with correlation length of the randomness from FE simulations. Taking the curve corresponding to $L_c/L_c^{\text{ref}} = 1$ to be the reference, dashed lines show the predicted behaviour at other correlation lengths assuming $\langle l_f \rangle \propto L_c^1$. The actual simulations agree well this prediction hence confirming the linear scaling. 66

3.18 Scaling of location of the expected location of the first focusing event wavelength of the initial wavefront from FE simulations. As long as $\lambda \ll L_c$, $\langle \tilde{l}_f \rangle$ is independent of wavelength. The power law scaling seems to break down at higher $\langle h^2 \rangle$. This is consistent with the expectation that the scaling holds only for weak scattering and higher $\langle h^2 \rangle$ corresponds to higher scattering. 66

4.1 Schematic of the pillared plate under consideration. Dimensions are not to scale. 70
4.2 Plot of deflection of the tip of the resonators/pillars in different mode shapes obtained from finite element simulations. Note the apparent "spatial phase" relationship. 71
4.3 For any point on the deflected plate we can find the surface normal $\hat{n}$. If there is a resonator at this site (say the i^{th} one), we postulate that position of this resonator is given by a superposition of rotation such that its longitudinal axis aligns with $\hat{n}$ and flexure away from this longitudinal axis given by $p_i\phi(z)$. Here, $\phi(z)$ is the first bending mode of a cantilever beam. 73
4.4 Comparison of modal frequency obtained from FE simulation and analytical model developed in this work. 76
4.5 MAC number comparison of mode shapes obtained from the model developed in this work compared with mode shapes obtained from FE simulations. Due to many modes being close together in terms of frequency, there is a need to match mode shapes based on their MAC number and this can be done by maximising the trace of the MAC matrix. This is done using a standard algorithm in combinatronics. This leads to the sorted pairing of the modes (R) and we can see that the model predicts mode shapes with a degree of accuracy for at least the lower modes. . . 78
4.6 Diagonal of the MAC matrix plotted before and after reordering modes using the Hungarian algorithm. It can be clearly seen, by comparing the select mode shapes plotted above, that the sorting matches similar modes even though their frequencies are highly degenerate. Mode shapes are plotted to show the deflection of the base as a contour map and the deflection of the resonators are represented by arrows indicating tip deflection direction and magnitude. 78
4.7 Polarisation causes the band gap to split. The magnitude of the split is dependent on the amount of polarisation (in this case, aspect ratio of cross-section of resonators). The slope of the grey transparent lines is given by the modal density of a uniform plate. It can be see that, outside the resonance band of the pillars, curves follow this slope. The slight departure from this trend may be explained by the discretisation approximations made when setting up the FE simulation. 79
4.8 Cumulative number of modes in system with unpolarised resonators. The result from FEM is compared with the one proposed in this text. . . 80
4.9 Effect of polarisation on modal density. Some peaks may appear merged due to frequency resolution used. (Bottom) Same plot in log scale. 81

4.10 For resonators with rectangular cross sections with unequal sides, the two principal directions become "preferred" directions for tip deflections and the Chladni patterns of the sonic crystals are similarly modified. Shown here are typical examples of Chladni patterns in such sonic crystals. The two figure correspond to the Chladni patters seen in two different pass bands 82

5.1 Schematics of tube and fin banks with tubes arranged in rectangular (left) and hexagonal (right) lattice configurations. 84
5.2 Tube in a rectangular lattice arrangement on the fins. Outer diameter of the tubes (R_o) is marked and so are the inter-tube distances (b and d_w). The inter-tube distance in the direction of transverse displacement of the tubes is b. 86
5.3 Deformation of tube (grey) + fin (blue) system at a lower vibrational mode for an illustrative case. Note that all the tubes have the same transverse deflection. This shape may be called $\psi(x)$. 86
5.4 The deformed shape of the fins (blue) can be written in terms of the deformed shape of the tubes (grey). Red dashed lines show the undeformed shape. 87
5.5 For typical lower modes of the tube-fin bank, the effect of the fins can be modelled as an equivalent soft shear core 88
5.6 Deflection of a unit cell to a shearing force. This is used to find the shear modulus of the equivalent soft shear core material. 89
5.7 ANSYS Shell Beam (top): The tubes are modelled as beam elements and the fins are modelled with shell elements. ANSYS Shell (bottom): The tube and fins are both modelled with shell elements. 90
5.8 Comparison of modal frequency estimates of tube and fin bank in fixed-fixed (left) and cantilevered (right) boundary conditions using the presented model and two different FE simulations. 91
5.9 Comparison of computation time for modal frequency of tube and fin bank in fixed-fixed (left) and cantilevered (right) boundary conditions using the presented model and two different FE simulations. Note that the y-axis in both plots has a log scaling. 92
5.10 Types of lower modes typically seen in fin and tube systems when the tubes are arranged in an irregular hexagonal lattice obtained using FEM simulations. 93
5.11 Rigid body rotation of fins in torsional modes. Properties of rigid body rotation allows description of tube deflection, tube twist and fin rotation by the single generalised coordinate θ. 95
5.12 Geometrical parameters of a tube arrangement on fins. A unit cell of the hexagonal lattice is marked using dotted lines. Here, d_y and d_z dictate the spacing between the tubes and y_1 and y_2 are some relevant length scales of the uni cell which are used in calculating energy terms and can be written in terms of d_y and d_z. 97
5.13 Comparison of bending mode frequencies estimates from presented model and finite element simulations simulations of a tube and fin bank with 4 or 24 tubes and 207 fins. We see that the presented model is within $\sim 10\%$ of the estimates from FE. 98

5.14 Comparison of twisting mode frequencies estimates from presented model and finite element simulations simulations of a tube and fin bank with 4 or 24 tubes and 207 fins. We see that the presented model is within $\sim 8\%$ of the estimates from FE. 98
5.15 A screenshot of a Python based GUI for deployment of the presented model in industry. The GUI allows for selection of pre-set fin configurations and material combinations. 99

Appendix A.1 A simple progress report is obtained by tracking the number of files in the `DataFiles` folders. 107

Appendix B.1 Schematic of monatomic 1D crystal 110
Appendix B.2 Dispersion relation for a monatomic chain 111
Appendix B.3 Schematic of diatomic 1D crystal 112
Appendix B.4 Dispersion relation for a diatomic chain where the ratio of the masses, $\mu = 1.5$. The orange shaded region is called a band gap and no propagating waves exist in this frequency band. 112
Appendix B.5 Dispersion curve for a monatomic lattice formulated as a diatomic lattice. 113
Appendix B.6 Centered square lattice. 114
Appendix B.7 The iso-frequency contours of the two branches of the solution of the characteristic equations. Notice that both branches have an 8 fold symmetry. 115
Appendix B.8 (Left) The dispersion surface in 3D. (Right, top) Top view of the dispersion surface. (Right, bottom) Dispersion curve in the Irreducible Brillouin Zone 116

List of Tables

2.1 Summary of some wave scattering phenomena. 12
2.2 List of parameters used in numerical ray integration and FE simulations for all the results presented here. Unless stated otherwise, it may be assumed that the parameter values in bold face were used. 20

3.1 List of parameters used in numerical ray integration and FE simulations for all the results presented here. When it is unclear from context, it may be assumed that the parameter values in bold face were used. 67

4.1 List of parameters used in FE simulations. 76

5.1 Summary of the performance of FE, discrete model and smeared model at modal frequency estimation. 91

Declaration of Authorship

I declare that this thesis and the work presented in it is my own and has been generated by me as the result of my own original research.

I confirm that:

1. This work was done wholly or mainly while in candidature for a research degree at this University;
2. Where any part of this thesis has previously been submitted for a degree or any other qualification at this University or any other institution, this has been clearly stated;
3. Where I have consulted the published work of others, this is always clearly attributed;
4. Where I have quoted from the work of others, the source is always given. With the exception of such quotations, this thesis is entirely my own work;
5. I have acknowledged all main sources of help;
6. Where the thesis is based on work done by myself jointly with others, I have made clear exactly what was done by others and what I have contributed myself;
7. Parts of this work have been published as:

   K Jose, N Ferguson, and A Bhaskar. Branched flows of flexural waves in non-uniform elastic plates. *Communications Physics*, 5(1), 2022. URL `https://www.nature.com/articles/s42005-022-00917-z`

   K Jose, N Ferguson, and A Bhaskar. Branched flows of flexural elastic waves in non-uniform cylindrical shells. *PLoS ONE*, 18(5), 2023. URL `https://doi.org/10.1371/journal.pone.0286420`

Signed:.. Date:..................

Acknowledgements

Thank you, Atul, for your guidance, support, kindness and generous spirit. Thank you for letting me have an experience of doctoral research with a lot of freedom and independence. I am glad you trained me in not just the relevant research topics and academic writing but also gave me, during numerous relaxed chats, an introduction to the history and even, perhaps, the sociology of applied mechanics. This is just the kind of doctoral research experience I was looking for. Thank you for being generous with your time.

Thank you, Neil, for your constant support and guidance. Also, I am grateful to you for taking on the rather mundane, but nonetheless critical, administrative components of doctoral supervision after Atul left for Sheffield. Many thanks to Maryam for her support and guidance in the early stages of this dissertation.

Thank you, Claus, for hosting us, ESRs, at Vestas aircoil. Thank you for helping us during our time in Denmark. Thanks also to Frank and other Va employees in Lem. I am grateful to the European Union for their generous financial support in the form of a Marie Curie Fellowship, as part of the InDEStruct H2020 project (Grant Agreement No. 765636). Thanks to Atul (Singh), Milena and Talha for being wonderful colleagues in the InDEStruct project. The use of the IRIDIS High Performance Computing Facility, and associated support services at the University of Southampton, in the completion of this work is also gratefully acknowledged.

A part of the work reported in this dissertation was done in Rinkøbing, Denmark. Many thanks for all the folks at Career Campus, Rinkøbing who made the stay so pleasant. I will forever cherish memories of the sunsets by the fjord and the house parties at Career Campus.

Thank you, Nana, for your love and companionship. Many thanks for being there when I was not very sure of myself. I will miss you and our travels together. Thank you for showing me the beauty of and from Jutland.

Thanks to the Boldrewood Campus desk-neighbours for their friendship and support. I will miss our lunch breaks, Brewdog pub nights and bouldering sessions. Thanks also to the IIT Kanpur and Meta folks for putting up with me and putting me up in London. The, all too frequent, weekend trips to London were a wonderful way to recharge. Thanks to the online LDG group for all the thought-provoking conversations over the years.

Finally, many thanks to my parents and brother. Your love and support through this entire journey was vital. I could not have done this without all of you. I am forever grateful.

To Mummy

Chapter 1

Introduction and literature survey

The dynamics of elastic media continues to be of great interest in a wide range of technological and natural contexts. Engineers frequently encounter design problems where structural dynamics plays a key role because the operating environment has temporally fluctuating forces, giving rise to a dynamic response of the structure. In particular, there are many structural parts that appear in the form of thin-walled structures such as an elastic plate or a shell. These are of particular interest because of the their ubiquitous presence due to nature of manufacturing - e.g. a plate formed by rolling metals, or a cylindrical hell produced by processes such as turning or plastic extrusion through a die, in addition to the structural function served by such constructions – e.g. the fuselage of an aircraft, a pressure vessel, or a container.

The study of the dynamics of such thin-walled structures can be carried out by modelling them using partial differential equations and solving these equations analytically, whenever possible. Recent rapid advancements in computing power provide us with yet another tool in the form of numerical simulations. The domains of the structures of interest are discretised, i.e. broken up into smaller inter-connected pieces, and the resultant problem is solved numerically using techniques such as finite element method or finite difference method. Even more recently, high-performance clusters (HPC), also called “supercomputers”, with numerous interconnected computing cores, have provided a way to speed up the aforementioned numerical simulations.

In addition to the practical consideration as to why thin-walled structures are important due to their ubiquity in nature and the industry, structural mechanics has made great advances in the simplified mathematical descriptions of such elastic solids, which attempts to make assumptions about the elastic displacement field through the thickness. While all real structures are three-dimensional, these kinematic assumptions lead to a dimensional reduction in the corresponding mathematical problem concerning plates and shells, vis-a-vis full 3D elasticity that is often analytically intractable, and computationally expensive.

Shells and plate form essential components in aerospace engineering [6], offshore structures [7], floating platforms [8], launch pads, launch vehicles, pressure vessels [9], and containers. Because of the inevitable manufacturing tolerances, these components show variability in their geometry and properties from the intended design. The propagation of elastic waves in such non-uniform wave-bearing media is motivated by a host of practical examples such as these.

Three types of non-uniformities have been typically considered in the existing literature on wave propagation in non-uniform elastic media. The first is wave propagation in elastic solids with (spatially) periodically varying properties. The non-uniformity can appear in the form of periodically varying material properties , geometric properties, or regularly spaced inclusions, attachments, and/or constraints. The motivation for studying such problems is twofold. The first one is to understand the dynamics of some engineering structures such as bladed disks [10], rail lines (with regularly spaced sleepers) [11], and heat exchangers (with regularly spaced metal fins). The second motivation is to *engineer*, the so-called, phononic/acoustic meta-materials [12, 13] which make use of "spatial periodicity" to confer the structure some special dynamical properties with respect to frequency response and enables some exotic behaviours such as acoustic cloaking [14] and negative refraction [15]. At lower frequencies, homogenisation techniques can be applied to simplify the analysis in order to infer the wave dynamics. At moderate or high frequencies, Bloch-Floquet-based analysis [16] is used to infer wave dynamical response. These techniques utilise the translational symmetry of the problem to simplify the analysis/numerical simulations. A short primer on this has been included in the appendix of this work. Also see [17] for discussions of high-frequency homogenisation techniques.

The second type of non-uniformity that has been considered in literature is systematic spatial variation in properties, usually described by well-defined (non-random) functions [18–25]. These variations can be due to varying geometrical or material properties. Advances in additive manufacturing have enabled their ease of fabrication [26]. Such structures are collectively referred to as functionally graded materials [27, 28]. They have found applications in areas such as compliant mechanisms [29], biomechanics [30], and sensing [31].

Lastly, the third kind of non-uniformity that has been considered is random inclusions or randomly varying properties . Theoretical [32], experimental [33], and numerical studies [34] has been done to understand the effect of a single inclusion (scatterer) on wave propagation. This has also been subsequently extended to include multiple discrete randomly-placed scatterers [35–37]. However, there are very few studies where the non-uniformity takes the form of smooth *spatially-correlated* randomly-varying properties [38, 39]. The question of wave propagation in such cases seems to be especially under-examined.

To address this, the first portion of the present work is motivated by the propagation of bending waves in thin-walled structures when there are structural imperfections leading to a correlated spatial variability (e.g. in thickness, which is a key parameter to characterise bending wave propagation). A sound scientific understanding of this problem is desirable since, even structures that are manufactured to be nominally materially homogeneous and geometrically uniform, inevitably possess some non-uniformity. Further, bending waves introduce unique mathematical challenges because of the wave speed being strongly dependent on the wave length, unlike mostly non-dispersive waves in many other contexts such as electromagnetism, optics, etc., where this dependence is weak.

Also, bending waves are the dominant mode of propagation for most practical situations in the dynamics of 1D and thin-walled structures such as plates and shells, because axial and in-plane stiffness is large relative to flexure, so the axial and in-plane propagation is energetically unfavourable for low frequency dynamics. In addition to engineered structures, many naturally occurring elastic solids pose similar mechanical and mathematical challenges, for example, those in geophysics such as seismic waves in geological plates or waves borne by floating ice sheets.

In this work, the propagation of an initially planar wavefront in an elastic plate with random variations in properties is studied. Surprisingly rich and complex branching patterns are seen in the dynamical response. This is shown to be caused by the correlated nature of the randomness. The deep connection of this observation to an entire class of scattering phenomenon called *branched flows* [40, 41] is explored. While, branched flows have been observed previously in other physical systems, it has not been reported previously in elastic structures.

Spatially correlated randomness[1] leads to “random focusing” of the wavefront. This subsequently develops into distinct “branches” of wave propagation. The focusing also leads to the appearance of high amplitude locations[2]. Despite the stochastic nature of this phenomenon, surprisingly, the expected location of these high amplitude events shows an elegant scaling with the statistical properties of the randomness field. The expected location shows a linear and a power law scaling with correlation length and some appropriate measure of the “severity” of randomness, respectively. Here, correlation length is a measure of how how ′rapid′ the random spatial variations are. The ″peaks″ and ″valleys″ in the random field have spans that are roughly equal to the correlation length. In a more precise sense, the correlation length appears as a length scale in the autocorrelation function of the randomness field.

---

[1] Spatially correlated random variation in thickness is studied here. However, the analysis presented clearly shows that it can be generalised easily to other variations in geometric or material parameter.

[2] These amplitudes can be more than 10 times the amplitude of the original wavefront despite the “severity” of the randomness being fairly small.

Kulkarny and White [42] studied the general problem of wave propagation through weakly inhomogenous media where they also derived the scaling law associated with branched flows. One of the earliest observations of, what are now called, branched flows were then made in the context of radio waves [43, 44]. Partially ionised clouds provide the weakly scattering medium in that case. Topinka et al. [2] experimentally demonstrated the existence of branched flows in two-dimensional electron gas.

Branched flows have also been proposed as an explanation for an interesting observation in acoustic waves carried by oceans. It is well known that at the depth of around $\sim 0.75 - 1.4$ km below the surface of the ocean there is the so called sound fixing and ranging channel or deep sound channel. A local minima (in the depth direction) of sound speed at this depth makes this an effective waveguide that can carry sound over large distances (thousands of kilometers) [45]. It was also well known that this medium is weakly inhomogeneous and therefore weakly scattering to acoustic waves [46]. However, acoustic pulses were seen to be much better preserved than expected after propagating over long distances and presumably, undergoing multiple scattering [47]. Wolfson and Tomsovic showed [48], from numerical studies, that the stable branches of energy flow emerging due to random focusing by a spatially correlated randomness partially explains this phenomenon. However, they do not use the phrase "branched flows".

Degueldre et al. studied the propagation of tsunami waves modelled using the classical wave equation [49]. The non-uniform and spatially correlated bathymetry of the ocean is shown to present the kind of disorder that supports branched flows. Numerical simulations are carried out using actual bathymetry data of a certain portion of the Indian Ocean. Existence of branched flows and the associated scaling laws are demonstrated. It is also shown there that the location of high amplitude waves change significantly with even minor changes in the bathymetry. This shows that branched flows may need to be accounted for when attempting to predict wave amplitudes and their locations in a tsunami.

A very ingenious demonstration of branched flow of light was recently reported by Patsyk et al. [50]. Thin soap films are used as a waveguide for light. An optical fibre is used to launch a laser beam into the soap film. The naturally occouring spatially-correlated thickness variation in the soap films provides the disorder. Some expected statistical properties of distribution of intensities and the associated scaling law are verified experimentally.

Another study of branched flows of electromagnetic waves (microwaves) was carried out by Höhmann et al. [51]. Propagation of microwaves over a domain with spatially-correlated randomly varying electric potential is considered in this study. A metallic plate is decorated with randomly placed "cones" to achieve the disorder. Branch-like patterns and "hot-spots" in amplitude, characteristics of branched flows, are observed experimentally. These were also compared with numerical simulations.

A series of studies have investigated the statistical properties of branched flow [52–54]. Branched flows have been studied for non-linear waves [55] and anisotropic media too [56]. Given the recency of many the fundamental studies on branched flow, it is not surprising that very few applications of branched flow have been identified so far [57]. Very recent advances in this area [58, 59] suggests that branched flows could be leveraged in designing efficient waveguides.

All these physical phenomena in which branched flows have been identified, except electron waves, are governed by the (non-dispersive) *classical* wave equation. By contrast, flexural waves in elastic plates are governed by the strongly dispersive *bi-harmonic* wave equation. Hence, the observation of branched flows in elastic structures is surprising given the remarkably different physics that governs flexural waves in elastic plates. This suggests some universality of branched flows in wave dynamics. This is explored to a certain extent in this work, where the study of branched flows is extended to cylindrical shells of modest curvature.

While some work has been done on wave propagation in plates with randomly varying properties, similar studies for elastic shells are missing. The existing studies seem to consider randomness in a very limited sense, say, confined to axial variations [60, 61]). This, however, is not particularly surprising. Even the formulation of equations of motion for a shell of uniform thickness are more recent [62–64] compared to those for plates [65–67]. The dynamics of even perfectly homogeneous shells are a matter of active research [68, 69]. This may explain why the study of wave propagation in non-uniform shells is in its relative infancy. In the current work, flexural wave propagation of elastic waves on thin cylindrical shells with randomly varying thickness is considered. This follows the style of analysis carried out for elastic plates in this work to demonstrate the existence of branched flows in cylindrical elastic shells.

It is perhaps instructive, at this point, to take a detour and describe where branched flows fit in the class of other well-known random wave scattering phenomena. The key length scales involved are the wavelength of the wavefront and the 'feature size' of randomness. Rayleigh scattering [70–72] describes the case when the scatterers ('feature size' being the size of discrete particles/spatial correlation length of randomness here) are much smaller than the wavelength. The severity of scattering, in this regime, scales as the inverse of the fourth power of the wavelength and explains why the sky is blue [73–75]. In the regime of scattering by randomness or particle of 'feature size' of the order of the wavelength under consideration, wave scattering is governed by Mie scattering [3]. Scattering severity is independent of wavelength and explains the grey/white colour of clouds [72, 76]. Lastly, wave transmission in a continuum with small spatially correlated randomness shows branched flows when the ‘feature size’ (here, correlation length) is much larger than the wavelength. Here too, the severity of scattering is independent of wavelength. The existence of random focusing [42, 77], leading to regions of large amplitude and emergence of distinct branching, typifies branched flows. Also, the existence of a scaling relationship [52, 53] between expected locations of high amplitude and statistical properties of the randomness field is another feature unique to branched flows. The distinction between branched flows and other wave-scattering phenomena is elaborated upon in this work.

Returning to the spatial variability of response in structures: Interest in the spatial patterns seen in the response of vibrating plates, which goes as far back as Leonardo da Vinci and Galileo Galilei [78], actually motivated the very search for a mathematical description of the motion of elastic plates. The first systematic scientific interest in this subject started developing after Earnst Chladni’s demonstration of what has come to be known as ”Chladni’s patterns” [79]. The demonstration lead to the establishment of a prize, by Napoleon Bonaparte, to be awarded for a mathematical description of plate vibration [78]. The prize was awarded to Sophie Germain, a largely self-taught mathematician, for finding the correct differential equation describing the motion of flat plates [65]. However, the boundary conditions were incorrect and Gustav Robert Kirchhoff is credited with the first solution to the vibration of circular plates [66]. Today, Kirchhoff-Love and Mindlin plate theories are the most popular standard theories for describing the motion of elastic plates [67].

Besides non-uniformity influencing the dynamics of elastic wave propagation, plates with periodically placed elastic rods provide an opportunity to tailor the rich dynamical behaviour. Plates decorated with pillars and rods [80–87] have also attracted recent interest as acoustic meta-materials and phononic crystals [88, 89]. However, most of these tend to be focused on modeling wave transmission characteristics by considering theoretically infinite lattices. The spatial periodicity present in most meta-materials can then be used to aid analysis. Also, the wave propagation question in the general class of *master* structures decorated with nominally numerous identical micro-structural elements has been studied in its generality by Mishuris et al. in a recent paper [90]. A study of the modal vibration of pillared plates seems to be missing from the literature.

Based on observations made from some numerical experiments and supported by physical (energetic) arguments, an *anzats* about the mode shapes is made. This is used to construct a Rayleigh quotient-based approximation of the modal vibrations and compared against finite element simulations. Cross-disciplinary tools [91] are leveraged to match mode shapes of the pillared plates before comparing them.

---

[3] Mie scattering may also refer to the solution of wave scattering by a *single* particle.

Next, a wholly industrial application of the study of spatial variability of dynamic structural response is considered. The modal vibration of tube-and-fin banks, which are critical components in many heat exchangers, is studied. Here too, certain observations about the mode shapes motivate the proposal of a Rayleigh-quotient-based approximation of the modal vibrations. Lower vibrational modes are shown to be well approximated by mode shapes of equivalent (fictitious) beams in flexure and rods in torsion. The proposed model is shown to be in good agreement with FEM simulations while being computationally very efficient by comparison.

Heat exchangers provide an interesting practical context to study vibrations since they are composed on many sub-components often arranged in repeating patterns; all this contributes towards a complex dynamical response. The dynamics of heat exchangers are of great interest since vibration is a well-known cause of failure [92] in these structures. Heat exchangers are often mounted on the engines directly which are sources of base excitation. There is existing literature that considers the dynamics of heat exchanges, however, most of them seen focused on flow-induced aero-elastic vibrations [93–95] and not with the purely structural response to base excitation from engines. Also, while there are many numerical studies on the dynamics of heat exchangers [96], there seems to have been little focus on developing computationally efficient models of HE vibrations that can be deployed in early design stages. The need to conduct parametric sweeps over numerous design parameters and the associated ‘curse of dimensionality’ [97] precludes the possibility of naive numerical modal analysis of each design under consideration in the early stages. This, therefore, motivates the computationally efficient modelling of tube-and-fin vibrations presented here.

Thesis overview

This dissertation is divided into six chapters (the first being this one) and two appendices. In Chapter 2, the question of propagation of flexural waves on thin elastic plates with random spatially-correlated properties is considered. Connection to branched flows is established from theoretical analysis of partial, ordinary, and stochastic differential equations associated with the wave propagation problem. The ray dynamics representation of the problem [98] is studied numerically using a finite difference scheme. The complete wave elastodynamics problem is studied using finite element method-based transient simulations.

Chapter 3 concerns the transmission of flexural waves on thin elastic cylindrical shells with random spatially-correlated properties and the possible existence of branched flows. Theoretical and numerical analyses undertaken are akin to the ones described in Chapter 2. Owing to the multiplicity of the mathematical descriptions of the dynamics of elastic cylinders, two different ray formulations of the problem are analysed theoretically and numerically. One set of these ray equations is also derived directly from the equations of motion. FEM-based transient simulations are also carried out.

In Chapter 4, the modal vibration of a finite plate decorated with numerous identical pillars, inspired by industrial assemblies such as heat exchanger tubes coupled by end plates, is studied. The emergence of a spatial phase relationship between the tip deflections of the pillars in the mode shapes is noted. An *anzatz* about the mode shapes based on this allows for the construction of a Rayleigh quotient-based model of the modal characteristics. This is then compared with FEM-based modal analysis. Some ideas for matching mode shapes obtained from the presented model and from FEM simulations are also discussed.

Chapter 5 concerns the study of modal vibration of tube-and-fin bank assemblies for long waves, i.e. low modes. These form critical components of heat exchanger assemblies and their lower vibrational modes are of interest. Based on numerical experiments and physical arguments, some *anzats* about the lower vibrational mode shapes is arrived at. This is developed to construct a Rayleigh quotient-based approximation which is shown to be computationally efficient as compared to FEM simulations of the same structure. Good agreement with FEM simulations is established for different configurations of the tube arrangement on fins. Finally, the development of a graphical user interface, which packages the presented model for deployment in industrial settings, is discussed.

The main developments presented in this work are summarised along with remarks about possible future directions in Chapter 6. Further details about the FEM simulations which were carried out as part of chapter 2 and 3 are given in Appendix A. Appendix B contains an introductory tutorial on the application of Bloch's theorem to study the dynamic response of simple spring-mass lattices. The study of periodic structures through this route is another case where the spatial variability of the dynamic response is of tremendous interest.

Chapter 2

Flexural waves in random elastic plates: branched flows

2.1 Introduction and motivation

All practical structures are necessarily three-dimensional; however, mechanical abstractions such as rods, shafts, beams, plates and shells utilise fewer spatial dimensions and they occupy a special place in engineering as well as in the mechanics of many naturally occurring elastic structures. Accordingly, simplification in their mechanical models is commonly sought. Rods, shafts, and beams have one of the three characteristic dimensions much longer than the other two, and they primarily transmit stretch, torsion and bending deformations respectively. One-dimensional models to describe their mechanics are adequate for many practical situations, a simplification that enables us to have an analytical grip in understanding the mechanics of a host of problems in mechanical, aerospace, automotive and marine engineering. By contrast, flat plates and and shells have one of the three characteristic dimensions much smaller than the remaining two, thus the relevant governing equations necessarily involve two independent spatial coordinates. Examples of elastic plates and shells include aircraft fuselage, wing structures in aerospace applications, geological plates, floating ice sheets, pipes, pressure vessels, floors, decks and ship hulls.

Plates and shells tend to be softer in *flexure* than in stretch, so that lower modes of vibration are likely to be associated with bending than in in-plane stretch. Therefore, we will focus our attention on flexural waves in this dissertation and ignore the in-plane dynamics. In all these thin-walled structures, spatial variations in flexural stiffness inevitably exists because of manufacturing tolerances and variations in the

---

[0] Substantial portions of this chapter have been published in "Jose, K., Ferguson, N. & Bhaskar, A. Branched flows of flexural waves in non-uniform elastic plates. Commun Phys **5**, 152 (2022)".

material properties. When waves propagate through one-dimensional elastic waveguides such as beams, rods, or shafts, that possess spatial variability, scattering can localise spatial response due to the disorder, or the propagation can exhibit Floquet-type response that has been well-studied in the past. Because of the one-dimensional geometry, the scope of studying spatial patterns during wave motion does not arise here, unlike two and three-dimensional geometries where such an opportunity exists. In the first part of this dissertation, we will be concerned with the emergence of spatial patterns in random elastic plates and shells. The present chapter is dedicated to the flexural dynamics of random flat plates, whereas the dynamics of cylindrical shells will be taken up in the subsequent chapter.

2.1.1 Dynamics of elastic plates

Starting from a free body diagram of an infinitesimal piece of an elastic plate, the equations of motion are not only difficult to derive, there are known objections concerning the kinetic boundary conditions as they are often obtained in an *ad hoc* manner from approaches that are not variational. While following a variationally consistent approach, one starts with kinematic assumption that any normal to the mid-surface of the plate remains undeformed and normal. This eliminates all three strains associated with the thickness direction, i.e. one direct strain and two shears.

Bending of a flat plate is characterised by the two curvatures of the deformed surface. Accompanied by the bending, the plate also undergoes twist, characterised by the cross-derivative of the surface deflection. In addition, the Poisson's ratio couples the two-dimensional stress-strain relationship. Accounting for these, the strain energy of an elastic plate in transverse motion is given by

$$U(t) = \frac{D}{2} \iint_A \left[(\partial_{xx}\eta)^2 + (\partial_{yy}\eta)^2 + 2\nu \, \partial_{xx}\eta \, \partial_{yy}\eta + 2(1-\nu)(\partial_{xy}\eta)^2 \right] \mathrm{d}A, \tag{2.1}$$

where $\eta(x, y, t)$ is the transverse deflection of the mid-surface at time t, originally in the x-y plane, D is the bending stiffness assumed above to be *constant* throughout the plate, ν is the Poisson's ratio of the plate material. Here the first two terms correspond to the strain-energy density (i.e. per unit area) due to the two curvatures, the third term arises from the Poisson's coupling in the 2-D constitutive relations, and the last terms is due to the twist of the surface. The kinetic energy density of an elastic plate in motion is given by $(1/2)\rho H(\partial_t \eta)^2$, so the total kinetic energy $T(t)$ of the plate is the area integral

$$T(t) = \frac{1}{2} \iint_A \rho H (\partial_t \eta)^2 \, \mathrm{d}A, \tag{2.2}$$

where H is the thickness of the plate assumed above to be uniform. So the Lagrangian for the continuum is given by $L = T - U$. Applying Hamilton's principle [99], we set the first variation of the integral of the Lagrangian to zero, i.e. $\delta \int_{t_1}^{t_2} L \, \mathrm{d}t = 0$, where δ

is the variation of the functional following the operator sign, t_1 and t_2 are arbitrary instants of time, so we obtain the following governing equation of transverse motion

$$\rho H \partial_{tt} \eta(x, y, t) + D\nabla^4 \eta(x, y, t) = 0, \tag{2.3}$$

where ∇^4 is the biharmonic operator given by $\nabla^4 = \left(\partial_{xxxx} + 2\,\partial_{xxyy} + \partial_{yyyy}\right)$. The above field equation is often known as the Kirchhoff–Love plate equation [67, 99, 100]. Application of Hamilton's principle also leads to variationally consistent boundary conditions – not stated here, as we are not considering reflections. When the thickness or the bending stiffness are spatially varying, i.e. $H = H(x, y)$ and $D = D(x, y)$, the inertia term remains unchanged except that the spatial dependence of H replaces the first term, whereas the second term is more involved and just replacing the bending stiffness by $D(x, y)$ would be incorrect. We will take this up in the next section.

The assumption of normals remaining normal amounts to ignoring through-thickness shear strains, when the characteristic dimensions in the $x - y$ direction are much larger than the thickness for statics, and the wavelength of interest is much larger than the thickness for dynamics. When thickness starts becoming comparable to the wavelength, shear needs to be included in the strain energy, the corresponding correction is usually attributed to Mindlin [101, 102]. In this chapter, we will ignore shear correction and assume the thickness to be significantly smaller than the wavelength of interest.

2.1.2 Elastic plates with non-uniform flexural stiffness

The basic procedure that one follows to derive the equation of motion of a plate with variable thickness remains the same as the one that is followed for a uniform plate. However, as stated above, a simple substitution of a constant bending stiffness D by a spatially dependent one $D(x, y)$ will yield incorrect results. This is because the form of the strain energy given in Equation 2.1 is obtained for the infinitesimal plate element *assuming* constant thickness along the entire domain of the plate. Due to the non-commutativity of multiplication and partial derivative operations, the imposition of force equilibrium needs to be carried out anew considering $D(x, y)$ to be spatially varying. This will not duplicated here, since it is the subject of many standard texts. The interested reader may consider studying the appendix of Leissa's report on the vibration of plates [103] for the derivation. In this work, the formulation from [104] will be used. The equation of motion of a plate with varying thickness can be written in terms of bending moment per unit edge length ($M_x,\ M_y$) and twisting moment per unit edge length (M_{xy}) terms (also known as stress resultants that eliminate thickness dependence) as

$$\rho H \partial_{tt} \eta + \partial_{xx} M_x + \partial_{yy} M_y + 2\partial_{xy} M_{xy} = 0, \tag{2.4}$$

where, $M_x = D(\partial_{xx}\eta + \nu\partial_{yy}\eta), M_y = D(\nu\partial_{xx}\eta + \partial_{yy}\eta), M_{xy} = (1-\nu)D\partial_{xy}\eta$, ρ is the density of the material, $H(x,y)$ is the thickness of the plate, ν is the Poisson ratio, $D(x,y) = \frac{EH(x,y)^3}{12(1-\nu^2)}$ is the bending rigidity of the plate, a function of position (x,y) here, and E is the Young's modulus.

2.2 Branched flows in inhomogeneous media

In this chapter we shall study flexural waves traveling in thin elastic plates in the presence of small random modulations in the thickness. This wave propagation problem shares a connection with a phenomenon called branched flow. It has previously been observed in many domains of physics and mechanics (except elasticity). Branched flows are discussed briefly in this section.

Waves travelling in weakly inhomogenous media with spatially isotropic correlated randomness, of correlation length L_c much larger than the wavelength λ of the wave front, get weakly scattered and show a branching behaviour which leads to "focusing" i.e. regions of high wave amplitudes. While the location of such "focusing events" (also called caustics) is a stochastic quantity, the expected distance of the first of such focusing events from the point of launch of the wave front, $\langle l_f \rangle$, has a surprisingly elegant scaling relationship with $\langle h^2 \rangle$, a suitably non-dimensionalised measure of the variance of the randomness[1], and with the correlation length. This scaling relationship is given by $\langle l_f \rangle \propto L_c \langle h^2 \rangle^{-1/3}$, where the angular brackets denote mean of the respective quantities. The scaling is also surprisingly independent of the wavelength of the wavefront. This phenomenon is called branched flow [40].

Branched flows have been reported in electron waves [2], microwaves [51], tsunami waves [49, 105] (see Figure 2.1), visible light [50] and sound waves in the ocean [48]. The statistics of the phenomenon have been the subject of numerous theoretical investigations [52–54]. It has been demonstrated in non-linear waves also [55].

Phenomenon	**Scatterer Distribution**	**Complete Localisation**
Bragg & Brillouin scattering [16]	*Perfectly Uniform*	*Possible (Freq. Dependent)*
Anderseron localisation [106]	*Nearly Uniform*	*Possible (Freq. Dependent)*
Local resonance [107]	*Irrelevant*	*Possible (Freq. Dependent)*
Rayleigh & Mie scattering [72]	*Random (Uncorrelated)*	*No*
Branched flow [40]	*Random (Correlated)*	*No*

TABLE 2.1: Summary of some wave scattering phenomena.

It is instructive to consider some other kinds of scattering and localisation phenomena which lead to high amplitudes so as to place branched flows in this class of phenomena (non-exhaustive list):

---

[1] $\langle h^2 \rangle$, for the case under consideration, is defined rigorously below

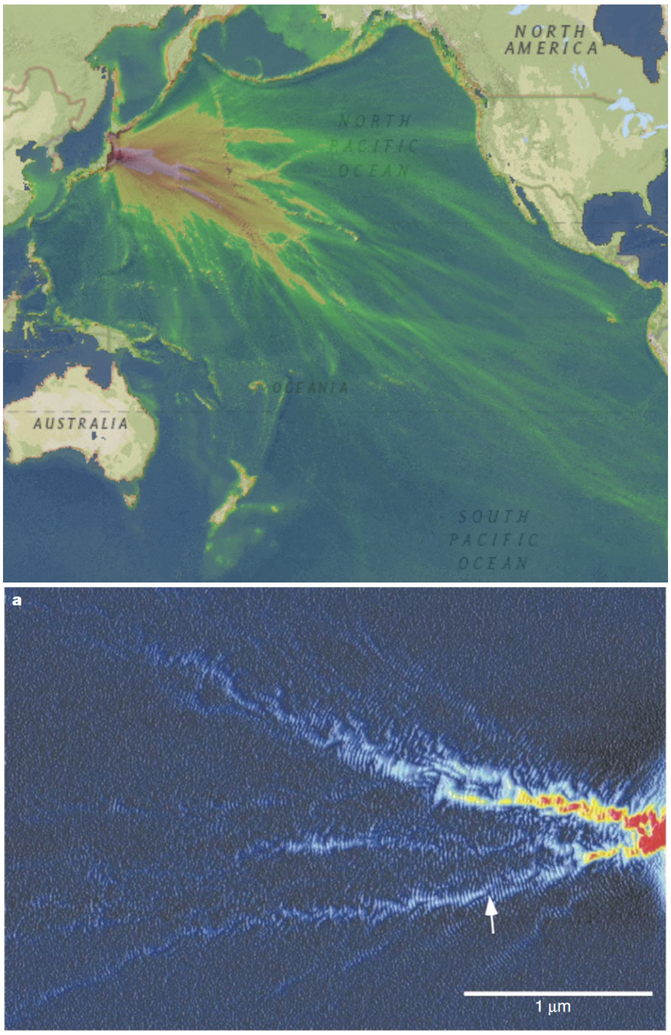

FIGURE 2.1: Branched flows have been observed in many different physical contexts and length scales (L) Branched flow visible in Tohoku earthquake tsunami, 2011 [1]. (R) Branched flow in electron gas [2].

- Bragg and Brillouin scattering [16] describe wave dynamics in the presence of uniformly distributed or periodic scatterers. It is typified by the existence of band gaps. Excitations with frequencies that lie within these bands do not propagate and are localised. Band gaps are observed when the wavelengths are of the order of the distance between the scatterers.

- Anderson localisation [106] is observed in the presence of *nearly*-uniformly distributed scatterers. The introduction of even small inhomogeneity in an otherwise uniformly distributed set of scatterers causes waves, which would propagate according to Brillouin scattering theory, to localise and not propagate. This was described by Anderson as an *"absence of diffusion..."*.

- Local resonance [107] of scatterers with internal degrees of freedom introduced onto an otherwise uniform medium can be leveraged to augment the wave transmission behaviour. Excitations of frequencies close to the resonance frequency of the scatterers are localised. These are often used to form "acoustic cloaks" [108]. Specific spatial distributions of the said scatterers may motivate localisation. However, a uniform arrangement is typically not required [109].

- Rayleigh scattering [72] describes the scattering of waves interacting with randomly distributed scatterers whose sizes are much smaller than the wavelength of the wavefront under consideration. The intensity of scattered radiation has a power law scaling with exponent -4 with wavelength. At a certain distance from the source, the probability of finding high-intensity peaks displays exponential decay. After sufficient propagation and therefore repeated scattering, the energy density can be described by the diffusion equation [110].
- Mie scattering is similar to Rayleigh scattering, except that the scatterers' sizes are of the order of the wavelength. The intensity of scattered radiation is independent of wavelength, unlike Rayleigh scattering.
- Branched flow [40] refers to the scattering and random focusing of waves due to the presence of spatially correlated randomness. The spatial correlation length of the randomness is much larger than the wavelength of the wavefront. The expected location of the first focusing event scales linearly with the correlation length and has a power law scaling with the variance of a suitable non-dimensionalised measure of randomness. At a certain distance from the source, the probability of finding high-intensity peaks is much higher than what one would see from Rayleigh scattering (see [50] for comparison). This 'heavy-tailed' probability is due to the presence of stable high-intensity branches.

It must be noted that very recent works [58, 59] have suggested that there may be deeper connections between Bragg and Brillouin scattering and branched flows than previously thought.

While branched flow of waves has been reported in seemingly unrelated fields, the underlying governing equation in most cases is the classical *non-dispersive* wave equation

$$\partial_{tt} f(x, y, t) = c^2 \nabla^2 f(x, y, t), \tag{2.5}$$

where $f(x, y, t)$ is the field variable that depends on the position x, y and time t; c is the wave speed, which is independent of the wavelength.

By contrast, bending waves in elastic plates are dispersive, as shorter wavelength waves travel faster. Such structures are frequently encountered in the physics of geological plates, glaciology of ice sheets, thin films, nano-mechanics of 2D materials such as graphene, aerospace skin structures, etc. Waves in thin elastic plates are governed by the bi-harmonic Kirchhoff–Love equation [99]

$$\partial_{tt}\eta(x,y,t) = -\beta^2\nabla^4\eta(x,y,t). \tag{2.6}$$

Here, η is the transverse displacement, $\beta^2 = EH^2/12\rho(1-\nu^2)$ combines the thickness of the plate H, Young's modulus E, Poisson's ratio ν and the material density ρ. The group velocity c_g is proportional to the wave number k, i.e. $c_g \sim \beta k$, as evident from the fourth spatial derivative. The biharmonic wave equation describes wave in plates of thickness much smaller than the wavelength of interest λ, i.e. $H \ll \lambda$, since higher order effects such as shear through the thickness [111] can be ignored. We restrict our case to such plates. Likewise, rotary inertia [101, 112, 113] and kinematic non-linearity due to large rotations associated with the so called von Karman strains [114] are be neglected.

The character of the waves governed by the biharmonic wave equation is markedly different from those governed by the classical wave equation in many respects. For example, a "sharp" wave packet would continue to propagate without distortion if the wave phenomenon is governed by the classical wave equation. If, instead, it is governed by the biharmonic wave equation, a similar "wave packet" would continuously deform with propagation. The initially "sharp" wave packet would "spread-out" and widen as it propagates. This is due to the presence of the fourth derivative (in space) in the case of the biharmonic wave equation, as opposed to the second derivative in the case of the classical wave equation. This confers a dispersive character to the former that the latter lacks.

Transmission of flexural waves in such plates, when their thickness has modest spatially correlated randomness, is studied here with a focus on branching behaviour. The scaling law that governs the expected location of high amplitudes is also explored, using using analytical approaches and two different numerical methods. Branched flows or similar phenomenon have not been reported in elastic structures and hence, a positive outcome of this proposed exploration would result in the uncovering of a, hitherto unknown, scattering phenomenon in elasticity. Additionally, given the differences between classical waves and the waves that are governed by the biharmonic wave equation, this would also point towards a certain universality of branched flows in random media, which is agnostic of the specific physics.

2.3 Scaling from analysis of ray equations

In order to derive the scaling relationship associated with branched flow, consider a plate of uniform density, Poisson's ratio and Young's modulus but mildly inhomogenous thickness. The thickness field can be expressed as

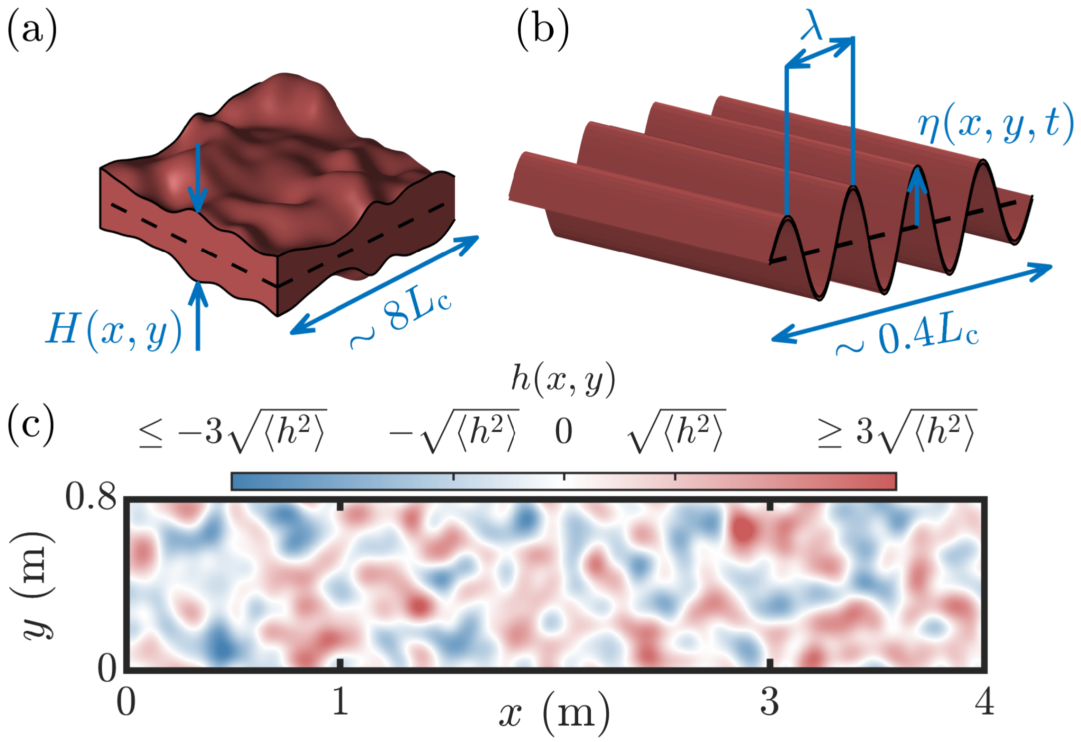
(a)
$H(x,y)$
$\sim 8L_c$
(b)
λ
$\eta(x,y,t)$
$\sim 0.4L_c$
$h(x,y)$
(c)
$\leq -3\sqrt{\langle h^2\rangle}$
$-\sqrt{\langle h^2\rangle}$
0
$\sqrt{\langle h^2\rangle}$
$\geq 3\sqrt{\langle h^2\rangle}$
0.8
y (m)
0
0
1
x (m)
3
4

FIGURE 2.2: (a) A schematic diagram of a piece of an exemplar thin non-uniform elastic plate under consideration. Thickness and its variation are greatly exaggerated for representational purposes. (b) The plate carries a pulse with a predominant wavelength $\lambda \ll L_c$, where L_c is the correlation length of randomness. (c) The randomness field $h(x,y)$ as a colormap, with $\langle h^2\rangle = 9.06\times10^{-4}$, $L_c = 0.1$ m.

$H(x,y) = H_0(1-h(x,y))$ where H_0 is the nominal thickness and $\langle h\rangle = 0, \langle h^2\rangle \ll 1$. Assume that $h(x,y)$ is a random field with zero mean and isotropic spatial correlation characterised by correlation length $L_c \gg \lambda$, the wavelength of interest. While the results are developed here for a plate with non-uniform thickness, the results can readily be generalised for plates with other non-uniform material properties as long as the non-uniformity is small.

One approach towards studying this problem would be to solve the above wave equation with random correlated thickness. However, an analytical solution of this problem is intractable for a random thickness field. Very few solutions of the biharmonic wave equation are known, even for simple geometry, boundary conditions and uniform flexural properties. Analytical solutions exist mostly for homogeneous plates of simple geometry (e.g. rectangular or circular) and simple boundary conditions on the edges (e.g., opposite ends simply supported). This gives us some perspective on the mathematical difficulty involved. Wave propagation for infinite uniform elastic plates is straightforward, whereas analysis for a non-homogeneous medium governed by the bi-harmonic equation is intractable, by contrast.

An alternative analytical approach is that of the equivalent ray dynamics problem—an approach that is taken here. It is the preferred analytical approach taken in other branched flow problems too. Ray dynamics (also called geometric optics) is an abstraction of the full wave dynamics problem which captures a lot of the essential physics of the problem and often enables further analysis, at the cost of losing some physical details of wave propagation. A ray tracks the propagation of a wavefront or the 'locations of constant phase'. For a ray approximation to be valid, the properties of the underlying field must vary *slowly* as compared to the wavelength under consideration i.e. the 'feature sizes' must be much larger than the wavelength. Since $\lambda \ll L_c$, the underlying properties $D,\ \rho,\ E,\ \nu$ and H are *slowly* varying functions of x, y, and hence, we can use the WKB/eikonal approximation to obtain the ray equations for a non-uniform thin plates as follows [104]:

$$\partial_\tau \mathbf{x} = (D/\rho H)^{1/2}\mathbf{k}/\omega, \qquad \partial_\tau \mathbf{k} = -\frac{1}{4}(\rho H/D)\nabla(D/\rho H), \tag{2.7}$$

where, ω is the angular frequency associated with the wavelength of interest, $\tau = \omega t$ is the re-scaled time variable[2], $\mathbf{x} = [x\ y]^T$ is the spatial location of the ray, and $\mathbf{k} = [k_x\ k_y]^T$ is the two dimensional wave vector.

A schematic representation of the structure under consideration is shown in Figure 2.2(a). Figure 2.2(b) shows the scale of the typical wavelength relative to the correlation length of the randomness field. Figure 2.2(c) is a plot of an exemplar $h(x, y)$. The spatially isotropic correlated nature of the randomness field is apparent[3].The relevant length scales of the problem are related as $H_0 \sim H \ll \lambda \ll L_c$. The first part of the inequality permits us the use of thin plate theory and the second inequality, also called the geometric optics limit, permits us the use of the WKB/eikonal approximation to derive the ray equations.

We can introduce the constant $\gamma^2 = \frac{EH_0^2}{(1-\nu^2)\rho}$ to rewrite $D/\rho H = \gamma^2(1 - h(x, y))^2$ to rewrite the ray equations as:

$$\partial_t \mathbf{x} = \gamma(1 - h)\mathbf{k}, \qquad \partial_t \mathbf{k} = \frac{\omega}{2}\frac{\nabla h}{(1 - h)}. \tag{2.8}$$

Since the medium is weakly scattering, the paraxial approximation can be applied. Under this assumption, reduction in the number of coupled equations in the system is possible by noting that the wavelength in the main propagation direction will change negligibly. Hence the rays travel in the main propagation direction with approximately constant speed and the wavenumber in the main propagation direction does not change appreciably from its initial value. The simplified system of ray equations after applying the paraxial approximation is:

---

[2] This is only one of the many allowable forms that τ can take. However, these choices will not alter the claims made in the work. This will be elaborated on in the next chapter.

[3] Details about how this field is generated is covered in section 2.5

$$\partial_t y = \gamma(1-h)k_y, \qquad \partial_t k_y = \frac{\omega}{2}\frac{\partial_y h}{1-h} \tag{2.9}$$

The above pair of equations can be treated as a pair of *nonlinear* ODEs for dependent variables $y(t)$ and $k_y(t)$ as functions of the independent variable time t.

Since we are interested in the average behaviour of such a system as opposed to a specific instance, the equations can be further simplified by replacing the correlated field $h(x,y)$ and its partial derivatives with (temporally) uncorrelated white noise terms (say $\Gamma_1(t)$ and $\Gamma_2(t)$). The properties of the field itself are encoded in a pre-factor which is obtained by ensuring that the integral of the correlation function is conserved. The details of this step can be found in [105]. The resulting simplification can be mathematically expressed as

$$\partial_t y = \gamma(1-h_0\Gamma_1(t))k_y, \qquad \partial_t k_y = h_1\Gamma_2(t) \tag{2.10}$$

where $h_1 = \frac{\omega h_0}{\sqrt{2}L_c}$, $h_0 = \frac{\pi}{2c}\langle h^2\rangle L_c$. This is a nonlinear Langevin equation in two dimensions (y, k_y) with multiplicative noise. The time evolution of the probability density function $P(y, k_y, t)$ of this stochastic differential equation is given by its Fokker-Planck equation [115]:

$$\partial_t P(y,k_y,t) = \left(-\gamma k_y\partial_y + \frac{\gamma^2 h_0^2 k_y^2}{2}\partial_{yy} + \frac{h_1^2}{2}\partial_{k_y k_y}\right)P(y,k_y,t). \tag{2.11}$$

Note that $\iint(\bullet)P(y,k_y,t)\,\mathrm{d}y\,\mathrm{d}k_y = \langle\bullet\rangle$, i.e. the expected value of $(\bullet)$ at some time t. Also, note that ∂_t and integration are commutative operators. So, we can multiply Equation 2.11 by y^2, yk_y and k_y^2 and integrate over the entire domain of y and k_y to obtain the temporal derivative of the expected values of these three quantities as

$$\partial_t\langle y^2\rangle = -2\gamma\langle yk_y\rangle + \gamma^2 h_0^2\langle k_y^2\rangle, \quad \partial_t\langle yk_y\rangle = -\gamma\langle k_y^2\rangle, \quad \partial_t\langle k_y^2\rangle = h_1^2. \tag{2.12}$$

These are coupled linear ODEs and can be solved with the initial conditions $\langle y^2\rangle = \langle yk_y\rangle = \langle k_y^2\rangle = 0$, since the wave initially propagates along x direction. This yields

$$\langle y^2\rangle = \frac{\gamma^2\omega^2 h_0^2}{2L_c^2}\frac{t^3}{3} + \frac{\gamma^2\omega^2 h_0^4}{2L_c^2}\frac{t^2}{2}. \tag{2.13}$$

We will ignore the second term on the right hand side as it is higher order in h_0. We seek the expected location of the first focusing event and hence we may set $t \propto \langle l_f\rangle$. For a focusing events to take place, the "forces" acting on the the rays at the extreme end of the ray bundle participating in the focusing event must be very different. For example, these rays must originally have possessed speeds in the transverse direction which have opposing signs. Hence the ray bundles must have originally been separated by a distance whose scale is governed by the correlation length (see [105] for details). Therefore, we set $\langle y_R^2 \rangle \propto L_c^2$ in the above equation and rearrange to get,

$$\langle l_f \rangle \propto L_c \langle h^2 \rangle^{-1/3}. \tag{2.14}$$

The linear scaling with correlation length can be arrived at even directly from simple dimensional arguments, since correlation length is the only length scale in the geometric optics limit.

2.4 Scaling from numerical ray integration

The scaling of l_f with the statistical properties of the randomness field is investigated by numerical integration of either Equation 2.8 or Equation 2.9[4] using a forward Euler method. Multiple rays[5], equi-spaced along the y axis are launched from the left edge of the plate with dimensions $L_x \times L_y$. They all have initial condition $x(0) = 0, k_x(0) = 2\pi/\lambda, k_y(0) = 0$.

As the rays propagate, those that were initially parallel to the propagation direction begin to scatter due to inhomogeneities in the thickness of the plate. Some rays eventually cross over causing focusing events as seen circled in Figure 2.3. All lengths are normalised with reference to the correlation length of 0.1 m and indicated with a tilde.

As has been shown, from the above analysis, the expected location of the first caustic due to branched flows is independent of material and geometric parameters of the plate under consideration as long as $H_0 \ll \lambda$. Nonetheless, parameter values need to be chosen to run numerical ray integration and finite element wave elastodynamics simulations. The parameters chosen for results reported here are tabulated in Table 2.2. It must be emphasised that the presented results are universal and therefore robust under a different choice of parameters, as long as the assumptions and qualifications noted above are satisfied.

These first focusing events can be numerically detected (see Figure 2.4) as the location where the curve of position versus wavenumber in the y-direction first becomes multi-valued [116]. In the instance shown in Figure 2.3, the location of the first

---

[4] Both of them will yield similar results on numerical integration. We use Equation 2.8 in this chapter. There are some subtle differences at higher values of $\langle h^2 \rangle$ which have been detailed systematically in the next chapter.

[5] We used 300 rays for results reported here. Since $L_y/L_c \ll 300$, we can be confident that we have enough rays to capture branched flow behaviour correctly. We numerically studied different spacing between the rays too. There was no appreciable change in the location of the detected caustics as long as the number of rays was sufficiently larger than L_y/L_c.

Variable Name	Symbol	Units	Value(s)
Young's Modulus	E	MPa	**200**
Density	ρ	$\mathrm{kg\,m^{-3}}$	**7800**
Poisson's Ratio	ν	1	**0.3**
Correlation length	L_c	m	**0.1**, 0.07, 0.15
Wavelength	λ	m	**0.01**, 0.007, 0.015
Nominal thickness	H_0	m	**0.001**
Width of the plate	L_y	m	**0.8**
Length of the plate	L_x	m	4, 8 -depending on $\langle h^2 \rangle$

TABLE 2.2: List of parameters used in numerical ray integration and FE simulations for all the results presented here. Unless stated otherwise, it may be assumed that the parameter values in bold face were used.

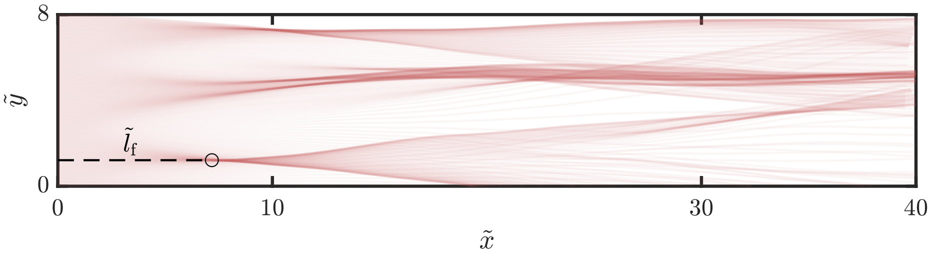

FIGURE 2.3: Evolution of rays in a plate with $\langle h^2 \rangle = 4.24 \times 10^{-4}$. Individual rays are plotted as translucent curves. Hence, caustics or focusing events, which correspond to overlapping rays, appear as regions of higher intensity. The location of first focusing is detected numerically (circular marker).

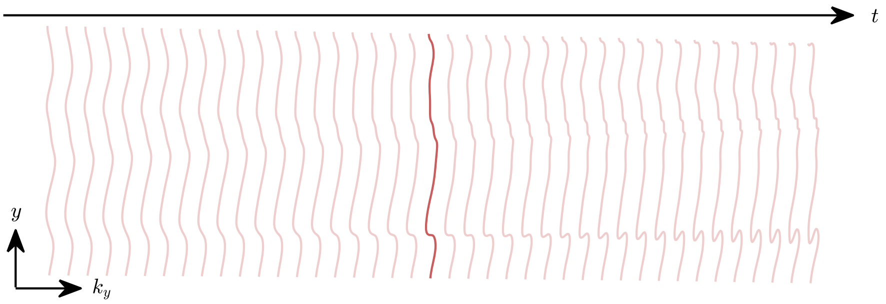

FIGURE 2.4: Temporal evolution of the $k_y - y$ curve. The location of the first caustic is detected by finding the instance where the $k_y - y$ curve become multi-valued (show in dark red here).

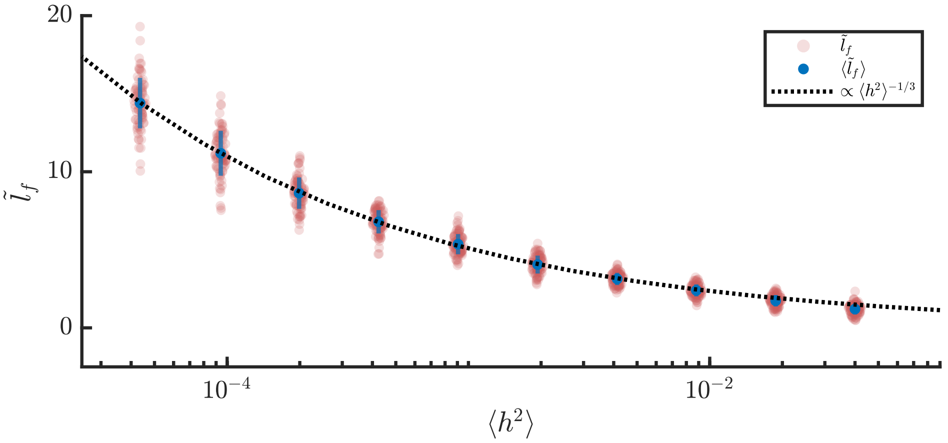

FIGURE 2.5: Scaling of the location of the first caustic location with $\langle h^2 \rangle$. The location of first focusing point (red translucent points) obtained from ray simulations. Mean $\langle \tilde{l}_{\mathrm{f}} \rangle$ of each cluster is indicated by blue markers and a 2-standard-deviation width centered on the mean is indicated by a vertical blue line. The scaling $\langle \tilde{l}_{\mathrm{f}} \rangle \sim \langle h^2 \rangle^{-1/3}$, indicated by the black dotted line on a semi-log plot, agrees extremely well with the simulations.

focusing event has been indicated with a circular marker and l_f is the distance of the first caustic from the left edge.

To study the scaling of $\langle l_f \rangle$ with $\langle h^2 \rangle$, 10 different values of $\langle h^2 \rangle$ ranging from 0.04 to 4.36×10^{-5} were considered–a range spanning 3 orders of magnitude. For each of the 10 values of $\langle h^2 \rangle$ considered, 80 different realisation of the random field h are obtained. They are, then, used for numerical ray integration and l_f is obtained numerically using the procedure described above. Each of these data points is plotted in a bee-swarm plot with translucent red dots in Figure 2.5. For each value of $\langle h^2 \rangle$ considered, $\langle l_f \rangle$ is shown using blue dots along with a blue line indicating one standard deviation in either direction. The dependence of $\langle l_{\mathrm{f}} \rangle$ on $\langle h^2 \rangle$, thus obtained, is in excellent agreement with Equation 2.14 (shown in Figure 2.5 as a dotted black line). Note that the x-axis in Figure 2.5 has a logarithmic scale.

In the geometric optics limit, the only length scale in the problem is the correlation length and therefore, $\langle l_f \rangle$ is expected to scale linearly with the correlation length L_{c}, from simple dimensional arguments. This is confirmed by the analysis presented above. Figure 2.6 shows the scaling of the expected location of the first caustic with the correlation length of the randomness field. The values of $\langle l_f \rangle$ obtained from ray integration with a reference of correlation length $\tilde{L}_{\mathrm{c}} = 1$ (shown with red circular markers) are used to make predictions (dotted lines), assuming a $\langle l_f \rangle \sim L_{\mathrm{c}}$ scaling, for two other correlation lengths $L_{\mathrm{c}} = 0.7, 1.5$. It is seen that values of $\langle l_f \rangle$ obtained from numerical ray integration (shown with blue and green circular markers) with correlation lengths shows excellent agreement with the predictions. This confirms the $\langle l_f \rangle \sim L_{\mathrm{c}}$ scaling in Equation 2.14.

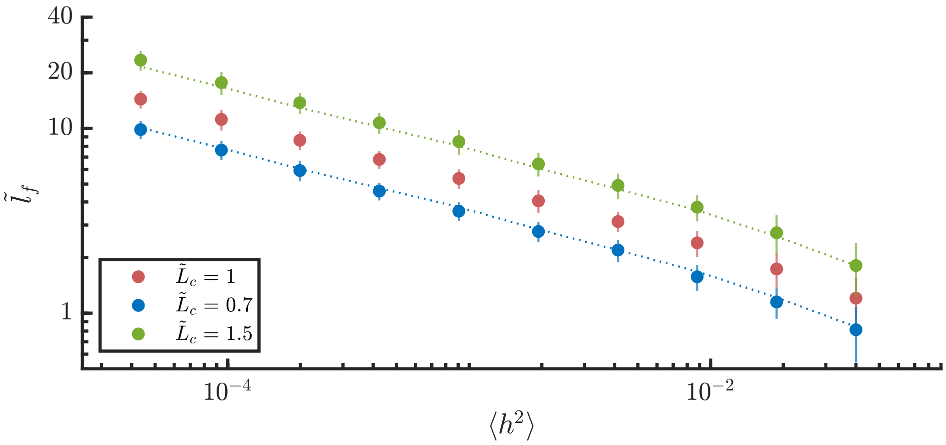

FIGURE 2.6: Using the simulation results of $\tilde{L}_c = 1$ (red dots), and linear scaling with $\tilde{L}_c$, predictions are made for the other two cases (dotted lines) on a log-log plot. These predictions agree well with the scaling obtained from numerical ray integration (green and blue dots for $\tilde{L}_c = 0.7, 1.5$ respectively).

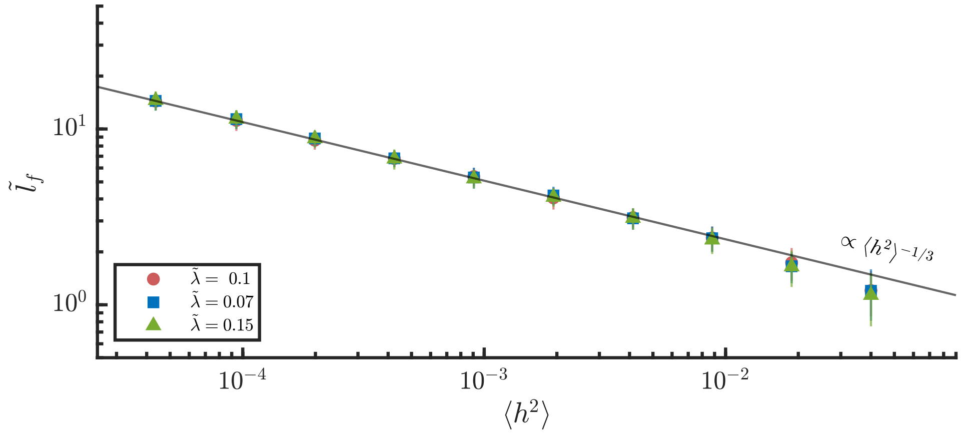

FIGURE 2.7: Scaling of $\langle l_f \rangle$ with wavelength λ. The location of the first caustic is independent of wavelength since even $\sim$ 200% variation in wavelength shows no appreciable change in the expected location of the first caustic.

Finally, as predicted, the expected location of the first caustic is shown to be independent of wavelength (see Figure 2.7). As long as the condition $\lambda \ll L_c$ is satisfied, it is seen that even a $\sim$ 200% change in wavelength leads to no appreciable change in the expected location of the first caustic.

2.5 Remarks on generating the random field

To generate the random thickness field $H(x,y)$, the following relationship is used $h(x,y) = S \times \mathcal{F}^{-1}(\mathcal{F}f \times \mathcal{F}R)$, where $\mathcal{F}$ is the Fourier transform, $f(x,y)$ is the desired auto-correlation function and $R(x,y)$ is a collection of uncorrelated random points drawn from a Gaussian of mean 0 and standard deviation 1 on the grid points at

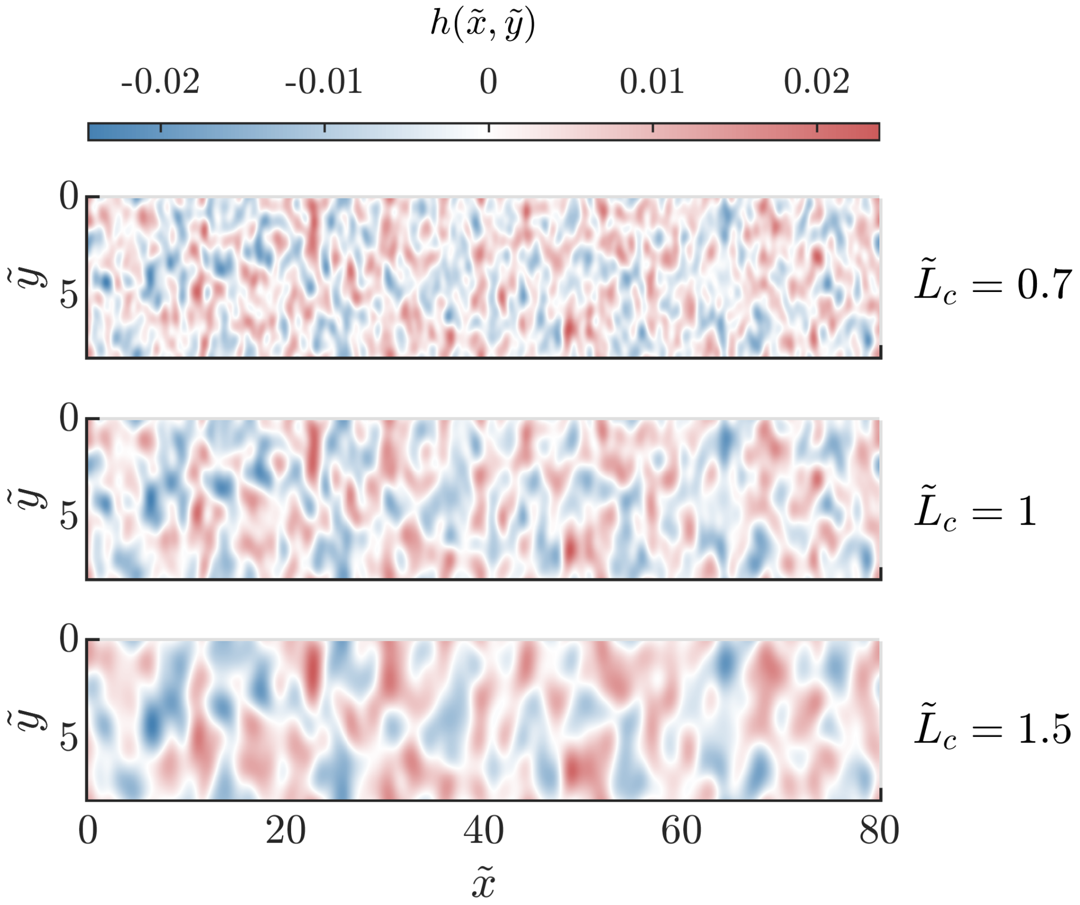

FIGURE 2.8: Examples of random fields $h(\tilde{x},\tilde{y})$ generated for the simulations. Note the effect of change in correlation length $\tilde{L}_c$. In all 3 plots, $\sqrt{\langle h^2 \rangle} = 0.0066$.

which $h(x,y)$ is desired and S is the desired standard deviation of $h(x,y)$. A 2D Gaussian was used as a correlation function with correlation length L_c. This is coded in MATLAB[6] and used to generate multiple instances of the random field with desired standard deviation and correlation length. Some instances of random fields generated are shown in Figure 2.8. The effect of changing correlation length can be clearly seen.

The emergence of branched flows and the associated scaling is independent of the auto-correlation function chosen for the random field. This is shown to be the case in the next section. The only requirement is that the integral of this function over $\mathbb{R}^2$ be well-defined. This is has been noted in extant literature [49].

---

[6] Based on a freely available code (`https://github.com/wulx/dwell2/blob/master/rsgeng2D.m`), suitably modified by the author. The code was validated before use, by ensuring that the output random field has the expected autocorrelation and variance.

2.6 Scaling from finite element simulation of wave elastodynamics

While the WKB/eikonal approximation, based ray formulation presented in section 2.4, is physically justified for the specific problem of interest, it does not capture some finer details of the full wave dynamics –dispersion being a primary example. Hence, finite element modelling based transient elastodynamics simulations using shell elements were employed to independently explore branched flows in elastic plates of randomly varying properties. Consider a thin rectangular plate of inhomogenous thickness and dimensions $L_x \times L_y$. The main propagation direction is along the x-axis. The length in this direction is $L_x(\gg L_y)$. As before, the thickness of the plate is given by $H(x,y) = H_0(1 - h(x,y))$ where $h(x,y)$ is a random field with zero mean and isotropic spatial correlation length L_c. The MATLAB code used to generate random fields of the specified parameters for numerical ray integration is also used to produce random fields for FE simulations. The field is saved as a file and used to specify the thickness at each node in FE simulation.

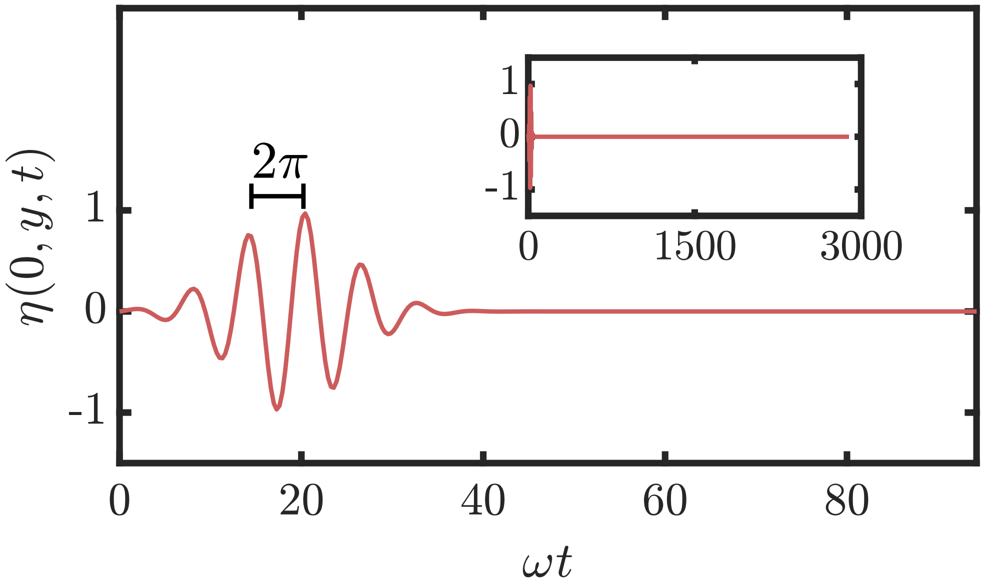

FIGURE 2.9: A plot of excitation applied on left edge of the plate under consideration. The excitation consists of a one short single pulse near $t = 0$. The pulse consists of a sinusoid of angular frequency ω modulated by a Gaussian. Hence, the excitation is nearly 'monochromatic'. From the inset it can be seen that the pulse is an initial sharp excitation.

A pulse with carrier frequency ω that is modulated by a Gaussian envelope is launched at the left edge (see Figure 2.9). This is a fairly 'monochromatic' excitation. This can be confirmed by looking at the Fourier Transform (see Figure 2.10) of the pulse and noting that most of the power in the signal is at or around the carrier frequency. The ratio of the 3 dB bandwidth to the carrier frequency is around 0.25. The

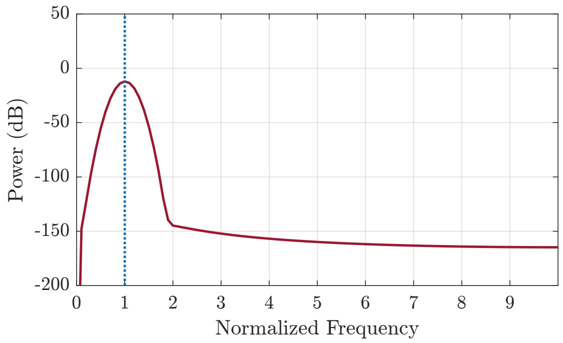

FIGURE 2.10: Fourier Transform of the pulse excitation show in Figure 2.9. The x-axis is frequency normalised with respect to the carrier frequency and the limits of the x-axis are governed by the Nyquist frequency of the signal. Note that most of the power in the signal is at or near the carrier frequency.

excitation thus provided resembles the motion of a rug transversely shaken at the left end. An initially plane wavefront with a predominant wavelength $\lambda \approx 2\pi\sqrt{\beta}\omega^{-1/2}$ thus propagates from left to right. Given that the line source on the left edge provides a transverse excitation, only bending modes are expected to be appreciably excited.

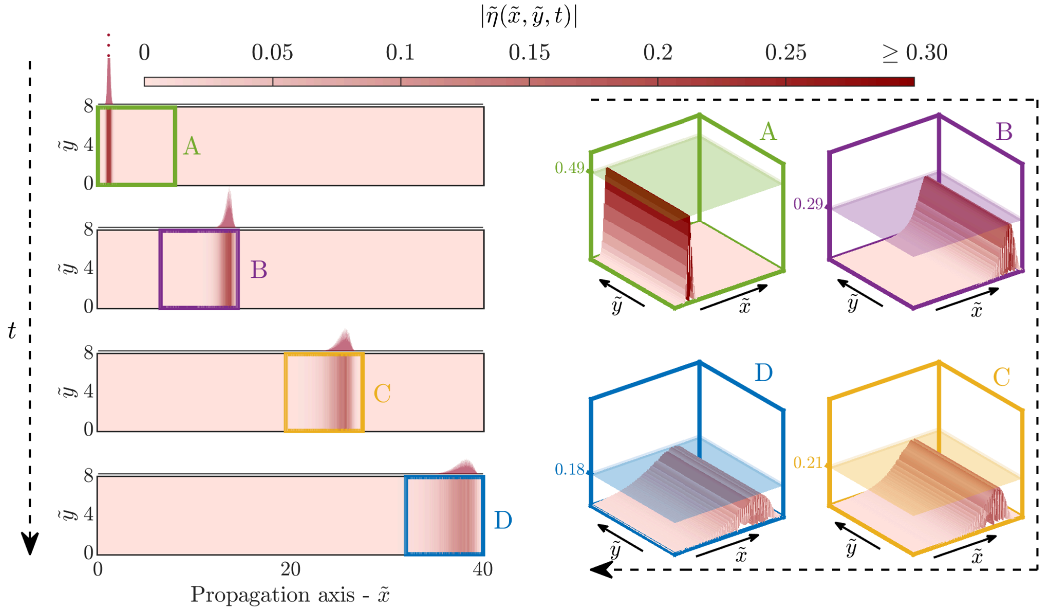

FIGURE 2.11: Spatio-temporal evolution of a Gaussian wave packet in a homogeneous plate. Transverse displacement of a thin homogeneous plate excited at the left edge by a pulse. Dispersion leading to a widening of the initially 'sharp' wavefront is apparent. The highest amplitude (marked by semi-transparent colored planes) at each time instant decreases monotonically. Branched flow is not observed.

To appreciate the effect of spatially correlated randomness, it is instructive to first consider, as a benchmark, the evolution of the wavefront produced by the excitation described above in a *uniform* plate (i.e. $\langle h^2 \rangle = 0$). Figure 2.11 shows the spatio-temporal evolution of the initially planar Gaussian pulse in this uniform plate, obtained using finite element elastodynamics simulations. The four panels on the left

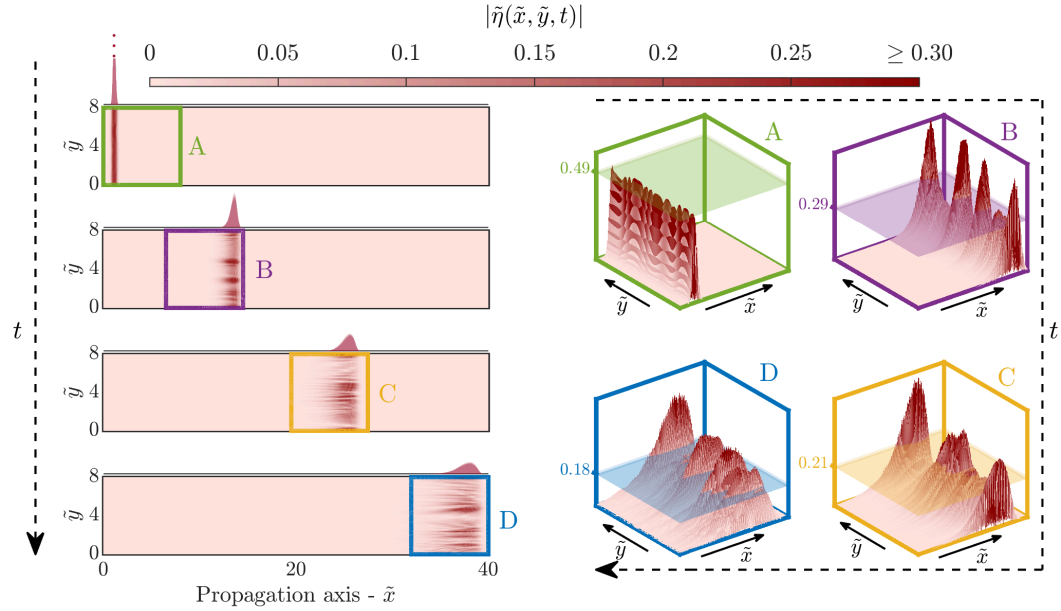

FIGURE 2.12: Spatio-temporal evolution of a Gaussian wave packet. Transverse displacement of a thin inhomogeneous plate excited at the left edge by a pulse. The emergence of branches i.e rapid variation in wave amplitude in the $\tilde{y}$ direction, is seen after sufficient temporal evolution. The wave front, at different points of time, is zoomed into and shown on the right. The transparent plane marks the highest amplitude seen in a perfectly homogeneous plate, under the same excitation, at the corresponding instant of time. Branched flow disrupts the monotonically decreasing trend of highest amplitude. The randomness field describing the thickness has the standard deviation $\sqrt{\langle h^2 \rangle} = 0.0301$.

show the amplitude of transverse displacement at four successive instants of time (top to bottom; x-y axes are normalised). Regions of highest displacement at each successive time instant are indicated by square boxes labelled A, B, C, D. Widening of the wavefront due to the dispersive nature of the medium is apparent. This can also be seen from the energy density plots (shown in light red above each panel in Figure 2.11). A monotonic reduction is also seen in the highest amplitudes of the wavefront as it propagates (see the 3D plots on the right). This follows from energy conservation since the widening of the wavefront must accompany a reduction in amplitude. The maximum amplitude seen at each time instant is shown in the plots on the right with transparent planes. The levels of these planes decrease monotonically with time, as expected. These planes would be used as amplitude references to illustrate the effect of non-uniformity on wave propagation.

Figure 2.12 shows the spatio-temporal evolution of the initially planar wavefront on an exemplar *non-uniform plate* ($\langle h^2 \rangle = 9.06 \times 10^{-4}$) with the same nominal properties as those of the uniform plate considered above. The widening of the wavefront as expected from the dispersive character of flexural waves in plates is clearly seen. However, note that unlike in the case of a uniformly thick plate, the highest amplitude observed at each successive time instant does not decrease appreciably. This can be

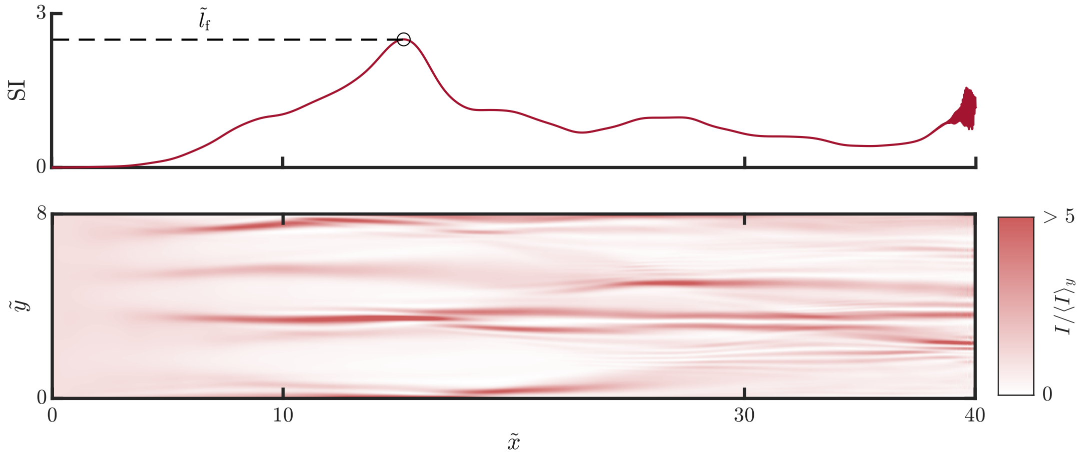

FIGURE 2.13: (Top) Plot of Scintillation Index (SI) corresponding to the case plotted in the bottom figure. It can clearly be seen that SI captures the variations in intensity (averaged along $\tilde{y}$). The location of the first focusing event is detected by finding the location (in the propagation direction) of the first significant peak in SI indicated by a circular marker in the plot. (Bottom) A plot of time-integrated intensity (normalised by mean along $\tilde{y}$). The emergence of focusing events is quite apparent. Note that the fluctuations are much higher than 5, but the scale is cut off at 5 to preserve detail in other regions. This corresponds to one of the simulations for $\tilde{L}_c = 1$, $\tilde{\lambda} = 0.1$, $\sqrt{\langle h^2 \rangle} = 0.0301$.

clearly seen in the 3D plots on the right-hand side by comparing the observed amplitudes to the colored planes which are the amplitude reference from the uniform plate at the same instant in time. This is due to the emergence of branches that is attributed to the scattering of the plane wave by the non-uniformity. These branches interfere and form locations of amplitudes much higher than what one may expect from the dispersive wave dynamics in the equivalent homogeneous medium. Regions with amplitudes that are lower than that for the homogeneous case also appear, as expected from energy conservation.

A few variables that will help in finding the location of the first focusing event will now be defined. This is following a strategy presented in [49, 105] for tsunami waves. Let the transverse deflection be given by $\eta(x, y, t)$. Define the time-integrated intensity as

$$I(x, y) = \int_0^T \eta^2(x, y, t)\mathrm{d}t. \tag{2.15}$$

Admittedly, $I(x, y)$ does not have the dimensions of intensity as traditionally defined in acoustics. It is named time-integrated intensity following the literature of branched flows. The above definition suggests that $I(x, y)$ will have peaks at the location of random focusing events. Since interest is in the distance of such events from the point of launch in the main propagation direction, we can define a quantity called the *scintillation index* [117], based on the variance of $I(x, y)$ in y-direction normalised by

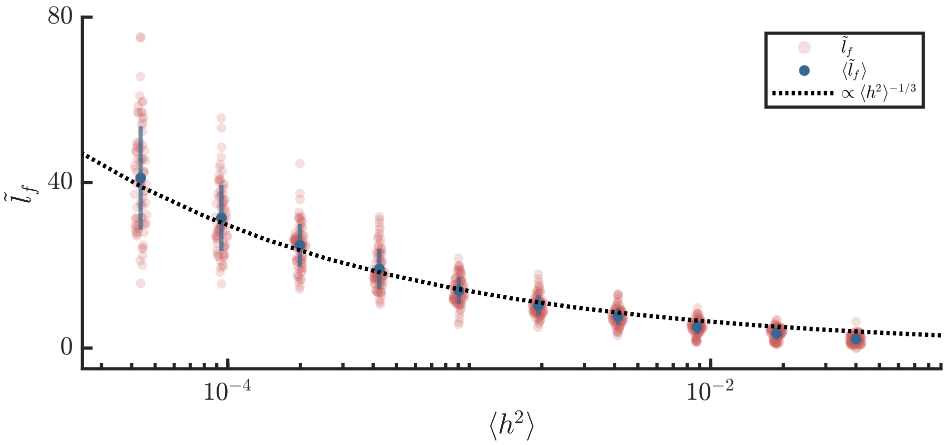

FIGURE 2.14: A plot of the location of first focusing events (red points). Mean $\langle \tilde{l}_f \rangle$ of each cluster is indicated by blue markers and a 2 standard deviation width centered on the mean is indicated by a vertical line. The scaling relationship of $\langle \tilde{l}_f \rangle \propto \langle h^2 \rangle^{-1/3}$, indicated by the black dotted line, agrees excellently with the simulations.

the mean in the same direction:

$$SI(x) = \frac{\langle I^2(x,y) \rangle_y}{\langle I(x,y) \rangle_y^2} - 1. \tag{2.16}$$

This is a quantity that has local peaks at the location of focusing events. See Figure 2.13 (bottom) for a representative plot of $I(x,y)$ normalised with respect to the average along the y axis. Focusing events due to branched flow, which lead to large amplitudes, are clearly visible. In Figure 2.13 (top), the scintillation index, $SI(x)$ derived from the integrated intensity plot shown can be seen. The location of first prominent peak of the scintillation index curve is the location of the first focusing event. This is shown with a circular marker on the plot.

For $\tilde{L}_c = 1$ and $\tilde{\lambda} = 0.1$, 80 simulations were performed for the same 'severity' of randomness $\langle h^2 \rangle$ and this was repeated for 10 different values of $\langle h^2 \rangle$ as was executed for numerical ray integration. The results shown in Figure 2.14 confirm that the scaling of $\langle l_f \rangle$ (blue circular markers) with $\langle h^2 \rangle$ agrees very well with Equation 2.14 and the scaling seen from numerical ray integration.

Similar simulations were run to study the dependence of $\langle \tilde{l}_f \rangle$ upon $\tilde{\lambda}$ next. For the same correlation length of $\tilde{L}_c = 1$, propagation for three different wavelengths of $\tilde{\lambda} = 0.07,\ 0.1,\ 0.15$ was studied (see Figure 2.15). For clarity, a logarithmic scale on the y axis is used, unlike Figure 2.14. In this "log-log" scaling the reference $\propto \langle h^2 \rangle^{-1/3}$ appears as a straight line. Also, only the mean and 2 standard deviation widths are shown in the plot for clarity. Logarithmic scale greatly exaggerates distances and

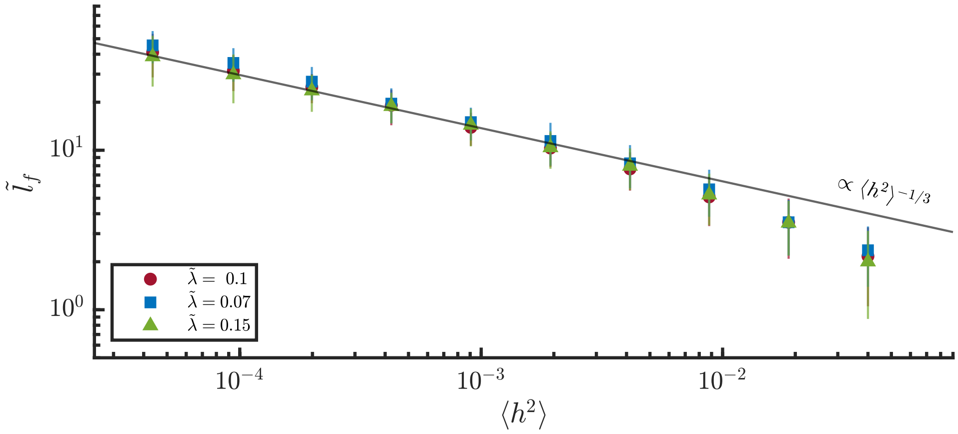

FIGURE 2.15: A plot of $\langle \tilde{l}_f \rangle$ vs $\langle h^2 \rangle$ for three wavelengths $\tilde{\lambda} = 0.1,\ 0.07,\ 0.7$ obtained from FE simulations. The scaling relationship of $\langle \tilde{l}_f \rangle \propto \langle h^2 \rangle^{-1/3}$, indicated by the black dotted line, agrees excellently with the simulations. This also demonstrates that $\langle \tilde{l}_f \rangle$ is independent of the wavelength as long as the wavelength is much smaller than the correlation length. Please note that unlike Figure 2.14, which has a y axis with a linear scale, the y axis in this plot is in log scale. This partially explains the apparent departure of the values of $\langle \tilde{l}_f \rangle$ from the predicted trend as log scale plots exaggerate distances at lower values. Nonetheless, some of the departure is also expected since the scaling relationship Equation 2.14 is predicated on weak scattering, a requirement that begins to be violated at higher values of $\langle h^2 \rangle$.

therefore the deviation from reference towards the lower end[7]. This partially explains the deviation from the reference along with the fact that at higher $\langle h^2 \rangle$, the "weak scattering" requirement for the scaling to hold in the media starts to be violated.

Also studied is the relationship between $\langle \tilde{l}_f \rangle$ and the correlation length. Simulations were carried out by fixing the wavelength at $\tilde{\lambda} = 0.1$ and ascertaining $\langle \tilde{l}_f \rangle$ for values of $\tilde{L}_c = 0.7,\ 1,\ 1.5$. These show the expected linear trend with correlation length as seen in Figure 2.16. Taking the simulation for $\tilde{L}_c = 1$ as reference, $\langle \tilde{l}_f \rangle$ values from this simulation are multiplied by 0.7 and 1.5 for $\tilde{L}_c = 0.7$ and 1.5 respectively to obtain predicted values based the scaling relationship given in Equation 2.14. These are indicated with dotted lines in Figure 2.16. One can see that $\langle \tilde{l}_f \rangle$ obtained from simulation for $\tilde{L}_c = 0.7$ and 1.5 are in excellent agreement with the predicted values.

As mentioned in the previous section, the appearance of branched flows and associated scaling is largely independent of the autocorrelation function underlying the correlated random field. All the results present here are based on random field with a Gaussian autocorrelation. However, some FE elastodynamics simulations with randomness fields which have a power law autocorrelation function of the form $(1 + (x^2 + y^2)/L_c^2)^{-2}$ were also run. The scaling remains unaffected as can be seen in Figure 2.17.

---

[7] For example, note how the standard deviation may appear to be greatest for highest $\langle h^2 \rangle$ and smallest for lowest $\langle h^2 \rangle$ in Figure 2.15. But it can be seen from Figure 2.14, where the y-axis is linear that the standard deviation has the opposite trend with respect to randomness level $\langle h^2 \rangle$.

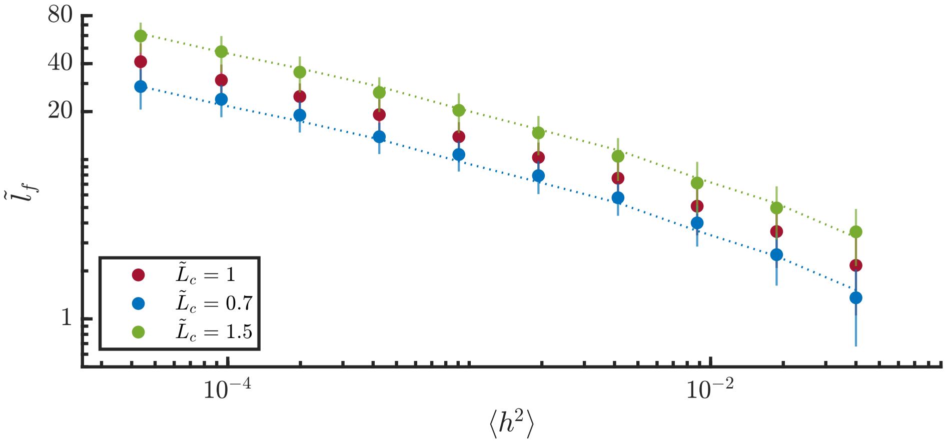

FIGURE 2.16: A plot of $\langle \tilde{l}_f \rangle$ vs $\sqrt{\langle h^2 \rangle}$ for three correlations lengths $\tilde{L}_c = 1,\ 0.7,\ 1.5$ obtained from FE simulations. Taking simulations of $\tilde{L}_c = 1$ as reference (red circular markers), dotted lines (blue and green) are plotted as predictions (for $\tilde{L}_c = 0.7$ & 1.5 respectively) assuming $\langle \tilde{l}_f \rangle$ scales linearly with $\tilde{L}_c$. It is seen that the FE simulations (green and blue circles) are in excellent agreement with the predicted trend.

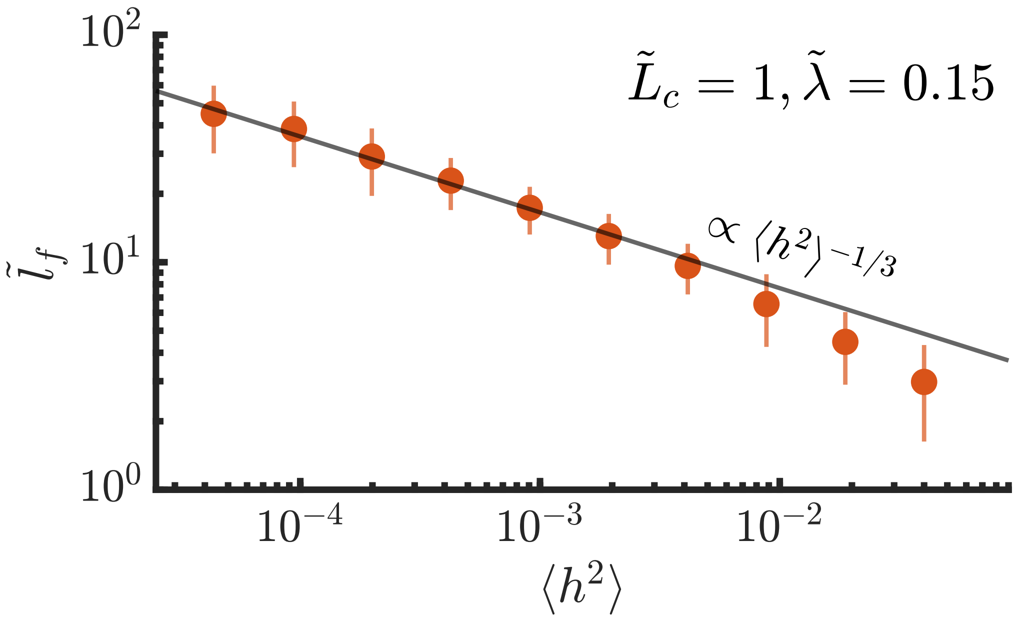

FIGURE 2.17: Scaling of location of caustics for power law correlation function. Finite element elastodynamics simulations confirm that using a power law auto-correlation function of the form $(1 + (x^2 + y^2)/L_c^2)^{-2}$ instead of a Gaussian auto-correlation to construct $h(x, y)$ does not affect the predicted scaling of the location of the first caustic. Note that this a log-log plot. Marker indicates the mean. A two-standard-deviation width centered at the mean is indicated by a vertical line.

After multiple branching, the fluctuations in $I(x, y)$ are expected to saturate [52] and hence $SI(x)$ is expected to stabilise towards a saturated value of 1. This may not necessarily happen in our system due to reflections from the long edges which have a "free" boundary condition. Commercial FE packages do not have any implementation of non-reflecting or infinite domain elements which couple with shell elements. Nonetheless, it is not expected to affect our simulations since the interest is only in the location of the first random focusing events and given that the study is on a weakly scattering case, these events are expected to occur before significant reflection from the boundary. Reflections from the two edges parallel to the main propagation direction may, however, partially explain the deviation from the expected scaling in regions of relatively higher $\langle h^2 \rangle$.

The l_f values obtained by FE elastodynamics simulations tend to be larger than those from numerical ray integration for the randomness fields with identical statistical properties (for example, compare l_f values in Figure 2.5 and 2.14). This is explained by the fact that l_f is obtained from numerical ray simulations by detecting the *onset* of a caustic/focusing event whereas in FE elastodynamics simulations l_f is obtained by finding locations of high amplitude. Since high amplitudes do not occur not at the onset of caustics, but further along, this leads to an appreciable difference between l_f values obtained from the two numerical methods discussed here. However, this does not affect the *scaling* of the location of the first caustics with the statistical properties of the randomness field. This 'mis-match' has been noted, for the case of Tsunami waves too, in [105].

Note that unlike the classical wave equation, the biharmonic wave equation which governs transverse wave motion of thin plates is strongly dispersive, this means that the wave pulse will "spread out" spatially as it progresses. If the wave evolves for too long it may take deflection values which are numerically vanishing. This may lead to wrong conclusions. This is not a problem one has to contend with when looking at non-dispersive system. Nonetheless, since the objective of the study is the *first* focusing event, this not particularly egregious.

2.7 Wave propagation in uncorrelated vs correlated random media

In this chapter, we reported the existence of branched flows of flexural waves in thin elastic plates. It is remarkable that small random variations in the thickness cause extreme amplitudes to develop. This is due to *correlated* randomness causing the initially planar wavefront to focus which leads to high amplitudes. The effect of spatial correlation in wave transmission can be best appreciated when compared to the case where the 'severity' of randomness ($\langle h^2 \rangle$) is the same however there is no discernible spatial correlation[8]. Consider the temporal evolution of the 'pulse' described previously (Figure 2.9) in plates whose thickness has (a) no randomness, (b) uncorrelated randomness, and (c) spatially correlated randomness (see Figure 2.18 for plots of $h(x, y)$). The two random fields have the same 'severity' of randomness $\sqrt{\langle h^2 \rangle} = 0.0301$, however, one has no spatial correlation and the other has an isotropic spatial correlation with $\tilde{L}_\mathrm{c} = 1$.

The displacement plot after some time t_r for each case is shown in Figure 2.19. As expected, the plate with no non-uniformity retains a planar wavefront. Dispersion has 'widened' and 'flattened' out the initially sharp and short pulse. In the plate with uncorrelated randomness, one can see that the planar wavefront has been slightly disturbed leading to small local peaks in amplitude. However, the highest amplitude seen is not appreciably different from the displacement seen in the uniform plate. The scattering observed here, from weak uncorrelated scatterers, is akin to Rayleigh scattering. The plate with correlated randomness shows an appreciably different displacement profile than the two cases discussed above. Emergence of distinct branches is seen which leads to amplitudes which are more than twice as large as what is seen in the previous two cases.

Figure 2.20 shows the distribution of amplitudes seen at some reference location ($\tilde{x}_\mathrm{r}$) on the $\tilde{x}$ axis (at time t_r). The displacement distribution for waves in the uniform plate at $\tilde{x}_\mathrm{r}$ lies within a narrow band as expected (pink histogram). The introduction of uncorrelated randomness widens this distribution. However, the distribution is still fairly narrow (the distribution in green histogram) compared to the distribution of displacement values seen in the plate with correlated randomness (the blue histogram)[9]. This is attributable to the existence of branched flows. Note the heavy tail seen in distribution of the displacements in the plate with correlated randomness. These 'extreme' amplitudes are the result of focusing events caused by branched flows.

---

[8] Strictly speaking, all random fields would have some correlation length. However, as long as it is much smaller than the wavelength under consideration, the randomness field can be considered effectively uncorrelated as far as the problem at hand is concerned.

[9] Since, this is akin to Rayleigh scattering, an exponential fall off is expected for higher amplitudes. It is not possible to capture this here due to the relative sparseness of the mesh in the $\tilde{y}$ direction. See [50] for a comparison of distribution of amplitudes seen from Rayleigh scattering compared those from branched flows.

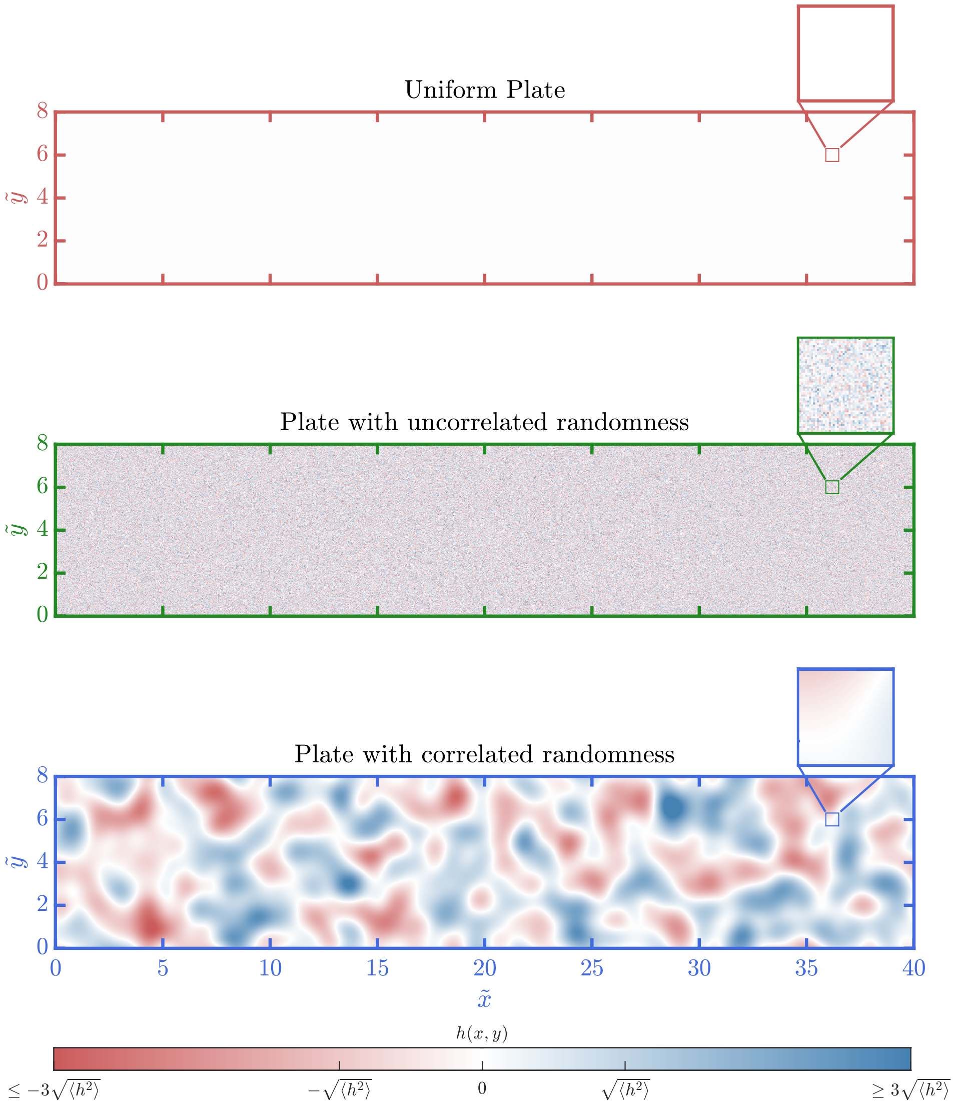

FIGURE 2.18: Colormap plots of $h(x,y)$ for a uniform plate (top), plate with uncorrelated randomness in thickness (middle) and plate with spatially isotropic correlated randomness in the thickness (bottom). Both random fields have the same standard deviation, $\sqrt{\langle h^2 \rangle} = 0.0301$. Zoomed in segments of the randomness are shown as insets.

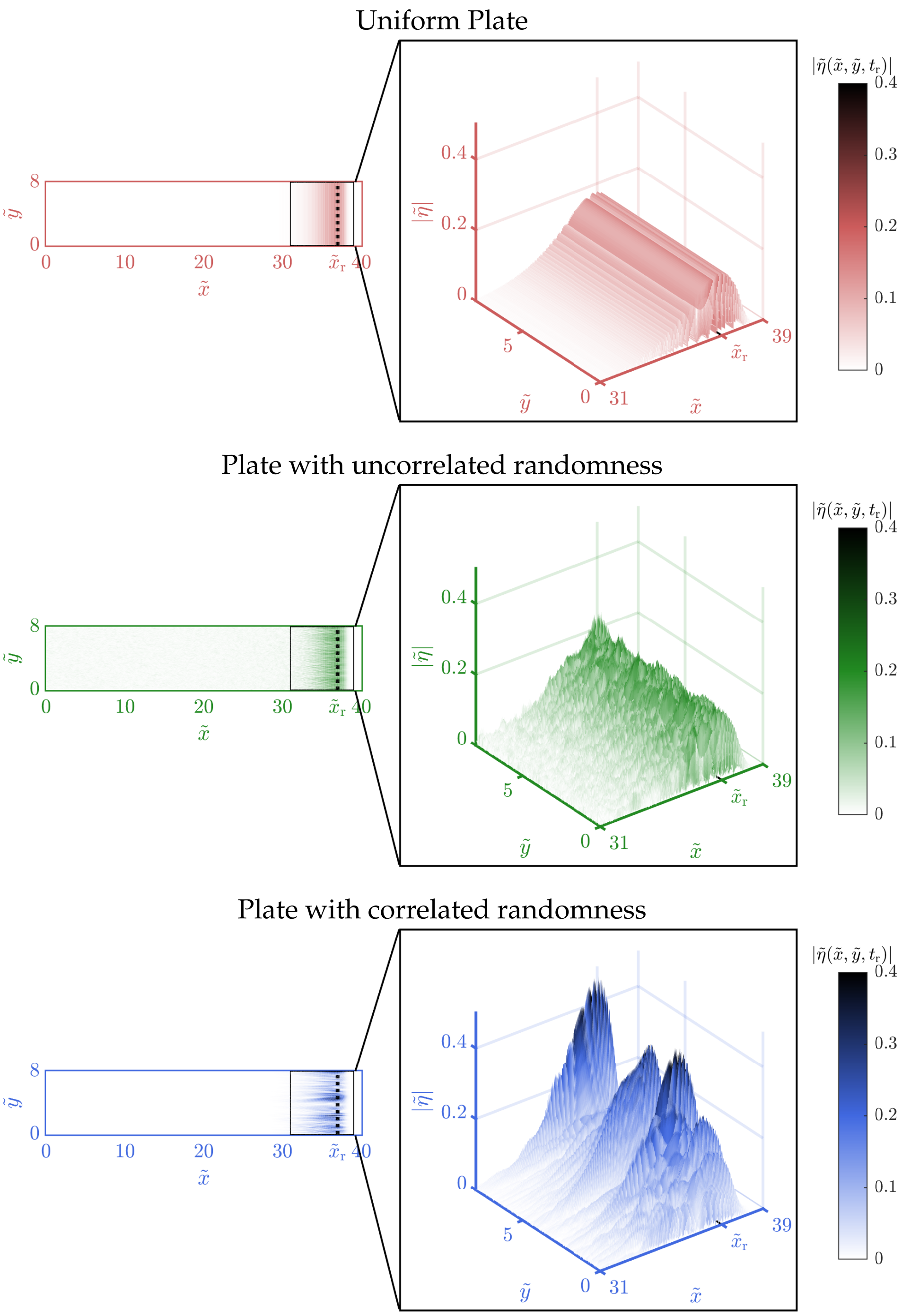
Uniform Plate

Plate with uncorrelated randomness

Plate with correlated randomness

FIGURE 2.19: Displacement profiles after some time $t_{\rm r}$ in the plates with uniform, uncorrelated random, and spatially correlated random thickness. The highest amplitudes seen in the plate with correlated randomness are more than double that seen in the other two cases. The wavefront (locations of highest amplitude) are zoomed into and shown on the right as 3D plots.

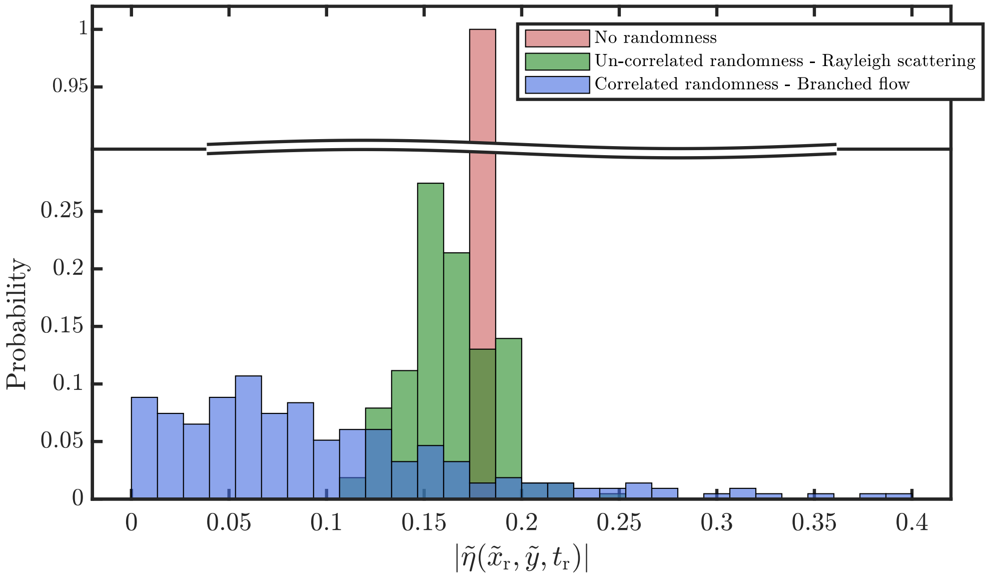

FIGURE 2.20: Distribution of amplitudes observed at time t_r and some reference location ($\tilde{x}_r$) on the $\tilde{x}$ axis. Amplitude distribution in plate with spatially correlated randomness shows a heavy tail.

2.8 Remarks on the FE simulations

- SHELL181 elements [118] were used for the simulations since they allow for specification of thickness at each node. SHELL181 is a sophisticated shell element which has contributions from in-plane (membrane) stresses, through thickness shear, and rotary inertia of the cross-section. These effects were ignored in the analysis. Nonetheless, these effects, while present, are expected to be negligible in the small deflection and $H_0 \ll \lambda$ regime considered here. There are some legacy shell elements in ANSYS which have potential energy contribution from bending and are thus closer to the analytical model that we have considered here. However, they are no longer officially recommended by ANSYS and more importantly, do not allow specification of variable thickness at a nodal level. This is why the SHELL181 elements were chosen for the FE simulations. In some ways, the robustness of the results, despite the use of an FE element which is more sophisticated than the analytical model, speaks to the correctness of our mathematical modeling and assumptions made therein.

- ANSYS linear transient time march was carried out, internally using the Newmark-beta method [119]. ANSYS also applies a small numerical damping with each time step to aid numerical convergence. The typical use case of transient simulations involves temporal evolution of the structure under consideration for a relatively short time period. Hence, this numerical damping does not lead to significant mis-estimation of the displacement values. However, the case studied pertains to a temporal evolution over a larger time scale and hence the default damping factor was seen to produce an 80% reduction of the total energy in the system by the end of the simulations. To mitigate this, a significantly reduced value for the numerical damping was used, from the default value, which lead to a loss of no more than 5% of the total energy in the complete simulation.

- Simulations were carried out on the domain $(\tilde{x}, \tilde{y}) \in [0, 40] \times [0, 8]$ except for the lowest three standard deviations which were done over $(\tilde{x}, \tilde{y}) \in [0, 80] \times [0, 8]$. It can be noted that even for the lowest amount of randomness, $\langle \tilde{l}_f \rangle < 40$, but it was ensured for all simulations that the propagation distance was at least twice as much as the expected value of the first focusing event to avoid biasing the sample. This means that for the highest 7 standard deviations studied, a field of normalised length 40 was sufficient, but for the latter case a field of normalised length 80 was used. This was done due to the computational load associated with running these simulations. But it is apparent that this has not had any significant bias on the sample since there is no discontinuity in the trend of the expected value of first focusing events. This can also be seen by looking at the spread of data in Figure 2.5.

- The latter end of $SI(x)$ and $I(x,y)$ shows some oscillations which are simply numerical "divide by 0" type artefacts since the wave front has not fully reached there before the simulation is terminated. This is confirmed by looking at the actual values of $I(x,y)$.
- The computational expense of running FE simulations is driven up by the peculiarities of the phenomenon one might wish to study. Since it is a study of wave mechanics, the mesh size is driven by the wavelength but the domain size is of the order of the correlation length, a quantity which is, necessarily (for the phenomenon being studied to occur), much larger than the wavelength. Hence this leads to very fine meshes driven by ensuring there are at least 6 mesh points per wavelength in the propagation direction over a large domain driven by a desire to keep the propagation distance at least 40 times the correlation length. This led to meshes which have between half and a few million nodes. Furthermore, the time step of the simulations is driven by the frequency associated with the wavelength of interest, but the duration of the simulation is driven by the time it takes the wave front to travel the propagation distance. The time period of the chosen frequency and the time taken for propagation are many orders of magnitudes apart. This led to simulations with a few thousand time steps. This combination of large mesh size and number of time steps led to simulation times ranging from 20 minutes to 8 hours per simulation on a High Performance Cluster (HPC). For this study, more than 4000 such simulations were run.
- Random fields were generated in the MATLAB environment, FE simulations were carried out on ANSYS APDL and $I(x,y)$ was extracted using a Python script. The author also wrote BASH scripts to automate setup and workflow including queuing jobs on the High Performance Cluster (IRIDIS 5).

More details about the numerical analysis workflow is given in Appendix A.

2.9 Conclusions

The emergence of focusing of bending waves in random thin elastic plates was demonstrated and quantitatively characterised. The scaling of the location of the first focusing event with the mean square randomness of the plate is determined when a pulse is launched from one end of plate. The ray description of the problem, arising from the eikonal equation for plate flexural waves, was reduced to a system of equations consistent with previously known scaling in other physical contexts, viz. $\langle l_\mathrm{f} \rangle \sim L_\mathrm{c}$ and $\langle l_\mathrm{f} \rangle \sim \langle h^2 \rangle^{-1/3}$. The ray equations were then integrated numerically and the results were found to agree with these scaling relationships. The location of the first caustic was found to be independent of the wavelength and the correlation function that describes the disorder. The scaling relationships between the location of focusing, ’severity’ of the disorder, and the correlation length were also obtained by elastodynamic simulations using the finite element method.

This work focused on thin plates where thickness shear effects are insignificant. The existence, or absence, of branched flows in thick plates where the wavelength is comparable to the thickness and, therefore, thickness shear is significant, remains an open question.

The formation of channels suggests the potential of tailoring and shaping wave paths within such elastic waveguides, especially when combined with acoustic metamaterials [120]. Since, particle separation & manipulation [121] involve steering particles to nodal lines, the author anticipates that this work may potentially inform the design of such technologies. While the analysis and computations presented here are restricted to thickness variations, the phenomenon reported here would, in principle, be observed for spatial heterogeneity in material properties such as the modulus of elasticity or density. Results presented here could also have interesting implications to metrology of elastic plates, geophysics and seismology.

There are natural questions about the extent of the universality of branched flow, especially in elasticity. In the next chapter, this question will be explored, in the context of hollow cylindrical shells.

Chapter 3

Flexural waves in random elastic cylinders: branched flows

3.1 Introduction

As mentioned in chapter 2, branched flow [40] is a peculiar behaviour of waves propagating through heterogeneous media with spatially correlated randomness. In the last chapter, we showed that flexural waves in thin elastic plates exhibit branched flow. This raises a natural question about the universality of branched flows in waves carried by elastic structures. In many applications such as health monitoring of buried gas pipes, shells act as waveguides for elastic waves, hence they provide a practical context to understand the relevant physics. Cylindrical shells also provide a domain to study branched flows with neither reflections from the long edges [4] nor 'contrived' periodic boundary conditions [52] at the edges parallel to the main propagation direction, because the domain folds circumferentially onto itself.

Thin shells can be considered a generalisation of a thin plates due to at least one of the principal curvatures being non-zero. This non-zero curvature introduces a coupling between the two in-plane and one transverse displacements. This makes the dynamics of shells different from that of flat plates where transverse displacements are decoupled from the in-plane ones. This coupling also makes the dynamics of shells harder to model. As a result, the formulation of even homogeneous shells continues to be an area of active research. By contrast, a single fourth order differential equation in terms of transverse displacement, given by the Kirchhoff–Love plate model [67, 99, 100], represents a universally-accepted simplest formulation of the dynamics of thin flat plates. Even after ignoring all higher order effects such as

---

[0] Substantial portions of this chapter have been published in "Jose, K., Ferguson, N. & Bhaskar, A. Branched flows of flexural elastic waves in non-uniform cylindrical shells. PLoS ONE **18**, 5: e0286420 (2023)".

transverse shear and rotary inertia of the cross-section, there are numerous models and, therefore, numerous equations of motions of a thin shell with slight variations.

In the case of cylindrical shells, the simplest equation of motion is usually a set of eighth-order differential equations which couple the two in-plane and one transverse displacements. However, unlike flat plates, numerous formulations of varying degrees of accuracy exist. The second chapter of Leissa's report titled "Vibration of Shells" [63], which provides an excellent synthesis of many of these shell equations, is summarised below.

Consider a cylinder of radius R and thickness H_0 which has the long axis along the x-direction and the circumferential direction along s (with units of length). If the axial, circumferential and radial displacement components are given by u, v & η respectively, then the equation of motion of this cylinder can be written as

$$\mathcal{L}\mathbf{u} = 0, \tag{3.1}$$

where $\mathbf{u} = [u \ v \ \eta]^T$ and $\mathcal{L}$ is a differential operator. According to [63], this operator can be written as

$$\mathcal{L} = \mathcal{L}_{\text{DM}} + \frac{H_0^2}{12R^2}\mathcal{L}_{\text{MOD}}. \tag{3.2}$$

Here,

$$\mathcal{L}_{\text{DM}} = R^2 \begin{bmatrix} \left(\partial_{xx} + \frac{(1-\nu)}{2}\partial_{ss} - \rho\frac{(1-\nu^2)}{E}\partial_{tt}\right) & \frac{(1+\nu)}{2}\partial_x\partial_s & \frac{\nu}{R}\partial_x \\ \frac{(1+\nu)}{2}\partial_x\partial_s & \left(\frac{(1-\nu)}{2}\partial_{xx} + \partial_{ss} - \rho\frac{(1-\nu^2)}{E}\partial_{tt}\right) & \frac{1}{R}\partial_s \\ \frac{\nu}{R}\partial_x & \frac{1}{R}\partial_s & \frac{1}{R^2} + \frac{H_0^2}{12}\nabla^4 + \rho\frac{(1-\nu^2)}{E}\partial_{tt} \end{bmatrix} \tag{3.3}$$

where, $\nabla^4 = (\partial_{xx} + \partial_{ss})(\partial_{xx} + \partial_{ss})$, comes from Donnell-Mushtari theory [122–124]. Note that, in Equation 3.2, the $\mathcal{L}_{\text{DM}}$ operator is modified by another linear operator $\mathcal{L}_{\text{MOD}}$. It can be seen from the multiplicative constant that appears with this operator that its effect will be small for thin shells since $H_0 \ll R$.

Different thin shell theories are obtained by changing the $\mathcal{L}_{\text{MOD}}$ operator. For example, to obtain the equations of motions due to Love and Timoshenko [100, 125, 126], one should set

$$\mathcal{L}_{\text{MOD}} = \begin{bmatrix} 0 & 0 & 0 \\ 0 & (1-\nu)R^2\partial_{xx} + R^2\partial_{ss} & -R^3\partial_{xx}\partial_s - R^3\partial_{sss} \\ 0 & -(2-\nu)R^3\partial_{xx}\partial_s - R^3\partial_{sss} & 0. \end{bmatrix} \tag{3.4}$$

To obtain the equations due to Reissner [127] and Naghdi-Berry [128] equations, set

$$\mathcal{L}_{\text{MOD}} = \begin{bmatrix} 0 & 0 & 0 \\ 0 & \frac{(1-\nu)}{2}R^2\partial_{xx} + R^2\partial_{ss} & -R^3\partial_{xx}\partial_s - R^3\partial_{sss} \\ 0 & -R^3\partial_{xx}\partial_s - R^3\partial_{sss} & 0 \end{bmatrix}. \tag{3.5}$$

And to obtain the equations due to Vlasov [129, 130], one must set

$$\mathcal{L}_{\text{MOD}} = \begin{bmatrix} 0 & 0 & -R^3\partial_{xxx} + \frac{(1-\nu)}{2}R^3\partial_x\partial_{ss} \\ 0 & 0 & -\frac{(3-\nu)}{2}R^3\partial_{xx}\partial_s \\ -R^3\partial_{xxx} + \frac{(1-\nu)}{2}R^3\partial_x\partial_{ss} & -\frac{(3-\nu)}{2}R^3\partial_{xx}\partial_s & 1 + 2R^2\partial_{ss} \end{bmatrix}. \tag{3.6}$$

The differences between the modifying operators arise from different approximations that are made while deriving the equations of motion. One of the most common source of difference between thin shell theories is how the ratio of distances through the thickness to the radius are approximated. For this discussion, say this ratio is z/R. This will be much smaller than 1 for thin shells. If z/R terms are neglected in comparison to unity, one gets the equations due to Love and Timoshenko. Dropping the z/R term earlier in the derivation results in the Reissner-Naghdi-Berry equations. If instead, the term z/R in the expression $1/(1 + z/R)$ is approximated by the series expansion $\sum_{n=0}^{\infty}(-z/R)^n$ in the derivation, one obtains the equations due to Vlasov. The equations of motion of a cylindrical shell due to Arnold & Warburton, Sanders, Epstein & Kennard and many others can also be written by choosing an appropriate $\mathcal{L}_{\text{MOD}}$ in Equation 3.2. Thin shell theories are premised on a set of assumptions called "Love's first approximations" [125]. There are numerous other theories which can be expressed in terms of the modifier operator $\mathcal{L}_{\text{MOD}}$ which result from this set of assumptions.

One can probably infer from even this short summary that the dynamics of cylindrical shells is more contentious a topic than the dynamics of plates even without the presence of in-homogeneity. However, the goal of this work is to study waves in thin cylindrical shells with modestly varying thickness. Also, the correlation length of the random thickness fields to be considered will be much longer than the wavelengths of interest. This places the current problem in the geometric optics limit and allows us to study it using the ray dynamics formulation. We shall study this problem using ray equations due to Pierce [3] and also using ray equations derived from the equations of motion due to Yu [131].

Waves in elastic shells have attracted the attention of dynamicists for sometime [132, 133]. Pioneering work on the statics of cylindrical shells was carried out by Donnell [62]. This has been extended, for example by Yu [131, 134], Naghdi & Cooper [135], to derive the dynamic equations of motion. Numerous formulations of the dynamics of shells, of varying degrees of accuracy, exist; these have been summarised by Greenspon [133] and Leissa [63]. Propagating waves [3, 136, 137], normal modes [131, 134] and shells under random excitation [138] have been studied theoretically, computationally [139] and experimentally [140]. See [141–143] for recent developments in the dynamics of cylindrical shells. The propagation behaviour of plane waves in the presence of inevitable manufacturing tolerances has, however, not been studied in any detail so far. Here we examine the the effect of such spatial non-homogeneities and explore the emergence of channels of energy flow in such elastic waveguides.

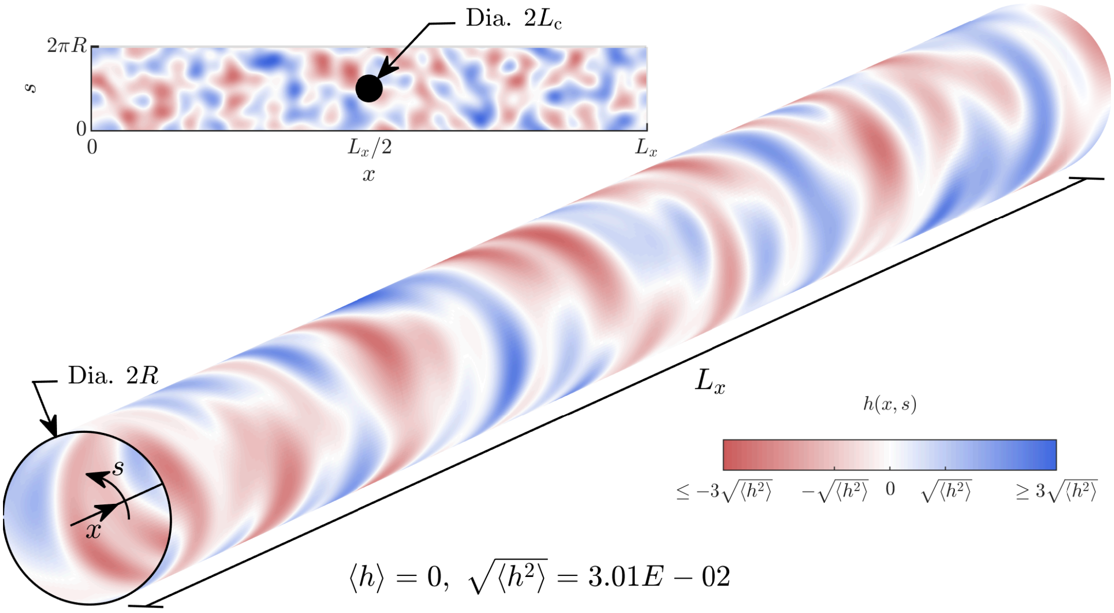
Dia. $2L_c$
$2\pi R$
s
0
0
$L_x/2$
L_x
x
Dia. $2R$
s
x
L_x
$h(x,s)$
$\leq -3\sqrt{\langle h^2\rangle}$
$-\sqrt{\langle h^2\rangle}$
0
$\sqrt{\langle h^2\rangle}$
$\geq 3\sqrt{\langle h^2\rangle}$
$\langle h\rangle = 0,\ \sqrt{\langle h^2\rangle} = 3.01E-02$

FIGURE 3.1: Spatial variation of thickness over the surface of an exemplar cylindrical waveguide. The radius of the cylindrical shell is R, axial length L_x, thickness H that varies spatially as per $H(x,s) = H_0(1 - h(x,s))$, where $\langle h\rangle = 0$, $\langle h^2\rangle \ll 1$. Colormap shows the spatial variation of $h(x,s)$. Inset on the top left is an "unwrapped" view of $h(x,s)$. In the middle of the inset, a circle of radius L_c, equal to the correlation length, is shown.

Consider the propagation of flexural waves through a hollow cylindrical waveguide when the wavelength of interest is much shorter than the correlation length of the heterogeneity of properties such as thickness or material stiffness. The tubular cross-section suffers breathing displacement that is radial, as the pattern propagates axially as a wave. The nominal thickness of the elastic cylinder is much smaller than the wavelength of interest, which justifies ignoring shear through the thickness in our analyses. Consider a cylinder of non-uniform thickness with the axis along the x-direction; the circumferential direction along s (with units of length) and thickness $H(x,s)$ about the nominal cylindrical surface. The thickness of the hollow elastic cylinder has the form $H(x,s) = H_0(1 - h(x,s))$ where $h(x,s)$ is a smoothly varying random field with an isotropic auto-correlation function; the correlation length is L_c, and $\langle h\rangle = 0$, $\langle h^2\rangle \ll 1$ (see Figure 3.1).

In this chapter, we will follow a procedure similar to that used in the previous one to study branched flows in thin cylindrical shells from analysis and using numerical methods. We will first develop a ray dynamics description of the problem at hand. Then we will study the scaling of the expected location of the first caustic from further analysis of the ray equation and also their numerical integration. To check if our results are robust, we obtain the scaling from analysis and validate against numerical integration of two different formulations: the ray dynamics of flexural waves in thin cylindrical shells—ray equations due to Pierce [3] and ray equation derived directly from equations of motions due to Yu [131]. Finally, we demonstrate branched flow and validate the associated scaling from a full finite element wave elastodynamics transient simulations of the spatio-temporal evolution of an initially plane radial pulse excitation on a thin hollow cylinder of modest non-uniform thickness.

3.2 Ray equations for radial displacement in thin cylindrical shells

Consider an initially plane wavefront of predominantly one wavelength propagating axially through a thin cylindrical shell. The assumption of slow spatial variation of properties enables the simplification of the wave elastodynamics to a set of ray equations using the eikonal/WKB approximations [144, 145]. We consider the system of ray equations by Pierce [3], which is a simple formulation based on Yu's equations of motion [131]. The ray equations are also derived independently in this work from Yu's equations of motions. These ray equations are more accurate, as evidenced by the fact that it captures the appearance of complete back-scattering at higher $\langle h^2 \rangle$ (to be discussed later), unlike the results from ray equations due to Pierce.

The ray dynamics can be further simplified using the paraxial approximation [146], permitted by the weak scattering nature of the problem, which asserts a predominantly axial direction of the wave vector. After applying the paraxial approximations the two ray systems behave very similarly, even at higher $\langle h^2 \rangle$. These ray equations are then used for further analysis and also integrated numerically to investigate the scaling of the location of the first caustic with statistical properties of the random field.

3.2.1 Ray equations from Pierce's formulation

Ray equations for theories of thin shells (Pierce)

The propagation of a strongly monochromatic wavefront (i.e. with one predominant wavenumber, say k_0) can be approximated by the equivalent ray dynamics as long as the wavelength is much shorter than 'feature size' (in this study, $\mathcal{O}(L_c)$). Rays are fully described by four quantities: spatial variables x, s indicating the location of the ray along the axis and circumference respectively, and k_x, k_s, the corresponding wavenumber components in the axial and circumferential directions respectively. The spatial variables are non-dimensionalised with respect to the nominal radius, i.e. $\tilde{x} = x/R, \tilde{s} = s/R$, whereas the wavenumbers are non-dimensionalised with respect to the initial wavenumber $\tilde{k}_x = k_x/k_0$, $\tilde{k}_s = k_s/k_0$. Note that this nondimensionalisation procedure is different from the one used in the previous chapter. Given the parameter regime of interest, (thin shell, small curvature, and slowly varying parameters) we can use the dispersion relation given by Pierce [3] to obtain the non-dimensionalised ray equations

$$
\begin{aligned}
\partial_\tau \tilde{x} &= \tilde{k}_x \left(\tilde{k}_x^2 + \tilde{k}_s^2 + 12(1-\nu^2)\frac{\gamma^2}{\epsilon^2} \frac{\tilde{k}_x^2 \tilde{k}_s^2}{\left(\tilde{k}_s^{\,2} + \tilde{k}_x^{\,2}\right)^3} \right), \\
\partial_\tau \tilde{s} &= \tilde{k}_s \left(\tilde{k}_x^2 + \tilde{k}_s^2 - 12(1-\nu^2)\frac{\gamma^2}{\epsilon^2} \frac{\tilde{k}_x^4}{\left(\tilde{k}_s^{\,2} + \tilde{k}_x^{\,2}\right)^3} \right), \\
\begin{bmatrix} \partial_\tau \tilde{k}_x \\ \partial_\tau \tilde{k}_s \end{bmatrix} &= \frac{1}{2}(\tilde{k}_x^2 + \tilde{k}_s^2)^2 \tilde{\nabla} \tilde{h},
\end{aligned}
\tag{3.7}
$$

where $\gamma = (k_0 R)^{-1}$, $\epsilon = H_0 k_0$. Additionally, $\tilde{h}(x/R, s/R) = h(x, s)$ and $\tilde{\nabla} = [\partial_{\tilde{x}}\ \partial_{\tilde{s}}]^T$. Here, τ is an arbitrary time scale, consistent with ray approximations. The initial condition is $\tilde{x} = 0$, $\tilde{k}_x = 1$, $\tilde{k}_s = 0$ and $\tilde{s} \in [0, 2\pi)$ depending on circumferential location of the ray's starting point. This simplified formulation assumes that $\lambda/R \ll 1$ [3, 136] and is based on the equations of motion by Yu [131] and Pierce's own derivation [147].

Paraxial ray equations (Pierce)

In the regime of weak scattering, as studied here, the ray equations corresponding to thin elastic shells can be simplified. The wavenumbers in the axial and circumferential directions ($\tilde{k}_x$ and $\tilde{k}_s$ respectively), are not expected to vary substantially from their initial values of 1 and 0 respectively, because the initially launched plane wave is purely axial. For weak scattering of initially plane waves, it is common to make the simplifying assumption that the wave-number does not change at all in the main propagation direction. This can be achieved by setting $\partial_\tau \tilde{k}_x = 0$, $\tilde{k}_x = 1$ in Equation 3.7, which is the essence of the paraxial approximation. Finally, dropping all

$\tilde{k}_s$ terms compared to $\mathcal{O}(1)$ terms, the ray equations become

$$\partial_\tau \tilde{x} = 1, \quad \partial_\tau \tilde{s} = \tilde{k}_s \left(1 + 12(\nu^2 - 1)\frac{\gamma^2}{\epsilon^2}\right), \quad \partial_\tau \tilde{k}_x = 0, \quad \partial_\tau \tilde{k}_s = \frac{1}{2}\partial_{\tilde{s}} \tilde{h}. \qquad (3.8)$$

The approximations made to obtain Equation 3.8 from the Equation 3.7 use arguments about the physics of the problem. Nonetheless, the validity of these assumptions is further confirmed here by numerical integration of ray equations (details of numerical ray integration later in section 3.6).

Results of the ray simulations are presented next. Figure 3.2 (left) shows the comparison between the rays obtained from numerical integration of the full thin shell ray equations (Equation 3.7), and the simplified ray equations obtained following the paraxial approximation (Equation 3.8) for increasing values of $\langle h^2 \rangle$. The rays have been plotted "unwrapped" in the left column of the figure, where 300 rays equi-spaced along the circumference at the left end are launched as they curve and veer downstream due to scattering. Transmission behaviour on the cylindrical surface, is shown in Figure 3.2 (column at the centre) where interesting spiral structures with no preferred handedness, as expected, are observed. The rays as computed using the thin shell theory versus that using the paraxial approximation look fairly similar, confirming the validity of the paraxial approximation. It can be seen that, at the time instant at which the simulation is terminated, all rays have reached the right edge in case of the paraxial approximation, unlike the rays obtained from integrating the thin shell ray equations. This is a consequence of the paraxial assumption i.e. the assumption that all rays travel with a constant speed in the main propagation direction. Most importantly, it can be seen that the spatial location of the first caustic, indicated by circular and cross-shaped markers, is approximately the same from both sets of ray equations, except for the highest levels of $\langle h^2 \rangle$ shown here.

In Figure 3.2 (right), the time evolution of the four quantities describing one exemplar ray is plotted. We can see that the values of $\tilde{x}$, $\tilde{s}$, $\tilde{k}_s$ are in excellent agreement. Also, $\tilde{k}_x$ has a constant value in the paraxial approximation as stated earlier. While it does not, obviously, show the variation with time that thin shell case shows, note that the values do not change appreciably from 1. Regardless, the first caustic is detected by looking for the instant where the $\tilde{s} - \tilde{k}_s$ curve becomes locally two valued (see section 3.4) and is not dependent on $\tilde{k}_x$ directly. In Figure 3.2 (right), markers indicate temporal location of the first caustic.

The paraxial approximation becomes more inaccurate as time passes. However, since we are interested only in the location of first caustic, and they tend to appear fairly early, this eventual drift is inconsequential. The paraxial approximation also breaks down faster when the value of $\langle h^2 \rangle$ is higher, i.e. when the weak scattering assumption starts breaking down. However, this is partially counteracted by the fact that when the value of $\langle h^2 \rangle$ is higher, the first caustic appear earlier. Nonetheless, the

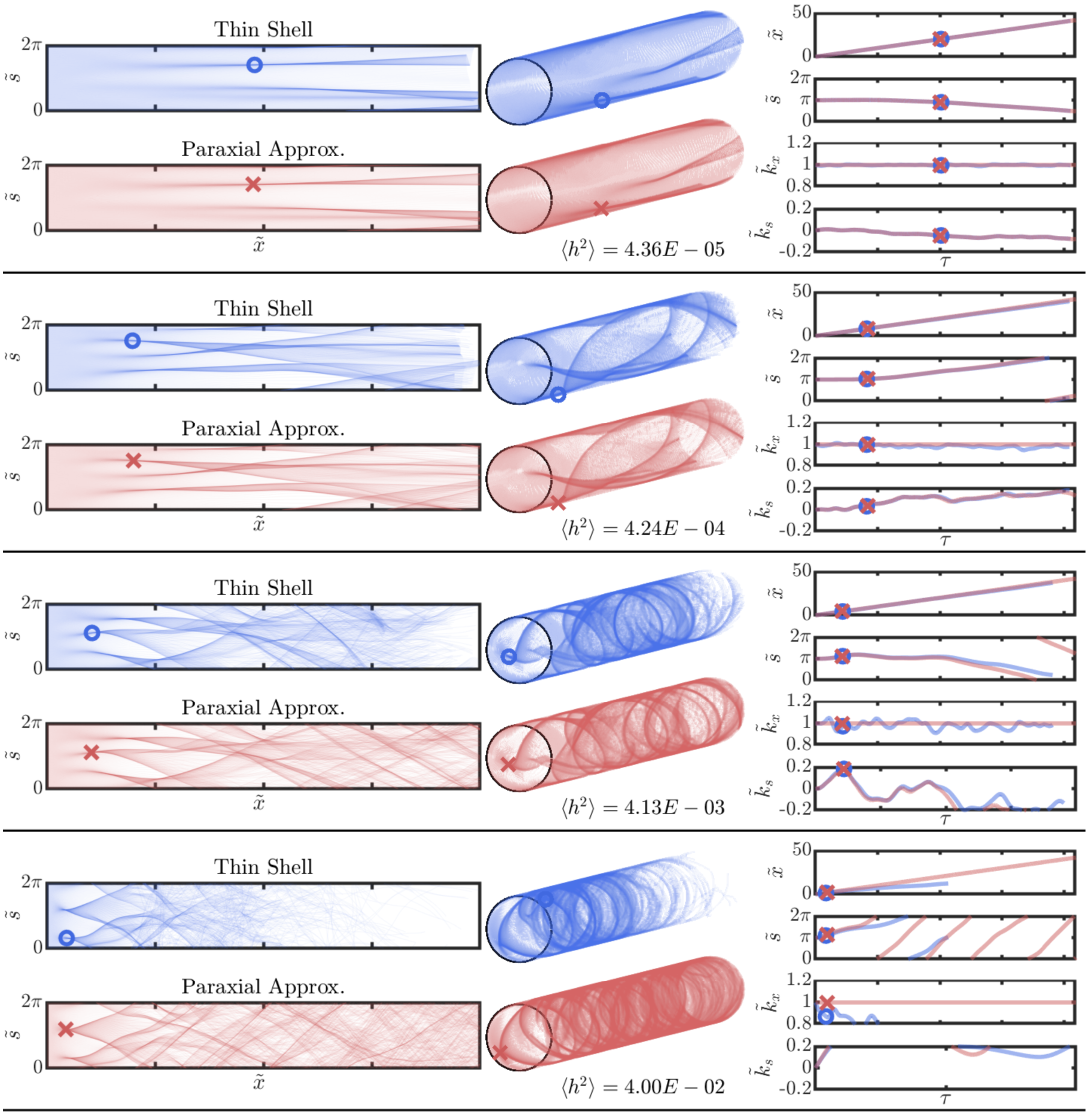

FIGURE 3.2: Comparison of thin shell ray equations and equations obtained from making the paraxial approximation for ray equations due to Pierce [3]. Left: Ray propagation using full thin shell theory and paraxial approximation of thin shell theory. Circular and cross markers indicate location of the first caustic. The $\tilde{s}$ axis has been "unwrapped" for representational purposes. Middle: Same ray propagation shown on the cylindrical surface. Right: Plot of the temporal evolution of quantities describing one of the rays. Here, markers indicate *temporal* location of the first caustic. It can be seen that, at higher values of $\langle h^2 \rangle$, the location of the first caustic detected from the paraxial approximation differs from thin shell.

progressive degradation of the paraxial approximation with increase in $\langle h^2 \rangle$ can be seen in Figure 3.2.

We will later use these ray equations to derive the scaling of $\langle l_f \rangle$ analytically. We will also numerically integrate them to study the scaling. The ray equations Equation 3.7 (and, therefore, Equation 3.8 too) are obtained from the simplified dispersion relation for flexural waves in a thin shell. At the higher $\langle h^2 \rangle$, some rays are expected to completely back-scatter due to the severity of randomness. This is not captured by Equation 3.7. In the next subsection, we derive the ray equations starting from the governing equations of the displacements of a thin cylindrical shell [131]. These ray equations are more sophisticated and show the expected back scattering at higher values of $\langle h^2 \rangle$. However, after applying the paraxial approximation, the resultant set of ray equations show very similar results to *Equation* 3.8.

3.2.2 Ray equations from equations of motion due to Yu

The equation of motion for the radial displacement of a cylindrical shell, $\eta(x, s, t)$, is given by (Yu [131])

$$\begin{aligned} &\frac{H^2}{12}\nabla^8\eta + \frac{1-\nu^2}{R^2}\partial_{xxxx}\eta + \rho\frac{2(1+\nu)}{E}\partial_{tt}\left[\left(\rho\frac{1-\nu^2}{E}\partial_{tt} - \frac{3-\nu}{2}\nabla^2\right)\right. \\ &\left.\times\left(\rho\frac{1-\nu^2}{E}\partial_{tt}\eta + \frac{\eta}{R^2} + \frac{H^2}{12}\nabla^4\eta\right) + \frac{1-\nu}{2}\nabla^4\eta + \frac{\nu^2}{R^2}\partial_{xx}\eta + \frac{1}{R^2}\partial_{ss}\eta\right] = 0, \end{aligned} \tag{3.9}$$

where $\nabla^2 = \partial_{xx} + \partial_{ss}$. The material parameters, $\nu,\ E$ and ρ – Poisson's ratio, Young's Modulus and density respectively, are constant throughout.

This formalism ignores contributions to strain energy due to through thickness shear deformation and rotary inertia. It also ignores geometric non-linearity in the strain-displacement relationships. The time independent terms in the resulting shell dynamics equations above are the same as Donnell's equations [62] for statics.

Note that the system of equations given by Yu have expressions for the time evolution of the displacement in the circumferential and axial directions too. Equation 3.9 describes the time evolution of the radial displacement that is independent of the displacements in the other two directions. If we were interested in the displacements in the other two directions, they could be obtained in conjunction with the solution of Equation 3.9.

Eikonal equation and dispersion relations (Yu)

We assume that $\lambda \ll L_c$. This means that $H(x,s)$ has properties that are spatially "slowly varying" which allows us to derive the eikonal equation from Equation 3.9. This is done by setting $\eta(x,s,t) = \hat{\eta}(x,s)e^{-i\omega t + iS(x,s)}$, where $S(x,s)$ is the eikonal. All derivatives of H and all derivatives of S higher than the first order are discarded due to the slowness of the spatial variation of the properties. The eikonal equation thus obtained is

$$\begin{aligned}
&\frac{H^2(\partial_x S)^8}{12} + \frac{1}{3}H^2(\partial_x S)^6(\partial_s S)^2 + \frac{H^2(\partial_x S)^6(\nu+1)(\nu-3)\rho\omega^2}{12E} \\
&+ \frac{1}{2}H^2(\partial_x S)^4(\partial_s S)^4 + \frac{H^2(\partial_x S)^4(\partial_s S)^2(\nu+1)(\nu-3)\rho\omega^2}{4E} \\
&- \frac{(\partial_x S)^4\left(\nu^2-1\right)\left(H^2(\nu+1)\rho^2R^2\omega^4 - 6\rho R^2\omega^2 E + 6E^2\right)}{6R^2E^2} \\
&+ \frac{1}{3}H^2(\partial_x S)^2(\partial_s S)^6 + \frac{H^2(\partial_x S)^2(\partial_s S)^4(\nu+1)(\nu-3)\rho\omega^2}{4E} \\
&- \frac{(\partial_x S)^2(\partial_s S)^2\left(\nu^2-1\right)\rho\omega^2\left(H^2(\nu+1)\rho\omega^2 - 6E\right)}{3E^2} \\
&+ \frac{H^2(\partial_s S)^8}{12} + \frac{H^2(\partial_s S)^6(\nu+1)(\nu-3)\rho\omega^2}{12E} \\
&- \frac{(\partial_s S)^4\left(\nu^2-1\right)\rho\omega^2\left(H^2(\nu+1)\rho\omega^2 - 6E\right)}{6E^2} \\
&+ \frac{(\partial_x S)^2\left(\nu^2-1\right)\rho\omega^2\left((\nu+1)(\nu-3)\rho R^2\omega^2 + (2\nu+3)E\right)}{R^2E^2} \\
&+ \frac{(\partial_s S)^2\left(\nu^2-1\right)\rho\omega^2\left((\nu+1)(\nu-3)\rho R^2\omega^2 + E\right)}{R^2E^2} \\
&- \frac{2(\nu+1)\left(\nu^2-1\right)\rho^2\omega^4\left(\left(\nu^2-1\right)\rho R^2\omega^2 + E\right)}{R^2E^3} = 0.
\end{aligned} \tag{3.10}$$

By setting $\partial_s S = 0$, $\partial_x S = k_x$, $H = H_0$, one gets the dispersion relation for flexural wave transmission along the axial direction in a uniform cylinder,

$$\begin{aligned}
&\frac{k_x^4\left(H_0^2k_x^4R^2 - 12\nu^2 + 12\right)}{12R^2} \\
&+ \frac{k_x^2(\nu+1)\rho\left(H_0^2k_x^4(\nu-3)R^2 + 12k_x^2(\nu-1)R^2 + 12(\nu-1)(2\nu+3)\right)}{12R^2E}\omega^2 \\
&- \frac{(\nu-1)(\nu+1)^2\rho^2\left(H_0^2k_x^4R^2 - 6k_x^2(\nu-3)R^2 + 12\right)}{6R^2E^2}\omega^4 \\
&- \frac{2(\nu-1)^2(\nu+1)^3\rho^3}{E^3}\omega^6 = 0,
\end{aligned} \tag{3.11}$$

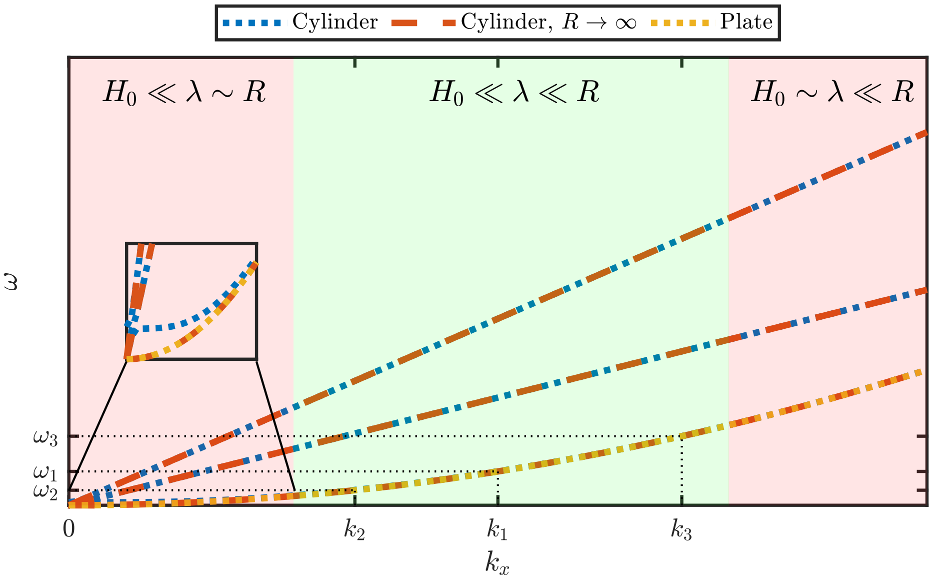

FIGURE 3.3: Comparison of dispersion relations. Dispersion relations obtained from equation of motion of a cylindrical shell are plotted with blue dotted lines; the same dispersion relation at the $R \to \infty$ limit is shown with orange dotted lines; the dispersion relation obtained from the equation of motion of a flat plate is plotted with a yellow dotted line. It can be seen that, in the parameter regime of interest ($H_0 \ll \lambda \ll R$), the lowest branch of the dispersion relations from equation of motion a cylinder is approximated well by the dispersion relation obtained from equation of a flat plate.

where k_x is the axial wavenumber. Further, setting $R \to \infty$ would yield the dispersion relation for a flat plate.

$$\begin{aligned}\frac{H_0^2 k_x^8}{12} &+ \frac{k_x^4(\nu+1)\rho\left(H_0^2k_x^2(\nu-3)+12(\nu-1)\right)}{12E}\omega^2 \\ &- \frac{k_x^2(\nu-1)(\nu+1)^2\rho^2\left(H_0^2k_x^2-6\nu+18\right)}{6E^2}\omega^4 - \frac{2(\nu-1)^2(\nu+1)^3\rho^3}{E^3}\omega^6 = 0.\end{aligned} \tag{3.12}$$

This can be compared with the dispersion relation for a flat plate [104],

$$\omega^2 = \frac{EH_0^2k_x^4}{12\rho(1-\nu^2)}. \tag{3.13}$$

We anticipate that all three dispersion relations will behave similarly in the regime of our interest ($H_0 \ll \lambda \ll R$). This can be seen from Figure 3.3 where the three dispersion relations have been plotted for typical material and geometric parameters used in the current study. We can see that in the parameter regime of interest, the lowest branch of the dispersion relations obtained from the equation of motion for a cylinder have similar values as those of the dispersion relation obtained from the equations of motion of a plate.

For the numerical study, we excite the elastic tubes by imposed displacements of a certain dominant frequency, shown in Figure 3.3 as $\omega_1, \omega_2, \omega_3$. The dispersion relations obtained from the equations of motions of a cylinder yield more branches as compared to the one from equations of a plate. This is because of the higher order of the governing equation and the other branches correspond to membrane-type displacements. However, it is seen from numerical simulations (FE) that the higher branches are not appreciably excited. This is because the excitation is predominantly radial and in the form of a circumferential line source. This only excites the lowest "breathing mode". Hence, we can restrict ourselves to the lowest branch of the dispersion relation. As noted earlier this lowest branch can be satisfactorily approximated by the dispersion relation obtained from equations of a plate in the parameter regimes of interest. Given the formal simplicity of the dispersion relation obtained from plate equations we shall use them later, to write down k_x explicitly in terms of ω in the derivation of non-dimensionalised ray equations.

The red region on the left in Figure 3.3 corresponds to small wave-numbers or, alternatively, large wavelengths. When the wavelengths become comparable to the radius of the cylinder i.e. $\lambda \sim R$, the curvature plays an increasingly important role in the dynamics of wave propagation. This explains why the dispersion relations for a cylinder (with finite R) and dispersion relations in the $R \to \infty$ limit begin to diverge from each other in this region (see Figure 3.3, inset). Meanwhile, the red region on the right-hand side of Figure 3.3 corresponds large wave-numbers or, alternatively small wavelengths (similar order as H_0). This is a regime ($H_0 \sim \lambda$) in which the suitability of the *thin* plate and shell equations we used to derive the dispersion relations is itself questionable.

Ray equations based on thin shell theory (Yu)

By setting $\nabla S = [k_x \; k_s]^T$, where k_x & k_s are wavenumbers in the axial and circumferential directions respectively and then using Cauchy's method of characteristics (see [104]), we obtain the ray equations

$$\begin{aligned}
\partial_\tau x &= \frac{k_x}{216R^2(1-\nu)}\Big[3H_0^4k_0^4(\nu-3)R^2\left(k_0^4-3\left(k_x^2+k_s^2\right)^2\right) \\
&\quad - 36H_0^2(\nu-1)\left(k_0^4\left(2\nu+2k_x^2R^2+2k_s^2R^2+3\right)-4R^2\left(k_x^2+k_s^2\right)^3\right) \\
&\quad - H_0^6k^8R^2\left(k_x^2+k_s^2\right)-864(\nu-1)^2(\nu+1)k_x^2\Big] \qquad (3.14) \\
\partial_\tau s &= \frac{H_0^2k_s}{216R^2(1-\nu)}\Big[H_0^2k_0^8R^2\left(H_0^2\left(k_x^2+k_s^2\right)-3\nu+9\right) \\
&\quad + 9k_0^4\Big(H_0^2(\nu-3)k_x^4R^2+2k_x^2R^2\left(H_0^2(\nu-3)k_s^2+4(\nu-1)\right) \\
&\quad + H_0^2(\nu-3)k_s^4R^2+4(\nu-1)+8(\nu-1)k_s^2R^2\Big) \\
&\quad - 144(\nu-1)R^2\left(k_x^2+k_s^2\right)^3\Big] \\
\begin{bmatrix}\partial_\tau k_x \\ \partial_\tau k_s\end{bmatrix} &= \frac{\nabla h}{432(1-\nu)}\Big[H_0^2\left(k_x^2+k_s^2\right)^2\left(H_0^2k_0^4-12\left(k_x^2+k_s^2\right)\right) \\
&\quad \times\left(H_0^2k_0^4+6(\nu-1)\left(k_x^2+k_s^2\right)\right)\Big].
\end{aligned}$$

Here, k_0 is the wavenumber excited in the structure on excitation at frequency ω. Notice that the eikonal equation is only unique up to a multiplicative constant. Hence the scaling of the time variable τ is arbitrary, as is the case with ray approximations.

For the purpose of our discussions it would be useful to define two non-dimensional parameters which strongly influence the transmission of flexural waves in thin cylinder: (1) $\gamma = \frac{1}{k_0R}$ and (2) $\epsilon = H_0k_0$.

We will now non-dimensionalise the ray equations, as earlier, by setting $\tilde{x} = x/R$, $\tilde{s} = s/R$, $\tilde{k}_x = k_x/k_0$, $\tilde{k}_s = k_s/k_0$. We shall also replace τ with $\left(\frac{R}{k_0^7H_0}\right)\tau$ as we can scale time arbitrarily. This scaling simplifies the non-dimensionalised ray equations. It also ensures that the time derivative terms are roughly $\mathcal{O}(1)$. This helps avoid any possible machine precision/overflow based issues when the ray equations are integrated numerically. The numerical integration worked fine without this scaling also. Machine precision/overflow issues might be rare for the system under consideration. However, we choose this scaling as a matter of good numerical computing practice. Apart from the two stated above, there are no other reasons to choose this specific scaling for τ. We shall use the expression $\omega = \sqrt{\frac{EH_0^2k_0^4}{12\rho(1-\nu^2)}}$ from dispersion relations of a flat plate. Ideally, we should obtain an expression for k_0 in terms of ω by solving the dispersion relation we obtained earlier for wave propagation in cylinders. While it may be possible to write it in closed form, it is expected to be algebraically complicated. Given that, we had earlier established, using observations from Figure 3.3, that the dispersion relation for a flat plat approximates the dispersion relation of a cylinder of the geometric and material parameters of interest,

$$
\begin{aligned}
\partial_\tau \tilde{x} =& \frac{-\tilde{k}_x}{216(\nu-1)\epsilon^2}\Bigg[\tilde{k}_x^2\Bigg(18(\nu-3)\epsilon^4\tilde{k}_s^2 - 432(\nu-1)\epsilon^2\tilde{k}_s^4 \\
&+ 864\gamma^2(\nu-1)^2(\nu+1) + \epsilon^6 + 72(\nu-1)\epsilon^2\Bigg) - 144(\nu-1)\epsilon^2\tilde{k}_x^6 \\
&+ 9\tilde{k}_x^4\left((\nu-3)\epsilon^4 - 48(\nu-1)\epsilon^2\tilde{k}_s^2\right) \\
&+ \epsilon^2\Bigg(-144(\nu-1)\tilde{k}_s^6 + \tilde{k}_s^2\left(72(\nu-1)+\epsilon^4\right) + 9(\nu-3)\epsilon^2\tilde{k}_s^4 \\
&+ 36\gamma^2(\nu-1)(2\nu+3) - 3(\nu-3)\epsilon^2\Bigg)\Bigg], \\
\partial_\tau \tilde{s} =& \frac{-\tilde{k}_s}{216(\nu-1)}\Bigg[-144(\nu-1)\tilde{k}_x^6 + 9\tilde{k}_x^4\left((\nu-3)\epsilon^2 - 48(\nu-1)\tilde{k}_s^2\right) \\
&+ \tilde{k}_x^2\left(-432(\nu-1)\tilde{k}_s^4 + 18(\nu-3)\epsilon^2\tilde{k}_s^2 + 72\nu + \epsilon^4 - 72\right) \\
&- 144(\nu-1)\tilde{k}_s^6 + \tilde{k}_s^2\left(72\nu+\epsilon^4-72\right) + 9(\nu-3)\epsilon^2\tilde{k}_s^4 \\
&+ 36\gamma^2\nu - 36\gamma^2 - 3\nu\epsilon^2 + 9\epsilon^2\Bigg], \\
\begin{bmatrix}\partial_\tau\tilde{k}_x \\ \partial_\tau\tilde{k}_s\end{bmatrix} =& \frac{-\tilde{\nabla}\tilde{h}}{432(1-\nu)}\left(\tilde{k}_x^2+\tilde{k}_s^2\right)^2\left(12(\tilde{k}_x^2+\tilde{k}_s^2)-\epsilon^2\right)\left(6(\nu-1)(\tilde{k}_x^2+\tilde{k}_s^2)+\epsilon^2\right),
\end{aligned}
\tag{3.15}
$$

where $\tilde{\nabla} = [\partial_{\tilde{x}}\ \partial_{\tilde{s}}]^T$.

The ray equations derived from the equations of motion of transverse displacement of a cylindrical shells are rather complicated and not particularly amenable to further analysis. However, in the regime of weak scattering that we study here, the ray equations can be simplified greatly. The wavenumbers in the x and s directions, $\tilde{k}_x$ and $\tilde{k}_s$, are not expected to vary substantially from their initial values of 1 and 0 respectively, as the initially launched flexural wave is in the purely axial direction.

Paraxial ray equations (Yu)

For weak scattering of initially plane waves, it is customary to make the simplifying assumption that the wave-number does not change at all in the main propagation direction. This can be achieved by setting $\partial_\tau\tilde{k}_x = 0$, $\tilde{k}_x = 1$ in Equation 3.15, which is the essence of the paraxial approximation. Finally, dropping all $\tilde{k}_s$ terms compared to $\mathcal{O}(1)$ terms, the ray equations become

$$
\partial_\tau\tilde{x} = c_1, \qquad \partial_\tau\tilde{s} = c_2\tilde{k}_s, \qquad \partial_\tau\tilde{k}_x = 0, \qquad \partial_\tau\tilde{k}_s = c_3\tilde{h}_{\tilde{s}}, \tag{3.16}
$$

where,

$$\begin{aligned}
c_1 &= \gamma^2(-\nu/3 + (1-\nu^2)4/\epsilon^2 - 1/2) + \zeta,\\
c_2 &= -\gamma^2/6 + \zeta,\\
c_3 &= \zeta/2,\\
\zeta &= -\frac{\left(\epsilon^2-12\right)\left(6\nu+\epsilon^2-6\right)}{216(\nu-1)}.
\end{aligned}$$

Figure 3.4 shows the comparison of ray equations from thin shell theory and the one obtained after applying the paraxial approximation. The figure is similar to Figure 3.2. However, here we can see that the ray equations based on thin shell theory are able to model even complete back scattering at higher values of $\langle h^2 \rangle$ unlike the formulations of ray equations used in the main text. Nonetheless, it can be seen that after the application of the paraxial approximation (which negates any back-scattering behaviour), the rays look identical to the one in the main text even at higher $\langle h^2 \rangle$.

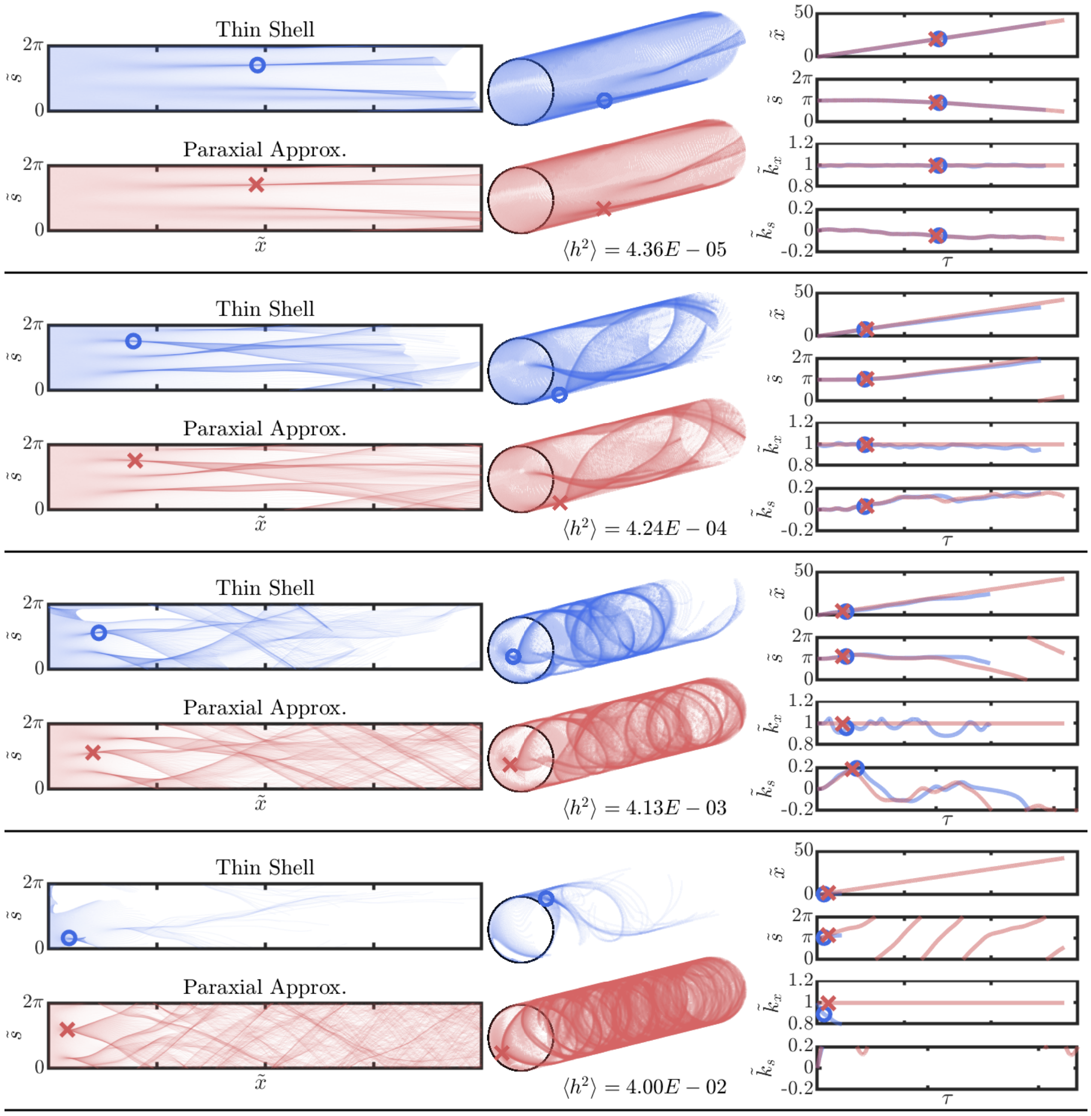

FIGURE 3.4: Comparison of thin shell ray equations and equations obtained from making the paraxial approximation using Yu's formulation. Left: Ray propagation using full thin shell theory and paraxial approximation of thin shell theory. Circular and cross markers indicate location of the first caustic. The $\tilde{s}$ axis has been "unwrapped" for representational purposes. Middle: Same ray propagation shown on the cylindrical shell. Right: Plot of the temporal evolution of quantities describing the one of the rays. Here, markers indicate *temporal* location of the first caustic. It can be seen that, at higher values of $\langle h^2 \rangle$, complete back-scattering of rays is observed in the thin shell case. This not modelled by the paraxial approximation which assumes weak scattering.

3.3 Scaling law from the analysis of ray equations

The steps we follow to derive the scaling law from the ray equations are similar to those in existing literature on branched flow. While formally similar, the specific terms are different. To derive the scaling law, the paraxial ray equations describing $\tilde{s}$ and $\tilde{k}_s$ are rewritten as a set of stochastic differential equations (SDEs). The random field is replaced with uncorrelated noise terms and a pre-factor which encodes the statistics of the random field. This results in a Langevin equation [148], which contains deterministic and stochastic terms described by the so-called drift and diffusion coefficient of the system. Consider the paraxial ray equations obtained from Yu's formulations of the the equations of motion. Equation 3.16, when re-written as a system of SDEs has linear drift coefficients and constant diffusion coefficients and is therefore, a specific type of Langevin equations called an Ornstein-Uhlenbeck Process[1]. Then, the Fokker Planck equation (FPE) is obtained from these Langevin equations. It describes the time evolution of the probability distribution of each of the state variables. The FPE is then integrated to obtain explicit expressions for the time evolution of the variance of the state variables as ODEs. Then a substitution is made, based on physical arguments, which yields the scaling law after rearrangement.

Equation 3.16, rewritten as a stochastic differential equation is,

$$\partial_\tau \tilde{s} - c_2 \tilde{k}_s = 0, \qquad \partial_\tau \tilde{k}_s = c_3 h_1 \Gamma(\tau), \tag{3.17}$$

where $h_1 = \sqrt{\pi}\langle h^2 \rangle / (c_1 \tilde{L_c})$ and $\Gamma(t)$ is a Gaussian white noise term with zero mean and $\langle \Gamma(\tau)\Gamma(\tau') \rangle = \delta(\tau - \tau')$. The factor h_1 encodes the properties of the random field when the ray equations (ODEs) are converted to SDEs and is found by imposing a conservation constraint on the correlation function (see [116] for details). The drift and diffusion coefficients of the SDE (Langevin equation) are

$$D_{\text{drift}} = \begin{bmatrix} 0 & -c_2 \\ 0 & 0 \end{bmatrix}, \qquad D_{\text{diffusion}} = \begin{bmatrix} 0 & 0 \\ 0 & c_3^2 h_1^2 \end{bmatrix}. \tag{3.18}$$

This yields the Fokker Planck equation [148] which describes the temporal evolution of the probability density of $\tilde{s}, \tilde{k}_s$,

$$\partial_\tau P(\tilde{s}, \tilde{k}_s, \tau) = \left(-c_2 \tilde{k}_s \partial_{\tilde{s}} + c_3^2 h_1^2 \partial_{\tilde{k}_s \tilde{k}_s} \right) P(\tilde{s}, \tilde{k}_s, \tau) \tag{3.19}$$

Note that $\iint (\bullet) P(\tilde{s}, \tilde{k}_s, \tau)\, \mathrm{d}\tilde{s}\, \mathrm{d}\tilde{k}_s = \langle \bullet \rangle$, i.e the expected value of $(\bullet)$ at some time τ. Hence, we can multiply Equation 3.19 by $\tilde{s}^2$, $\tilde{s}\tilde{k}_s$ and $\tilde{k}_s^2$ and integrate over the entire domain of $\tilde{s}$ and $\tilde{k}_s$ to obtain:

$$\begin{aligned} \partial_\tau \langle \tilde{s}^2 \rangle &= -2c_2 \langle \tilde{s}\tilde{k}_s \rangle \\ \partial_\tau \langle \tilde{s}\tilde{k}_s \rangle &= -c_2 \langle \tilde{k}_s^2 \rangle \\ \partial_\tau \langle \tilde{k}_s^2 \rangle &= 2c_3^2 h_1^2 \end{aligned} \tag{3.20}$$

---

[1] In the case of plates, discussed in the previous chapter, the resultant SDE is not an Ornstein-Uhlenbeck Process but a non-linear Langevin equation with 'multiplicative noise'. Nonetheless, the proof proceeds similarly (see [49]).

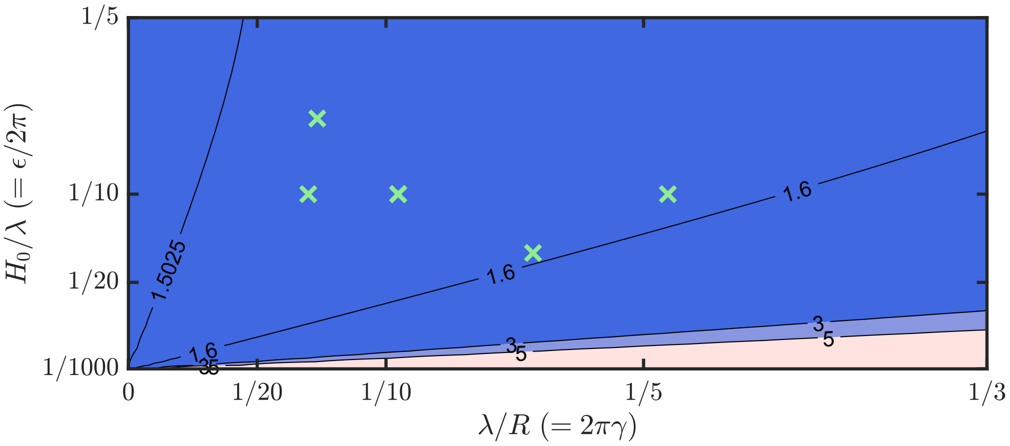

FIGURE 3.5: Plot of $\alpha^{\text{Yu}}(\gamma, \epsilon)$ (Equation 3.22). This plot shows that in the parameter region of interest, α has a weak dependence on γ & ϵ. Green cross markers indicate the parameters used in studies reported here.

These are coupled linear ODEs and can be solved with the initial conditions $\langle \tilde{s}^2 \rangle = \langle \tilde{s}\tilde{k}_s \rangle = \langle \tilde{k}_s^2 \rangle = 0$, at $\tau = 0$, since the wave is initially along x direction to obtain,

$$\langle \tilde{s}^2 \rangle = 2c_2^2 c_3^2 h_1^2 \frac{\tau^3}{3}. \tag{3.21}$$

Here we will make a physics based argument to arrive at the scaling of the location of the first caustic. A sketch of the arguments is given here (see [105]). For a focusing event to occur, two bundles of rays travelling in *opposite* directions (along $\tilde{s}$ direction) must interact. For these ray to have such different dynamics, they must be spread out by distances of the order of the correlation length. Hence, in Equation 3.21, setting $\langle \tilde{s}^2 \rangle \sim L_c^2$ and $\tau = \tilde{l}_f / c_1$ yields $\langle \tilde{l}_f \rangle \propto \alpha^{\text{Yu}}(\gamma, \epsilon) \tilde{L}_c \langle h^2 \rangle^{-1/3}$. Here

$$\begin{aligned}\alpha^{\text{Yu}}(\gamma, \epsilon) &= \left(\frac{3}{2\sqrt{\pi}} \frac{c_1^4}{c_2^2 c_3^2} \right)^{1/3} \\ &= \left(\frac{3}{2\sqrt{\pi}} \frac{\left(\gamma^2(-\nu/3 + (1-\nu^2)4/\epsilon^2 - 1/2) + \zeta\right)^4}{\left(-\gamma^2/6 + \zeta\right)^2 (\zeta/2)^2} \right)^{\frac{1}{3}}.\end{aligned} \tag{3.22}$$

α^{Yu} has an explicit dependence on γ & ϵ i.e. H_0, R & λ. However, it can be seen from Figure 3.5 that the dependence is actually quite weak in the parameter ranges of interest ($\alpha \approx 1.55 \pm 5\%$). Green cross markers indicate the cases that have been reported here.

Equation 3.16 and Equation 3.8 are formally identical and hence, the above analysis can be used to obtain the $\langle l_f \rangle$ scaling from the ray equations due to Pierce too. This

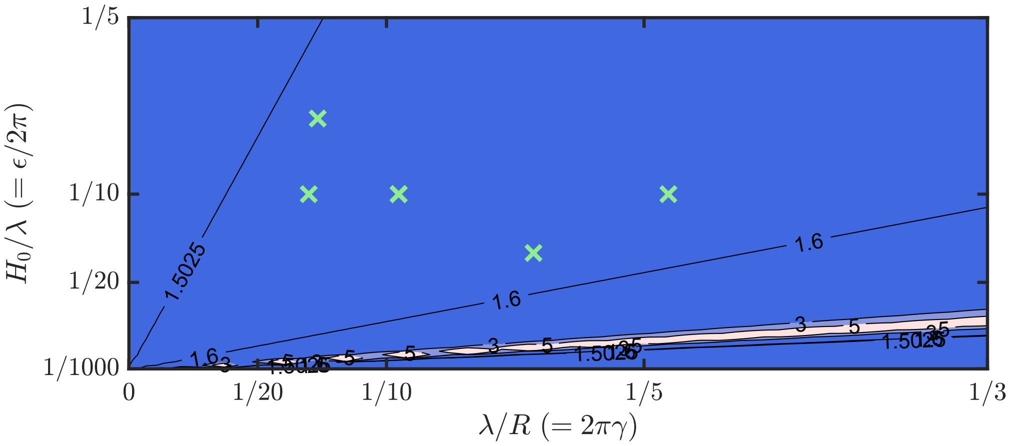

FIGURE 3.6: Plot of $\alpha^{\text{Pierce}}(\gamma, \epsilon)$. This plot shows that in the parameter region of interest, α has a weak dependence on γ & ϵ. Green cross markers indicate the parameters used in studies reported here.

yeilds $\langle l_f \rangle \propto \alpha^{\text{Pierce}}(\gamma, \epsilon) L_c \langle h^2 \rangle^{-1/3}$, where

$$\alpha^{\text{Pierce}}(\gamma, \epsilon) = \left(\frac{6}{\sqrt{\pi}} \right)^{1/3} \left(1 + 12(\nu^2 - 1) \frac{\gamma^2}{\epsilon^2} \right)^{-2/3}. \tag{3.23}$$

Like α^{Yu}, α^{Pierce} has an explicit dependence on γ and ϵ, i.e. H_0, R, and λ. However, it can be seen from Figure 3.6 that the dependence is weak in the parameter ranges of interest where $\alpha \approx 1.52 \pm 1\%$. Green cross markers indicate the cases that have been reported here.

The simpler form of α^{Pierce} makes it amenable to further analysis. The insensitivity of of the last term within the parentheses above relies on the wavelength of interest being much smaller than the radius of the hollow cylinder, more precisely on the relationship $\lambda \ll \sqrt{RH_0}$. Thus, the smallness of the nominal thickness H_0 must be compensated by the largeness of the radius R so that the product is sufficiently large compared to the wavelength. Largeness of H_0, on the other hand, invalidates thin shell theory that ignores thickness shear.

In the regime of $\lambda \ll \sqrt{RH_0}$, the relationship approximates to

$$\alpha \approx \left(\frac{6}{\sqrt{\pi}} \right)^{1/3} \left(1 + \frac{(1 - \nu^2)}{2\pi^4} \frac{\lambda^4}{R^2 H_0^2} \right). \tag{3.24}$$

Note that the value of the factor $2\pi^4$, in the denominator of the second term, is over two orders of magnitude, facilitating the smallness of the second terms, hence the insensitivity of α on γ/ϵ. While this dependence is not a simple power law, it still provides a simple expression that captures the role of the additional length scale, i.e. R, as compared to a flat plate waveguide. The above analysis also highlights the role of the ratio $\lambda/\sqrt{RH_0}$ in the dependence of the location of the first caustic upon this ratio. It seems that H_0/λ must be small enough for the thin shell theory to hold and yet large enough so as not to couple flexural and membrane modes.

In both Figure 3.5 and Figure 3.6, we can see that α is sensitive to γ and ϵ at higher values of γ and smaller values of ϵ. The first is associated with strong curvature effects —a case we are not interested in studying in this work. The latter is the small H_0/λ regime —increased energetic viability of membrane modes in this regime suggests that our analysis which focuses only on flexural modes may be insufficient here.

Since $\alpha^{\text{Yu}}(\gamma, \epsilon)$, $\alpha^{\text{Pierce}}(\gamma, \epsilon)$ are roughly constant in the parameter regimes of interest, we can conclude that the expected location of the first caustic does not scale with wavelength, nominal thickness or radius, if the thickness is small, and the radius is large, compared to the wavelength.

3.4 Scaling law from numerical integration of ray equations

The scaling Equation 2.14, in the case of cylindrical shells, can be studied by numerical integration of the ray equations derived above. The paraxial approximation based ray equations will be used. A similar procedure, as the one described in the previous chapter, is used for integration and detection of the first caustics with appropriate changes to ensure the circular continuity of the curve at $\tilde{s} = 0, 2\pi$ is respected.

Caustic detection is carried out numerically by tracking the local slope of the curve and detecting locations when the slope become higher than $\pi/2$. The temporal evolution of the $\tilde{k}_{\tilde{s}} - \tilde{s}$ curve is plotted in Figure 3.7. The first time this curve folds over itself, signalling the onset of a caustic, is shown in red. Note that since, $\tilde{k}_{\tilde{s}}$ has values centered around 0, a constant positive value is added to it for representational purposes. This value is not used when numerically detecting the caustic.

The scaling of the expected location of the first caustic $\langle l_f \rangle$ with 'severity' of randomness $\langle h^2 \rangle$ is studied next, akin to the study in chapter 2. Figure 3.8 (top - from ray formulation due to Pierce, and bottom - from ray equations derived from equations of motion due to Yu) shows that both of paraxial ray equations derived above display $\langle l_f \rangle$ scaling in excellent agreement with the theoretical predictions. Red dots indicate individual data points $\langle l_f \rangle$ where as, the expected location $\langle l_f \rangle$, the mean of each cluster is indicated by a blue square marker. Centered at the mean, are vertical lines indicating a width of two standard deviations.

Similarly, the expected linear scaling of $\langle l_f \rangle$ with correlation length is investigated. Values of $\langle l_f \rangle$ for $\tilde{L_c} = 0.7, 1.5$, obtained from numerical ray integration, are in excellent agreement with predictions made using a reference simulation with $\tilde{L_c} = 1$, assuming linear scaling with correlation length (see Figure 3.9).

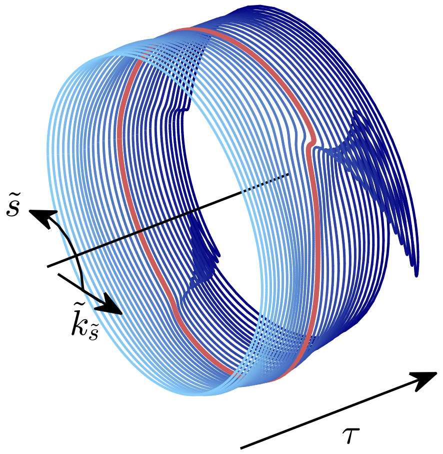

FIGURE 3.7: Plot of the temporal evolution of the $\tilde{k}_{\tilde{s}} - \tilde{s}$ curve obtained from numerical ray simulations. Since values of $\tilde{k}_{\tilde{s}}$ are centered around zero, a constant positive offset is added for the purpose of visualisation. The first caustic is detected by finding the location where the $\tilde{k}_{\tilde{s}} - \tilde{s}$ curve folds over itself (shown in red).

As predicted, the expected location of the first caustic is independent of the wavelength (see Figure 3.10). The values of $\langle l_f \rangle$ show no apprent change even when the wavelength is varied by $\sim$ 100%.

Finally, using ray simulations, $\langle l_f \rangle$ is shown to be insensitive to changes in the radius of the cylinder, in the $\lambda \ll R$ regime, see Figure 3.11. Some deviation from the predicted scaling is apparent in the smallest radius considered $R/R_0 = 0.5$. This signals the increased relevance of curvature effects. We are unable to study the regime of significant curvature effects (even smaller R) because of the bound imposed on the radius by the requirement the circumference to be of the order or larger than the correlation length.

Figure 3.12 shows the scaling of $\langle l_f \rangle$ with $\langle h^2 \rangle$ from all the sets of ray equations mentioned in this work. The set of ray equations from Yu's formulation (without the paraxial approximation) is the most accurate and is able to capture back scattering (see Figure 3.4), that is expected at higher $\langle h^2 \rangle$. This explains why thin shell equations from Yu's formulation show a larger departure from the predicted power law scaling at higher $\langle h^2 \rangle$. The same departure from the predicted power law does not appear in the other systems of ray equations considered here since they do not account for the possibility of back-scattering.

The location of the detected caustics from numerical ray integration must not show any angular bias in their location. We verify this as an additional check on out numerical simulations. Figure 3.13 show the angular distribution (light blue) of caustics detected using numerical ray integration. No consistent and appreciable bias is visible. Angular bias can be introduced inadvertently from improper interpolation of the randomness field when conducting numerical ray integration, as observed by

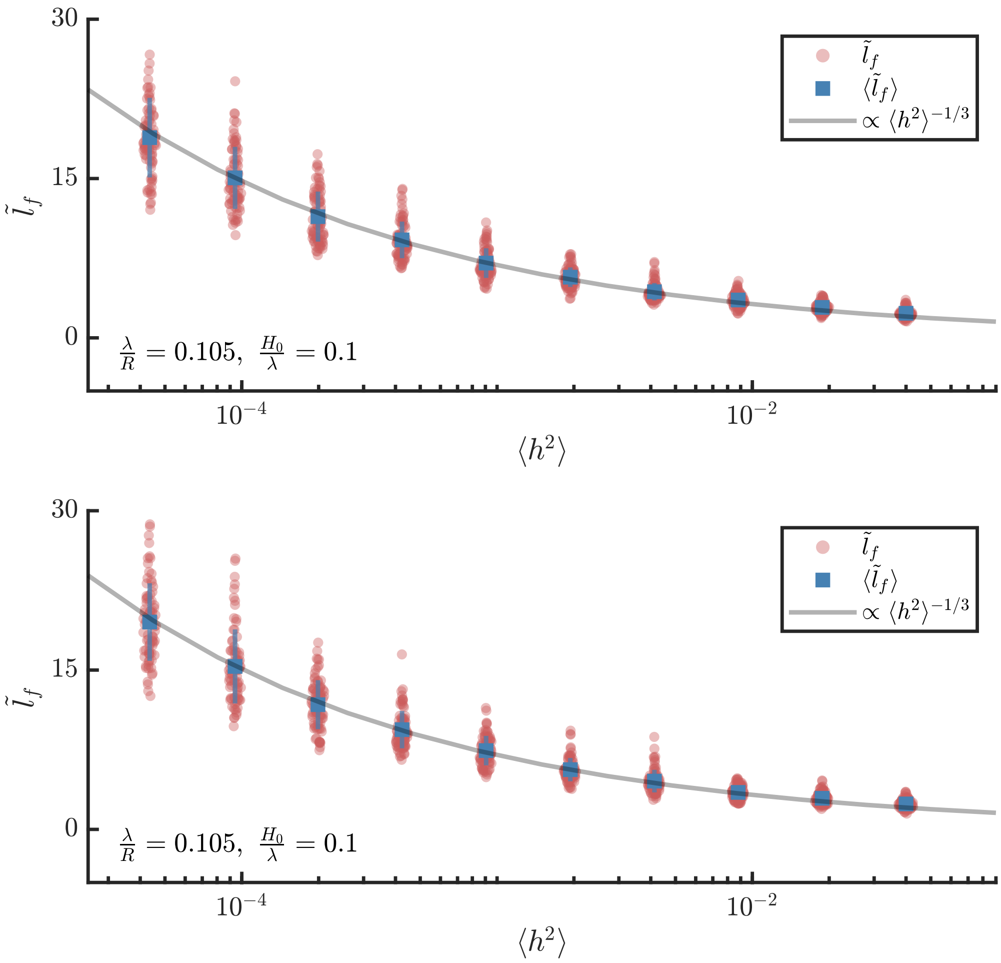

FIGURE 3.8: Scaling of location of first caustic with 'severity' of randomness (top - Pierce, bottom - Yu). Individual data points are shown as red dots and the mean of each cluster is shown as a blue square with vertical lines indicating a width of two standard deviation. The expected location of the first caustic is in excellent agreement with the theoretical prediction, show with a grey line.

the author in early stages of this work. This arises mainly due to the representation of the randomness field in computer code as a matrix, which structurally does not respect the continuity condition at $\tilde{s} = 0, 2\pi$ which leads to a small bias in interpolation around $\tilde{s} = 0, 2\pi$. This is mitigated by a sufficiently fine discretisation in the circumferential direction when generating the random field.

3.5 Scaling law from finite element elastodynamics

The scaling of the first caustic resulting from the analysis of ray equations can also be obtained numerically from finite element elastodynamic simulations. The emergence of branched flows is clearly visible from finite element elastodynamics simulations; an example of which is shown in Figure 3.14. 'Snapshots' of the temporal evolution of an

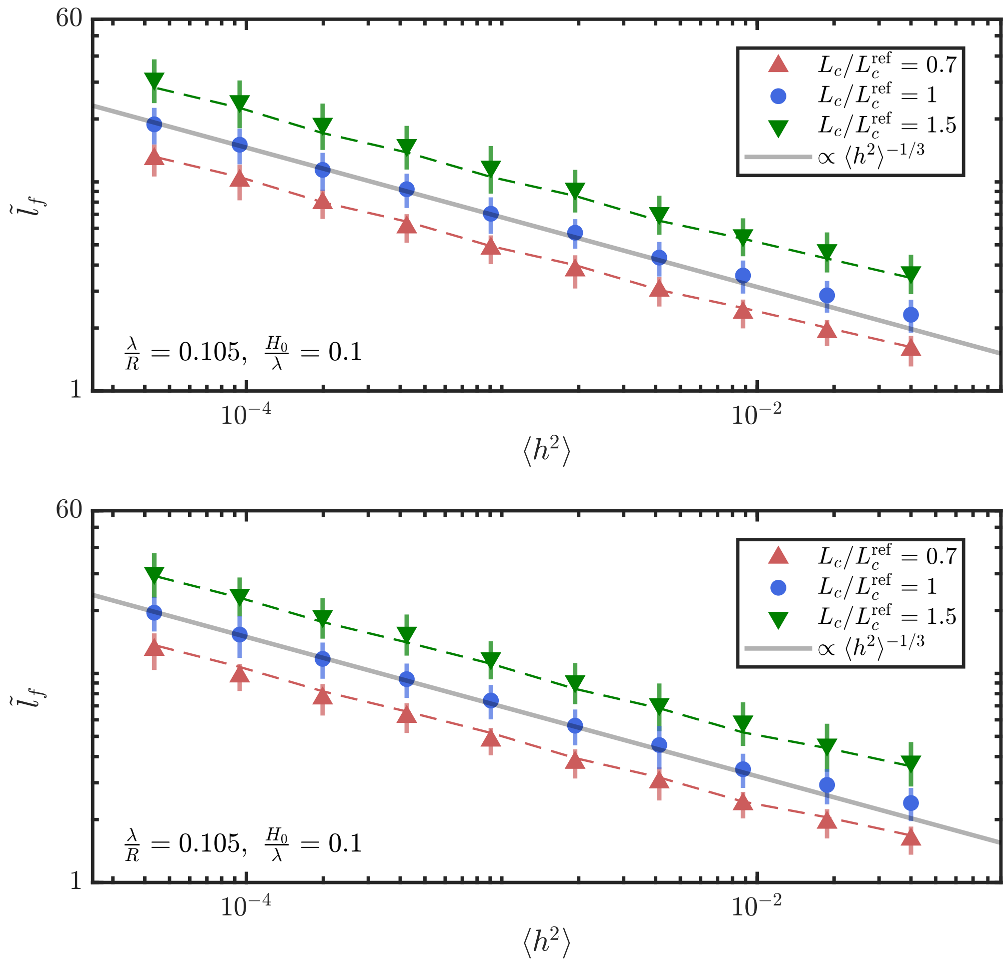

FIGURE 3.9: Scaling of location of the first caustic with correlation length of randomness (top - Pierce, bottom - Yu). Blue circular markers show the scaling of $\langle l_f \rangle$ for a reference correlation length. Predictions made assuming this as reference and a linear scaling with correlation length (dashed lines). The results of the numerical ray integration show (red and blue triangular markers) excellent agreement with this prediction.

initially plane wave front, as it propagates along the elastic cylinder with non-uniform thickness are shown in a sequence (a → b → c → d). In each panel, the entire domain is shown on the top and regions of high amplitude, indicated by colored lines, are zoomed into and shown on the bottom. The radial displacement has been greatly exaggerated for representational purposes. Note that the absolute value of displacement can be scaled arbitrarily since we are considering the linear displacement regime. The initially plane wave front (a) splits into distinct branches (b) leading to regions of extreme amplitudes. As the wavefront propagates further (c, d) more branching is observed. The widening of the wavefront as expected because of the dispersive nature of flexural waves in shells as seen here.

A technique similar to the one used in chapter 2 and in the existing branched flow literature [49] is used here to detect the location of the first caustic from FE simulations. For each simulation, the displacement fields are used to construct the

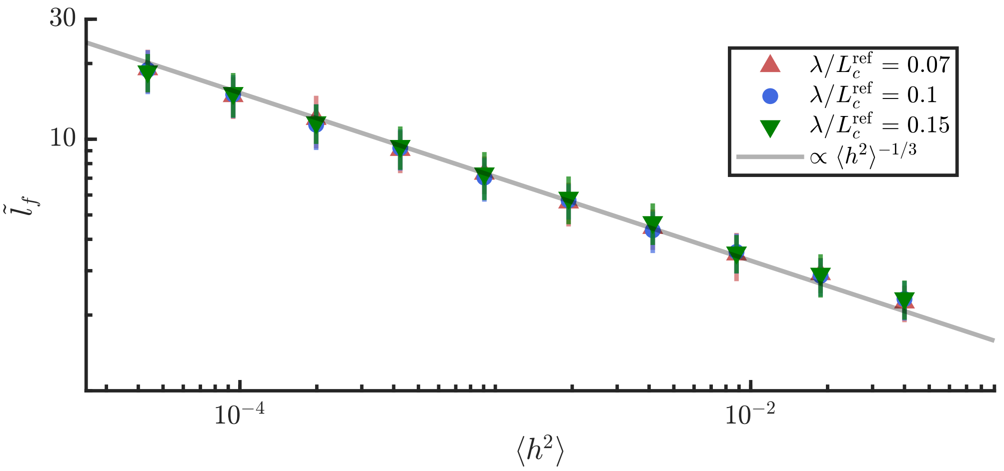

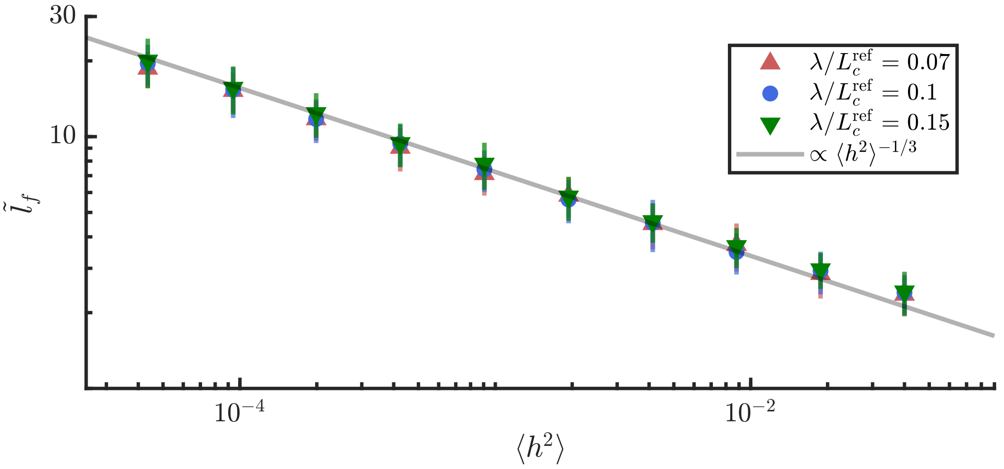

FIGURE 3.10: Scaling of location of the first caustic (top - Pierce, bottom - Yu) with wavelength (top - Pierce, bottom - Yu). Note that $\langle l_f \rangle$ shows no sensitivity to almost a 100% change in the value of the wavelength.

integrated intensity, $I(\tilde{x}, \tilde{s}) = \int_0^T \eta^2(\tilde{x}, \tilde{s}, t) \mathrm{d}t$. This is, in turn, used to construct the scintillation index, $S(\tilde{x}) = \langle I^2 \rangle_{\tilde{s}} / \langle I \rangle_{\tilde{s}}^2 - 1$. The location of the first significant peak of $S(\tilde{x})$ indicates the location of the first caustic (see Figure 3.15).

Using this approach of detecting the first caustics, the scaling of location of the first caustic with the statistical properties of the random field is explored. Figure 3.16 shows results for the distance of the first focusing event from the point of launch as a function of the severity of randomness for 80 realisations of the shells for each value of $\langle h^2 \rangle$ considered. The mean l_f for each value of $\langle h^2 \rangle$ considered is shown by a blue square marker which is close to the scaling $\langle l_f \rangle \sim \langle h^2 \rangle^{-1/3}$ that was derived analytically (shown as a grey curve).

The linear scaling of the location of focusing with the correlation length $\langle l_f \rangle \propto L_c$ is also validated using finite element simulations, see Figure 3.17. Using the curve obtained for $L_c / L_c^{\mathrm{ref}} = 1$ as reference, the prediction assuming the linear scaling with L_c is shown using dashed lines. The actual simulations (markers) agree well with this

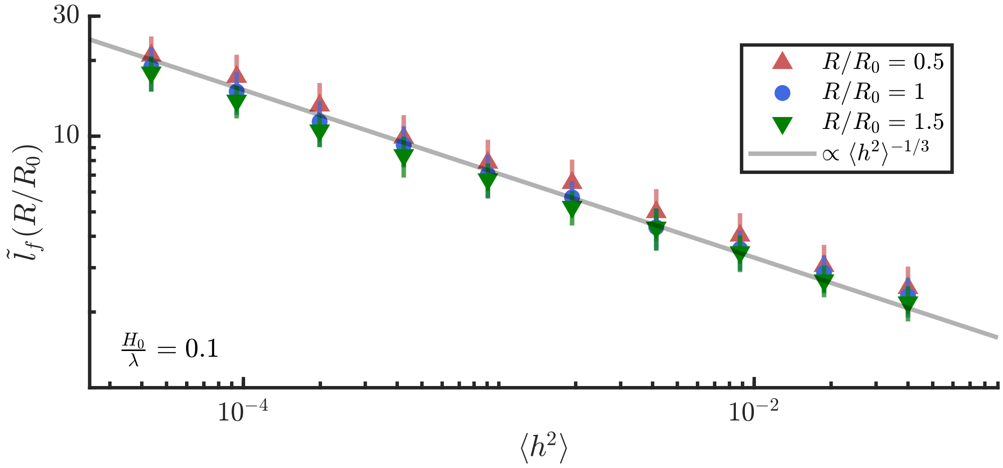

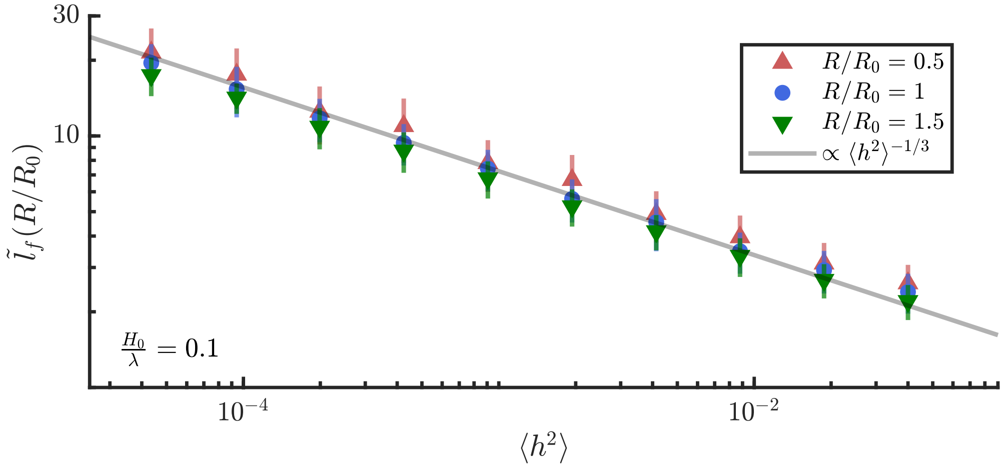

FIGURE 3.11: Scaling of location of the expected location of the first focusing event (top - Pierce, bottom - Yu) with the radius of the cylinder. Scaling of the expected locations of the first caustic with radii from numerical ray integration. The expected location of the first caustic is independent of the radius in the parameter ranges of interest.

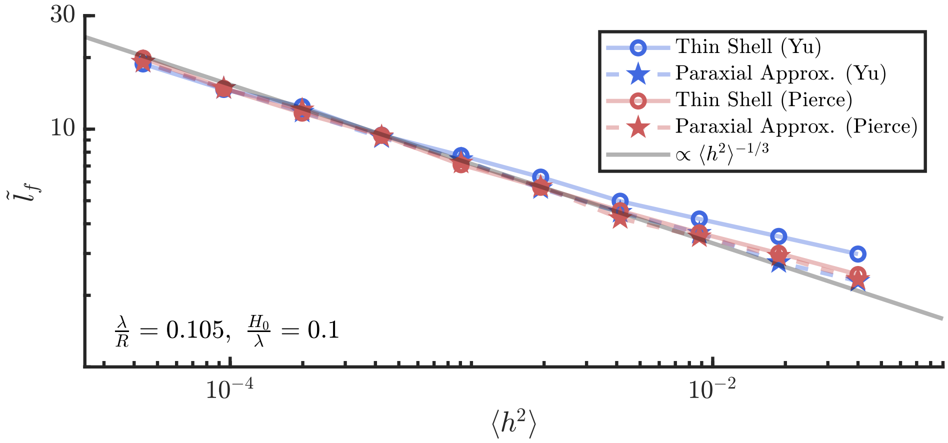

FIGURE 3.12: Comparison of $\langle l_f \rangle$ obtained from thin shell and paraxial ray equations from Pierce's and Yu's formulations. Thin shell equations from Yu's formulations shows significant deviation from the expected scaling at higher $\langle h^2 \rangle$, as expected.

ignoring all higher order effec

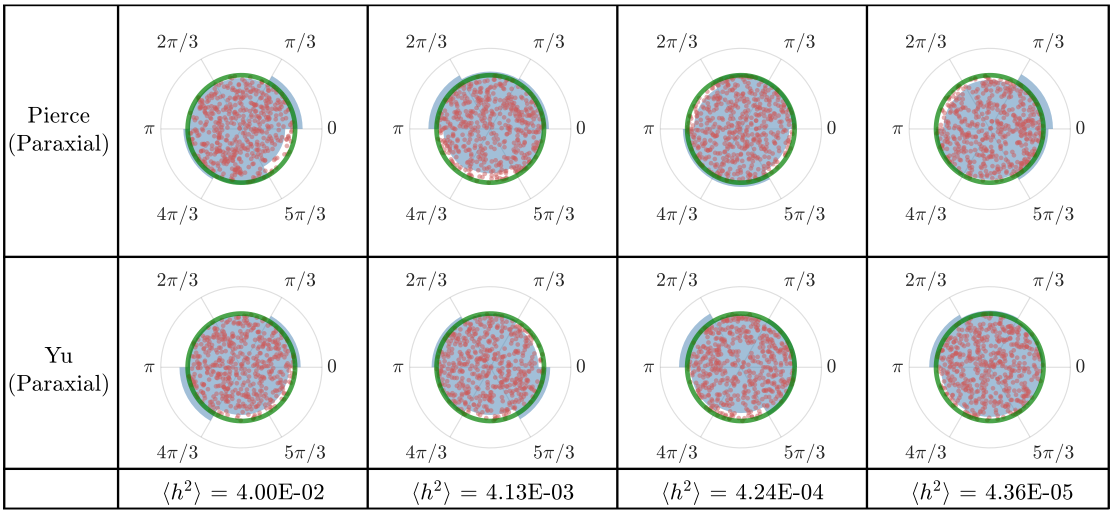

FIGURE 3.13: Histograms of angular locations of the first focusing events obtained from numerical ray integration. Polar histograms of the angular locations, shown in blue, show no consistent appreciable angular bias. The green circle indicates the outline of a polar histogram with perfectly zero angular bias. The individual data-points used to construct the histograms are shown with orange dots. Their angular location is the one obtained from simulations; their radial position in the above plots is randomised in the interest of visualisation.

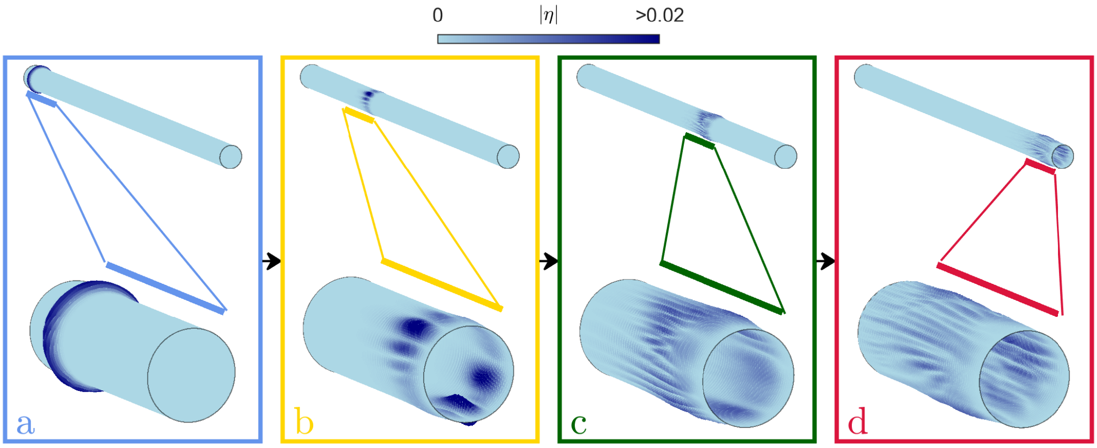

FIGURE 3.14: Emergence of branched flow of an initially plane wavefront in a thin cylinder of non-uniform thickness. Temporal evolution (a → b → c → d) of an initially plane flexural wave front in a thin elastic cylinder of non-uniform thickness. The full cylinder has been shown on the top of each panel. The regions of high amplitude at each time instant is indicated with colored lines and they been zoomed into and shown at the bottom of each panel. The emergence of branching leading to locations of extreme amplitudes and widening of the wavefront consistent with the dispersive character of this class of elastic waves is also observed.

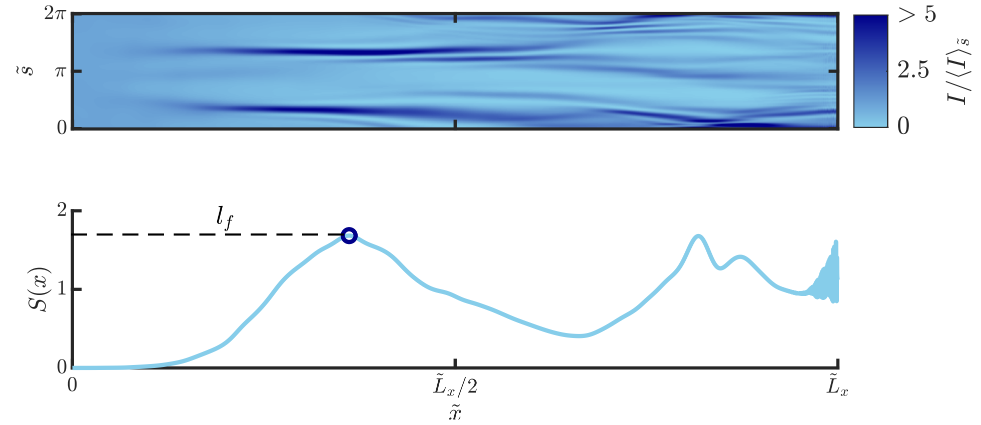

FIGURE 3.15: Plot of integrated intensity (top) and scintillation index (bottom) of an exemplar FE simulation. Note that the integrated intensity has been normalised along by the mean along the circumferential direction for visually emphasise the locations of extreme amplitudes. The first prominent peak (circular marker) of the scintillation index ($SI(x)$) curve indicates the location of the first caustic (l_f).

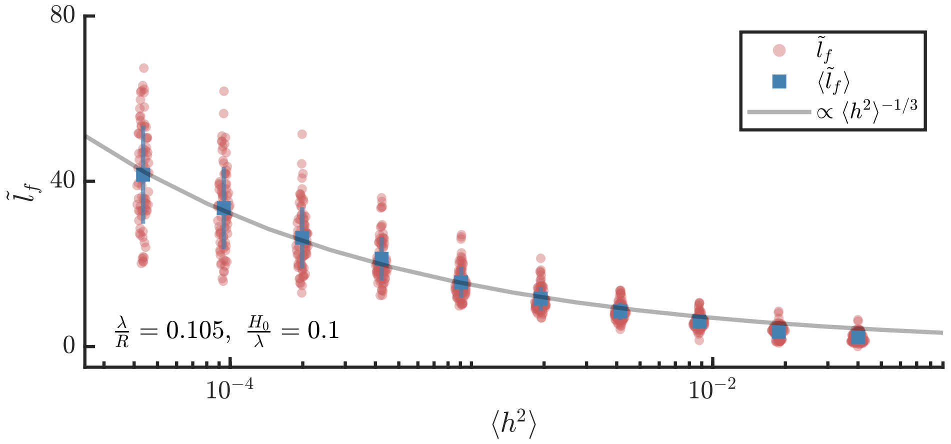

FIGURE 3.16: Scaling of location of the expected location of the first focusing event with "severity" of randomness as obtained from finite element simulations. Circular markers indicate locations of first caustic from individual simulations. Square markers show the expected location of the first caustic. Vertical lines indicate 2 standard deviation (centered around the mean). The expected locations of the first caustic show the expected power law scaling with $\langle h^2\rangle$.

prediction. In the results from FE elastodynamics simulations, the scaling seems to diverge from the prediction at higher values of $\langle h^2\rangle$; this is expected since the weak scattering assumption breaks down at these values of $\langle h^2\rangle$. This does not happen in the simulations using numerical integration of ray equations, since we use the formulation obtained from applying the paraxial approximation which assumes weak scattering.

The insensitivity of $\langle l_f\rangle$ to wavelength (for $\lambda \ll L_c$) is also confirmed, see Figure 3.18. The expected breakdown of the scaling due to strong scattering is seen here.

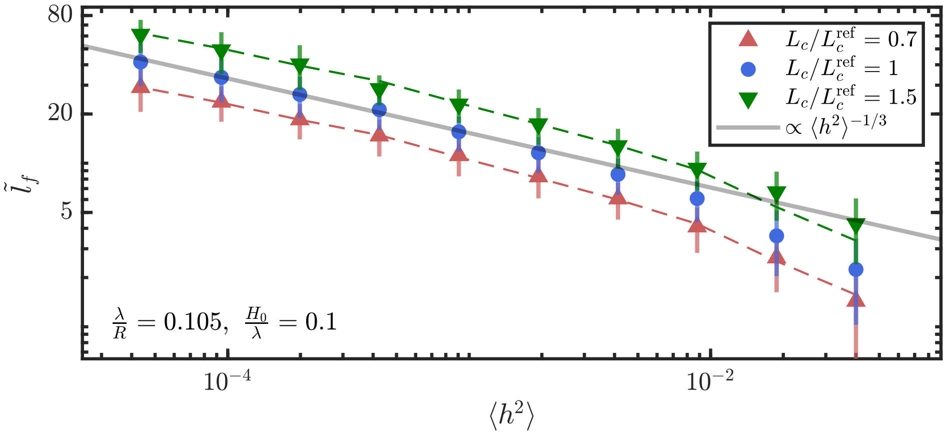

FIGURE 3.17: Scaling of location of the expected location of the first focusing event with correlation length of the randomness from FE simulations. Taking the curve corresponding to $L_c/L_c^{\mathrm{ref}} = 1$ to be the reference, dashed lines show the predicted behaviour at other correlation lengths assuming $\langle l_f \rangle \propto L_c^1$. The actual simulations agree well this prediction hence confirming the linear scaling.

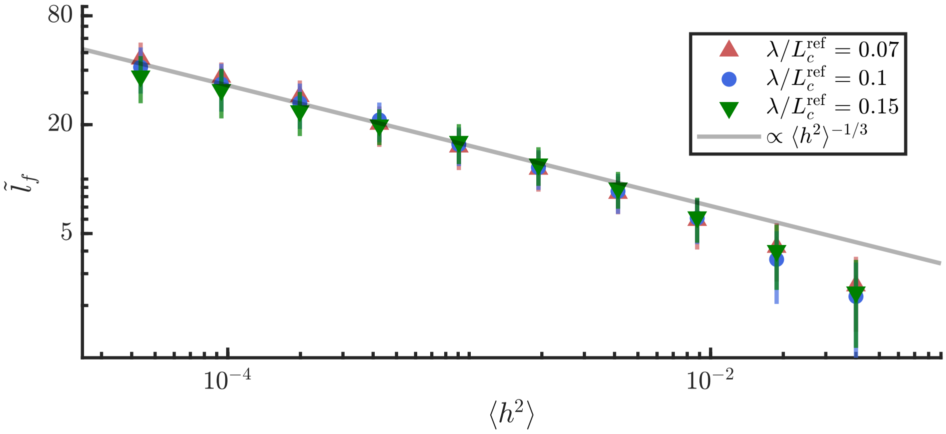

FIGURE 3.18: Scaling of location of the expected location of the first focusing event wavelength of the initial wavefront from FE simulations. As long as $\lambda \ll L_c$, $\langle \tilde{l}_f \rangle$ is independent of wavelength. The power law scaling seems to break down at higher $\langle h^2 \rangle$. This is consistent with the expectation that the scaling holds only for weak scattering and higher $\langle h^2 \rangle$ corresponds to higher scattering.

The insensitivity of $\langle l_f \rangle$ to variations in the radius of the cylinder is not verified using finite element simulations due to the prohibitive computational cost involved.

3.6 Remarks on numerical methods used

According to the paraxial approximation, rays travel at a constant speed in the main propagation direction. This enables calculation of the total time the rays would take to travel the entire length of the cylinder. The time stepping in the numerical ray simulations is set using this to ensure that there are 2000 time steps in the full length

Variable Name	Symbol	Units	Value(s)
Young's Modulus	E	MPa	**200**
Density	ρ	$\mathrm{kg\,m^{-3}}$	**7800**
Poisson's Ratio	ν	1	**0.3**
Correlation length	L_c	m	**0.1**, 0.07, 0.15
Radius	R	m	**0.0955**, 0.0477, 0.1432
Wavelength	λ	m	**0.01**, 0.007, 0.015
Nominal thickness	H_0	m	**0.001**
Length in propagation direction	L_x	m	4, 8 -depending on $\langle h^2 \rangle$

TABLE 3.1: List of parameters used in numerical ray integration and FE simulations for all the results presented here. When it is unclear from context, it may be assumed that the parameter values in bold face were used.

traversal. This time stepping is adequate since no variation is seen in the rays when the time steps are varied around 2000. Another way of being confident in the adequacy of the time stepping is to note that the time steps roughly corresponds the same number of steps the main propagation direction and 2000 steps is adequate to capture the features in the main propagation direction, which are of the order of the correlation length i.e ($L_x/2000 \ll L_c$). Note that one is unable to use purely physical arguments to arrive at the time step since the time scaling for ray equations is arbitrary as shown earlier.

For the FE elastodynamics simulations, a combination of physical arguments and some trial and error is used to find the total time of the simulations. The time step is set to $\frac{\pi}{4\omega}$, this ensures that there are 8 points per cycle since the forcing has predominant frequency component of ω. The cylinder is meshed using rectangular element which have the dimensions $\lambda/8$ and $3\lambda/8$ in the axial and circumferential directions respectively. Note that the meshing can be slightly coarser in the circumferential direction since the wave predominantly travels in the axial direction and hence has only modest variations along the circumference. The element aspect ratio of 1:3 is inadvisable in general for 2D elements, however, since we are confident that the variations in the circumferential direction are modest, this aspect ratio will not lead to ill conditioning or mis-estimation of results. The spatial discretisation of $\lambda/8$ ensures that the spatial variation due to a wave of predominant wavelength λ is adequately captured. Admittedly, since the system being studied is dispersive, wavelengths shorter than λ will also be excited and the chosen discretisation may not model them well. The computational expense of these FE simulations must be emphasised here and this is the reason behind some compromises in the choices made during meshing. Details of other parameters used in numerical ray integration and FE simulations is in Table 3.1.

3.7 Conclusions

There appears to be a universality of branched flows in the propagation of elastic waves through random media. Following the results in chapter 2 showing the existence of on branched flow in elastic plates [4], here analogous behaviour for shells with correlated random properties is demonstrated. The ray equations for flexural waves in a thin elastic cylinder are derived from two different formulations, [3, 131]. A paraxial approximation, permitted by the parameter regimes of interest, is applied to the ray equations. This is used to analytically demonstrate that the expected location of the first caustic in shallow cylinders shows the scaling $\langle l_f \rangle \propto L_c \langle h^2 \rangle^{-1/3}$ (from both formulations considered). This scaling was then corroborated using numerical integration of ray equations and full FE elastodynamic simulations.

An immediate extension of this work on cylindrical elastic shells would be to explore the dependence of the scaling of the first caustic with the radius for shells with *appreciable* curvature (i.e small radius). One is unable to do so in this work since the requirement of $2\pi R \gtrsim L_c$ limits how small the radius can be. This can be remedied by using anisotropic randomness which would enable reduction of the radius by the use of a smaller correlation length in the circumferential direction. There may be an interesting scaling of $\langle l_f \rangle$ with radius in this parameter regime. The existing literature on branched flows in media with spatially anisotropic randomness [56] can be leveraged. Another possible extension is the study of branched flow in ultra-thin" shell regime where membrane modes may couple with flexural modes. This may in fact be driven by non-uniform thickness. It would be interesting to explore the emergence of high amplitudes due to random focusing in a system with significant energy transfer between flexural and membrane modes.

Chapter 4

Standing waves in plates with periodically attached pillars: Chladni patterns

Having considered travelling waves in plates with spatially correlated randomness in properties in Chapter 2, we now turn to standing waves in plates that possess periodic heterogeneity. Periodicity is provided to the system by a lattice of flexible pillars that are attached to the plates, so that during motion they must follow the plate surface deflection as well as slope. This configuration provides an interesting toy problem to investigate the role of interaction of a group of flexible structures with a wave-bearing continuum. Another motivation of this arises from many practical structures that possess such generic features. For example, heat exchangers frequently comprise a bank of parallelly running tubes that are coupled – often at their ends – by elastic plates. Spatial patterns arising in the the standing waves of plates are well known, as they give rise to Chladni patterns. Here we study the spatial patterns generated by standing waves in a system that possesses elastically connected flexible pillars.

When standing waves are set up in an elastic plate, nodal patterns emerge along lines separating motion with opposite phases i.e. moving in opposite directions—an observation attributed to Chladni [79], the pattern being popularly known as Chladni figures. Although Chladni's original experiments refer to a plate driven near one of its resonant modes, the term has come to be used with the nodal patterns in a host of normal modes such as those found in the acoustics of musical instruments, e.g. violins [149], guitars [150] and tabla [151]. The generic use of the word has been used to describe even nodal patterns of wave functions in quantum mechanics. In the same spirit, nodal patterns presented by an elastic structure consisting of an array of pillars on a thin plate will be explored in this chapter. The need for experimental validation as well as spatial visualisation of resonant elastic structures has motivated the

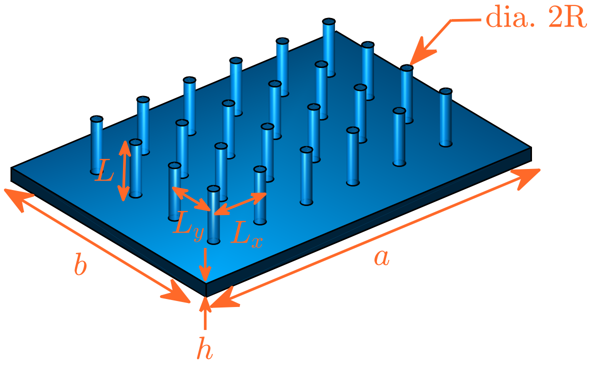

FIGURE 4.1: Schematic of the pillared plate under consideration. Dimensions are not to scale.

development of a host of modern experimental techniques such as laser Doppler vibrometry [152], defect-selective imaging [153] and holographic interferometry [154].

Systems consisting of identical pillars fixed perpendicularly to an elastic plate have been studied as an example of a configuration that could come under the general class of acoustic meta-materials [88, 89]. They show a remarkable ability to suppress vibrations within a certain band of frequencies [80–84]. This band can be 'tailored' by changing geometric and material parameters of the systems [85–87]. A recent work by Mishuris et al. [90] studies the general wave propagation problem of a "master" structure with distributed oscillators. The results obtained in these studies are usually valid exactly only for systems spanning an infinitely large domain. Limited studies have been carried out to explicate response of such systems with finite domain. Moreover, an analysis from a modal point of view seems to be missing from the literature as typically a wave approach and band-gap phenomena are often of interest. In this chapter, we consider the modal vibration of a pillared plate structure which is schematically represented in Figure 4.1.

Some initial numerical experimentation carried out by the author on a pillared plate with simply supported edges using FEM showed that, in the mode shapes, the tip defection of the pillars has a spatial phase relationship (see Figure 4.2). Based on this insight, a Rayleigh quotient based model of the modal vibration of a pillared plate is constructed. This model is expected to be very computationally efficient compared to FEM simulations. This would, therefore, enable rapid calculation of modal frequencies and would also provide a direct insight into how the modal frequencies change with geometric and material parameters. Furthermore, this model is then compared against

FEM simulations. This is followed by a discussion on modal density and brief discussion on a technique to 'polarise' the spatial phase of such systems.

One of the original motivations of the study presented in this chapter, with application to heat exchangers, is that damage is seen at certain locations and we were interested in the modal behaviour and to recognise whether one could have a 'rogue' component or the assembly essentially in some modes could be a composite assembly moving as a single body. A possible explanation of the said 'rogue' component's behaviour may also signal an Anderson localisation [106]-like due to small defects introduced during manufacture and assembly. This 'rogue' phenomenon has been reported previously, in industrial settings, in the case of bladed disks [155]. This is, however, not explored in the present work.

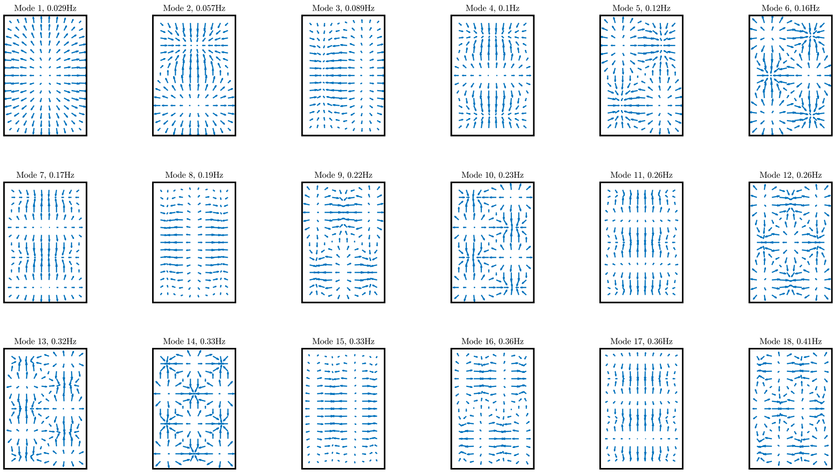

FIGURE 4.2: Plot of deflection of the tip of the resonators/pillars in different mode shapes obtained from finite element simulations. Note the apparent "spatial phase" relationship.

4.1 Analytical model of vibrational modes of a pillared plate

A Rayleigh quotient approximation is constructed to find the normal mode frequencies of a pillared plate assembly as described above. Based on some numerical experiments, the *ansatz* that the base plate deflection shape is always one of the mode shapes of a thin elastic plate with simple supports on all edges is arrived at.

As shown in Figure 4.1, we consider a thin elastic plate of size $a \times b$ in the $x - y$ plane, $0 \leq x \leq a, 0 \leq y \leq b$, and thickness h. This 'base' plate is decorated with identical cantilevered pillars (resonators) of length L, affixed to it in a rectangular lattice configuration. The resonators have a regular spacing of L_x and L_y in the x and y directions respectively and have a circular cross-section of radius R. The resonators are all made of the same material which has Young's modulus E_{R}, density ρ_{R} and Poisson's ratio ν. The plate material has density ρ_{P}, Young's modulus E_{P}, Poisson ratio ν and therefore a bending stiffness $D_{\mathrm{P}} = E_{\mathrm{P}}h^3/12(1-\nu^2)$.

4.1.1 Energy expressions for the base plate

During normal mode motion, the temporal part of the motion is sinusoidal, so the transverse deflection can be expressed as

$$w(x,y,t) = W(x,y)\cos\omega t, \tag{4.1}$$

where $W(x,y)$ is the mode shape. We now make an approximation by using an assumed mode for the plate part that it is the same as the mode shape of a plate with four simply supported edges. The transverse deflection (along the z axis, perpendicular to the $x-y$ plane) of this plate is assumed to be of the form

$$W(x,y) = A\sin(m\pi x/a)\sin(n\pi y/b) \tag{4.2}$$

where A is the amplitude. This assumed shape satisfies the *kinematic* boundary conditions for a simply supported plate at all its edges, i.e. $W(0,y), = W(a,y) = W(x,0) = W(x,b) = 0$. The potential energy $U_{\mathrm{P}}(t)$ of the plate (modelled as a Kirchhoff–Love plate) is given by,

$$\begin{aligned} U_{\mathrm{P}}(t) &= \frac{1}{2}D_{\mathrm{P}}\int_0^b\int_0^a \left((\partial_{xx}w+\partial_{yy}w)^2 - 2(1-\nu)\left(\partial_{xx}w\,\partial_{yy}w - (\partial_{xy}w)^2\right)\right)\mathrm{d}x\mathrm{d}y \\ &= \frac{1}{2}C_1A^2\cos^2\omega t, \end{aligned} \tag{4.3}$$

where $C_1 = \left[D_{\mathrm{P}}\pi^4\frac{(b^2m^2+a^2n^2)^2}{4a^3b^3}\right]$. The kinetic energy of the plate is given by

$$T_{\mathrm{P}}(t) = \frac{1}{2}\rho_{\mathrm{P}}h\int_0^b\int_0^a(\partial_t w)^2\mathrm{d}x\mathrm{d}y = \frac{1}{2}C_2\omega^2A^2\sin^2\omega t, \tag{4.4}$$

where $C_2 = \rho_{\mathrm{P}}h\frac{ab}{4}$.

4.1.2 Energy expressions for pillar resonators

Axial stress contributions can be ignored as they are expected to be small at lower modes. Hence, the pillars (resonators) can be modelled as Euler Bernoulli beams. Their deflection is assumed to be a combination of translation due to local deflection of the plate, transverse to its plane, which is also equal to that at the root of the elastic pillars, rotation such that the longitudinal axis of the resonator aligns with the local normal of the deflected plate and flexure in the shape of the first vibrational mode

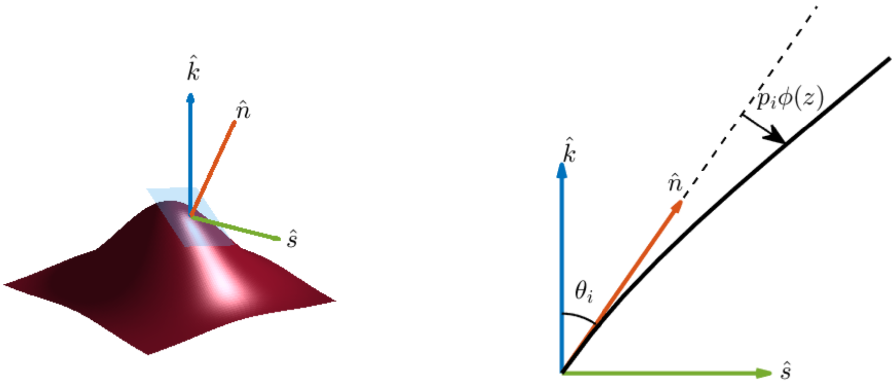

FIGURE 4.3: For any point on the deflected plate we can find the surface normal $\hat{n}$. If there is a resonator at this site (say the i^{th} one), we postulate that position of this resonator is given by a superposition of rotation such that its longitudinal axis aligns with $\hat{n}$ and flexure away from this longitudinal axis given by $p_i\phi(z)$. Here, $\phi(z)$ is the first bending mode of a cantilever beam.

shape of a cantilever beam $\phi(z)$ in the plane spanned by the vertical and the local surface normal. This assumption is justified from energy considerations at lower modes. See Figure 4.3 for a schematic representation of the same. Say, at the time instant t, the surface of the deflected plate is given by, $S : z - w(x, y, t) = 0$. The normal to the deflected surface is

$$\mathbf{n} = \nabla S = \begin{bmatrix} -A\cos(m\pi x/a)\sin(n\pi y/b)(m\pi/a) \\ -A\sin(m\pi x/a)\cos(n\pi y/b)(n\pi/b) \\ 1 \end{bmatrix} \cos(\omega t) \tag{4.5}$$

and the unit normal along the z axis is $\hat{\mathbf{k}}$. Here we are interested in lower vibrational modes and the linear displacement regime where the amplitude A is significantly smaller than the length of the sides (a, b). This implies that $Am\pi/a, An\pi/b \ll 1$. Also note that the highest magnitude the sinusoidal terms can have is 1. Therefore $\|\mathbf{n}\| \approx 1$ which implies that $\mathbf{n} \approx \hat{\mathbf{n}}$, i.e. $\mathbf{n}$ is, approximately, a unit vector. Further, let the angle between the vertical $\hat{\mathbf{k}}$ and normal to the surface S (at position of the resonator i), $\hat{\mathbf{n}}_\mathbf{i}$ be $\theta_i(t)$. Then by definition of the cross product we can write

$$\sin\theta_i(t) \approx \theta_i(t) = \|\hat{\mathbf{k}} \times \hat{\mathbf{n}}_\mathbf{i}\| = \left\| \begin{matrix} +A\sin(\frac{m\pi x_i}{a})\cos(\frac{n\pi y_i}{b})\frac{n\pi}{b} \\ -A\cos(\frac{m\pi x_i}{a})\sin(\frac{n\pi y_i}{b})\frac{m\pi}{a} \\ 0 \end{matrix} \right\| \cos(\omega t) = A\alpha_i\cos(\omega t). \tag{4.6}$$

where $\alpha_i = \sqrt{\sin^2(\frac{m\pi x_i}{a})\cos^2(\frac{n\pi y_i}{b})\frac{n^2\pi^2}{b^2} + \cos^2(\frac{m\pi x_i}{a})\sin^2(\frac{n\pi y_i}{b})\frac{m^2\pi^2}{a^2}}$. Let $\hat{\mathbf{s}}$ be the normalised projection of $\hat{\mathbf{n}}$ on the $z = 0$ plane. Hence for any material point at location z on the ith resonator, the deflection is

$$\mathbf{g}_\mathbf{i}(z, t) = w(x_i, y_i, t)\hat{\mathbf{k}} + (\theta_i z + p_i\phi(z))\cos(\omega t)\hat{\mathbf{s}} \tag{4.7}$$

and

$$\partial_t \mathbf{g_i}(z,t) = -\omega A\beta_i \sin(\omega t)\hat{\mathbf{k}} + -\omega(A\alpha_i z + p_i\phi(z))\sin(\omega t)\hat{\mathbf{s}}, \tag{4.8}$$

where, $\beta_i = \sin(m\pi x_i/a)\cos(n\pi y_i/b)$ and p_i is the tip displacement of the i^{th} pillar in the plane described by $\hat{s}$ and $\hat{k}$. Note that because θ_i is small, instead of projecting the deflection due to rotation of the base and bending of the resonators onto $\hat{k}$ and $\hat{s}$, the deflection is assumed to be completely along $\hat{s}$. This is simply tantamount to the approximations $\sin\theta_i = 0$ and $\cos\theta_i = 1$.

Hence, the kinetic energy of the ith pillar can be written as

$$T_i(t) = \frac{1}{2}\rho_{\text{R}}\pi R^2 \int_0^L \|\partial_t \mathbf{g_i}(z,t)\|^2 \text{d}z = \left[\frac{1}{2}C_{4,i}A^2 + \frac{1}{2}C_5 p_i^2 + 2\frac{1}{2}C_{6,i}p_i A\right]\omega^2\sin^2(\omega t) \tag{4.9}$$

where $C_4 = \rho_{\text{R}}\pi R^2(\beta_i^2 L + \alpha_i^2 L^3/3)$, $C_5 = \rho_{\text{R}}\pi R^2(\int_0^L \phi^2(z)\text{d}z)$, and $C_{6,i} = \rho_{\text{R}}\pi R^2\alpha_i(\int_0^L z\phi(z)\text{d}z)$.

Note that only the flexure of the resonators contributes to potential energy i.e $p_i\phi(z)$. The tip deflection (from $\hat{\mathbf{n}}_\mathbf{i}$) of the ith rod is p_i. The potential energy in the pillars that act as resonators can, therefore, be written as,

$$U_i(t) = \frac{1}{2}D_{\text{R}}\int_0^L (\partial_{zz}(p_i\phi(z)\cos(\omega t)))^2\text{d}z = \frac{1}{2}C_3 p_i^2\cos^2(\omega t) \tag{4.10}$$

where $C_3 = D_{\text{R}}\int_0^L \phi''^2(z)\text{d}z$ and $D_{\text{R}} = \pi R^4 E_{\text{R}}/4$.

4.1.3 Global matrices of a pillared plate

The energy terms, that are quadratic forms, can be summed up to obtain global matrices. If the unknowns are treated as the generalised coordinates of the problem and arranged into the vector $\mathbf{v} = [p_1\ p_2\ \ldots\ p_{N_r}\ A]^T$, then the total potential energy is

$$U(t) = \sum_{i=1}^{N_{\text{r}}} U_i(t) + U_{\text{P}}(t) = \frac{1}{2}\cos^2(\omega t)\mathbf{v}^T\mathbf{K}\mathbf{v}, \tag{4.11}$$

where

$$\mathbf{K} = \begin{bmatrix} C_3 & & & \\ & \ddots & & \\ & & C_3 & \\ & & & C_1 \end{bmatrix} \tag{4.12}$$

is the stiffness matrix and is a diagonal matrix of size $(N_r + 1) \times (N_r + 1)$. Similarly, the total kinetic energy of the the system is

$$T(t) = \sum_{i=1}^{N_{\text{r}}} T_i(t) + T_{\text{P}}(t) = \frac{1}{2}\omega^2\sin^2(\omega t)\mathbf{v}^T\mathbf{M}\mathbf{v}, \tag{4.13}$$

where

$$\mathbf{M} = \begin{bmatrix} C_5 & & & C_{6,1} \\ & \ddots & & \vdots \\ & & C_5 & C_{6,N_r} \\ C_{6,1} & \dots & C_{6,N_r} & C_2 + \sum_{i=1}^{N_r} C_{4,i} \end{bmatrix} \tag{4.14}$$

is the mass matrix and is almost a diagonal matrices of size $(N_r + 1) \times (N_r + 1)$ with the last row and column filled fully.

In normal mode vibration, conservation of energy implies that the maximum potential energy and maximum kinetic energy in the system must be equal. This is due to the synchronous motion of all constituent elements of the continua during normal mode motion.

The expressions for $U(t)$ and $T(t)$ (Equation 4.11 and 4.13 respectively) can be used to find maximum potential and kinetic energy by simply discarding the squared sinusoidal terms since the maxima of these terms is unity. Then, conservation of energy yields $\mathbf{v}^\mathbf{T}\mathbf{K}\mathbf{v} = \omega^2\mathbf{v}^\mathbf{T}\mathbf{M}\mathbf{v}$. From the variational principle, we know that the Rayleigh quotient $\mathbf{v}^\mathbf{T}\mathbf{K}\mathbf{v}/\mathbf{v}^\mathbf{T}\mathbf{M}\mathbf{v}$ must be stationary for normal mode motion. This means differentiating the quotient with respect to $\mathbf{v}$ and setting that to zero. Rearranging this, one obtains the generalised eigenvalue problem $\mathbf{K}\mathbf{v} = \omega^2\mathbf{M}\mathbf{v}$.

Therefore, the mode shapes $\mathbf{v}$ and modal frequencies ω can be found by solving the eigenvalue problem $\mathbf{K}\mathbf{v} = \omega^2\mathbf{M}\mathbf{v}$. Note that, only the eigenvector corresponding to the lowest eigenvalue, for each specified m, n corresponds to a mode shape of the pillared plate. Hence, to obtain multiple modes of the pillared plate, the eigenvalue problem must be solved repeatedly with different values of m, n while retaining only the eigenvector corresponding to the lowest eigenvalue.

4.2 Modal analysis using finite element simulations

The presented model is validated using finite element simulations (FE) of a rectangular plate decorated with equally spaced cantilevered beams. The parameters used for this are tabulated in Table 4.1

Finite element simulations were carried out using ANSYS MAPDL where the base and resonators were modelled using SHELL181 and BEAM88 [118] elements respectively. Modal analysis was carried out with simple supports on all edges of the plate using the internal PCG Lanczos solver.

Variable Name	Symbol	Units	Value(s)
Plate length	a	m	11
Plate width	b	m	16
Pillar separation in x direction	L_x	m	1
Pillar separation in y direction	L_y	m	1
Young's modulus of the plate	E_P	MPa	200
Young's modulus of the pillars	E_R	MPa	20
Density of plate	ρ_P	$\mathrm{kg\,m^{-3}}$	7800
Density of pillars	ρ_R	$\mathrm{kg\,m^{-3}}$	7800
Thickness of the plate	h	mm	1
Poisson's ratio of the plate	ν	1	0.3
Length of pillar	L	m	0.8
Radius of pillar cross section	R	mm	1

TABLE 4.1: List of parameters used in FE simulations.

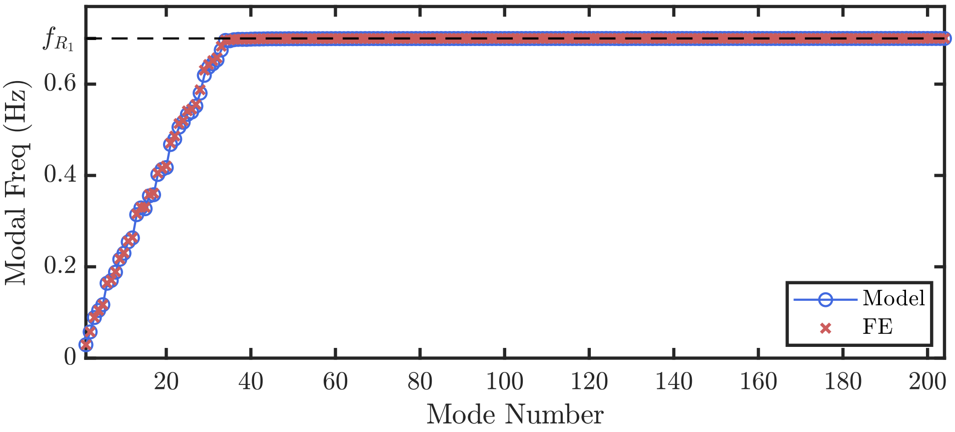

FIGURE 4.4: Comparison of modal frequency obtained from FE simulation and analytical model developed in this work.

4.3 Results and discussions

4.3.1 Modal Frequencies

The modal frequencies obtained from FE simulations are now compared with those obtained from the analytical model presented above. It can be seen from Figure 4.4 that the simulation and the model are in excellent agreement with each other. The high density of modes around the first natural frequency of the identical resonators f_{R_1} is also apparent.

4.3.2 Mode shapes (and their ordering)

The modal frequency of the modes obtained from the proposed model agrees well with those obtained from FE simulations. Now, the validity of the mode shapes will be assessed.

One of the most popular ways to compare mode shapes is the Mode Assurance Criteria (MAC)[156]. Consider two mode shapes expressed as vectors **u** and **v**, then the quantity

$$\mathrm{MAC} = \frac{|\mathbf{u} \cdot \mathbf{v}|^2}{|\mathbf{u}|^2 |\mathbf{v}|^2}$$

is a measure of the 'closeness' of the two modes shapes being compared —MAC lies between 0 and 1 with 1 signalling identical modes shapes apart from arbitrary constant scaling. If there are two sets of mode shapes to be compared, the MAC for all pairing between the two sets can be obtained and represented as a matrix. If one set were identical to the other set, then the MAC matrix would be nearly an identity matrix. All the diagonal terms would be 1 and the off-diagonal terms would have small but non-zero values.

Since there is a cluster of modes near the natural frequency of the resonators, to compare the analytical model with FE simulation results, the modes obtained from the model must be rearranged before finding the MAC. The best way to do this is to take the two sets of mode shapes in the order they are obtained from the FEM and model respectively and generate the MAC matrix. This will almost surely not be strictly diagonally dominant, given the strong degeneracy in the system and numerical approximations. This means that the modes need to be ordered so as to maximise the diagonal dominance of the MAC matrix. If $A_{i,j}$ are the elements of the MAC matrix, the aforementioned is tantamount to minimising $\sum_{i=1}^{N_{\text{modes}}} \sum_{j=1}^{N_{\text{modes}}} A_{i,j}(i-j)^2$ by rearranging rows and columns. The author could not find a standard algorithm to achieve this. However, if one assumes that there is only one mode corresponding to a mode from the FEM, i.e there is an exact one-to-one pairing of modes from the model and FEM, one may simply seek to reorder the rows and columns of the MAC matrix to maximise its trace. This is a standard problem in combinatorial optimisation called the balanced assignment problem and can be solved in polynomial time using the Kuhn–Munkres algorithm (also called the Hungarian algorithm)[91, 157]. The effect of applying Hungarian algorithm can be seen in Figure 4.5. This can also be seen in Figure 4.6 where the elements of the diagonals of the unsorted and sorted MAC matrices are shown. It can be clearly seen that the sorting algorithm matches similar modes. This can also been seen in the sample set of plots of the mode shapes obtained from the FE simulations and analytical model.

4.3.3 Sonic crystals with "polarised" resonators

The model and simulations presented so far have been with resonators which are beams with circular cross-sections. This means that the bending stiffness of the beam is independent of the plane of bending, i.e. with respect to tip deflection in any

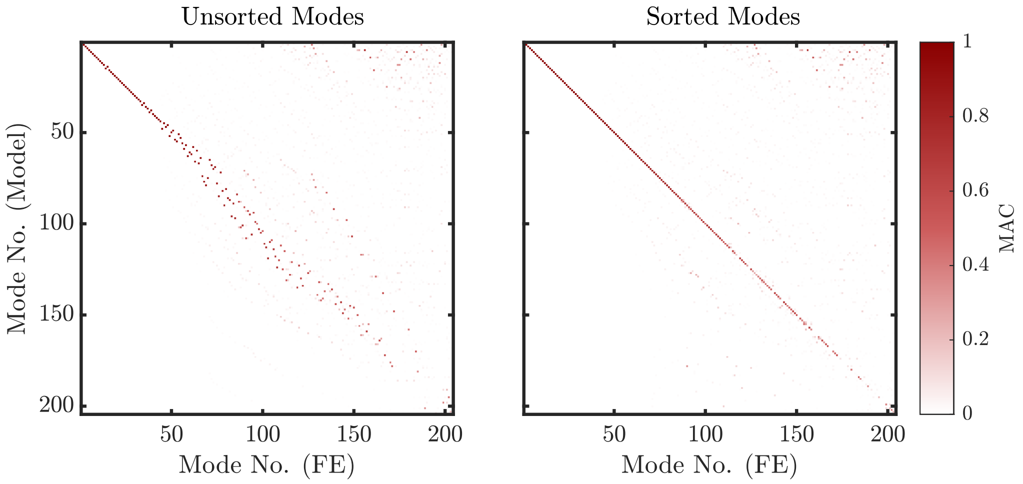

FIGURE 4.5: MAC number comparison of mode shapes obtained from the model developed in this work compared with mode shapes obtained from FE simulations. Due to many modes being close together in terms of frequency, there is a need to match mode shapes based on their MAC number and this can be done by maximising the trace of the MAC matrix. This is done using a standard algorithm in combinatronics. This leads to the sorted pairing of the modes (R) and we can see that the model predicts mode shapes with a degree of accuracy for at least the lower modes.

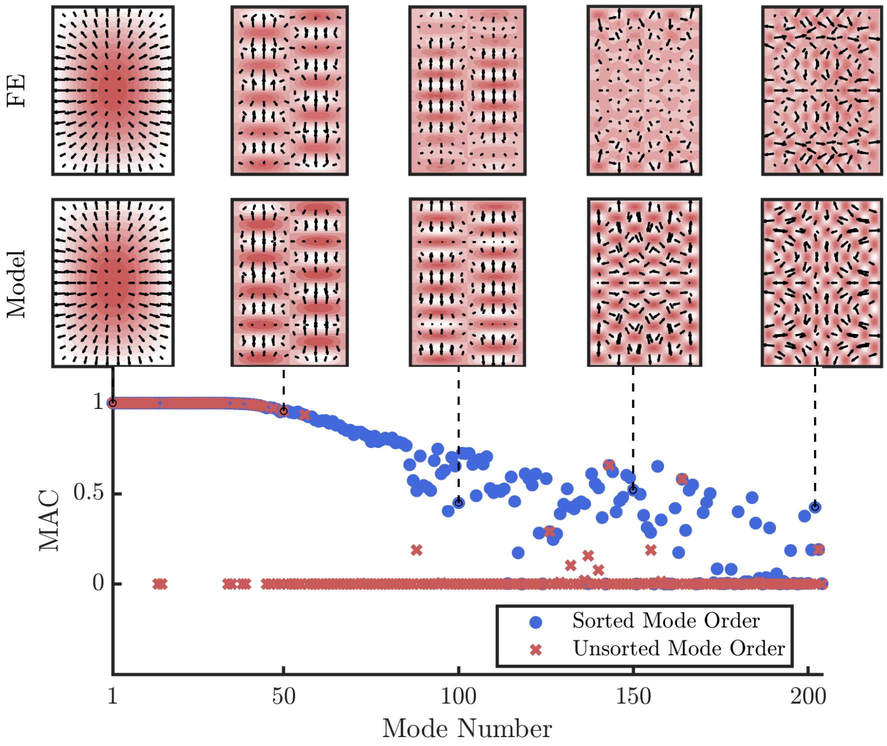

FIGURE 4.6: Diagonal of the MAC matrix plotted before and after reordering modes using the Hungarian algorithm. It can be clearly seen, by comparing the select mode shapes plotted above, that the sorting matches similar modes even though their frequencies are highly degenerate. Mode shapes are plotted to show the deflection of the base as a contour map and the deflection of the resonators are represented by arrows indicating tip deflection direction and magnitude.

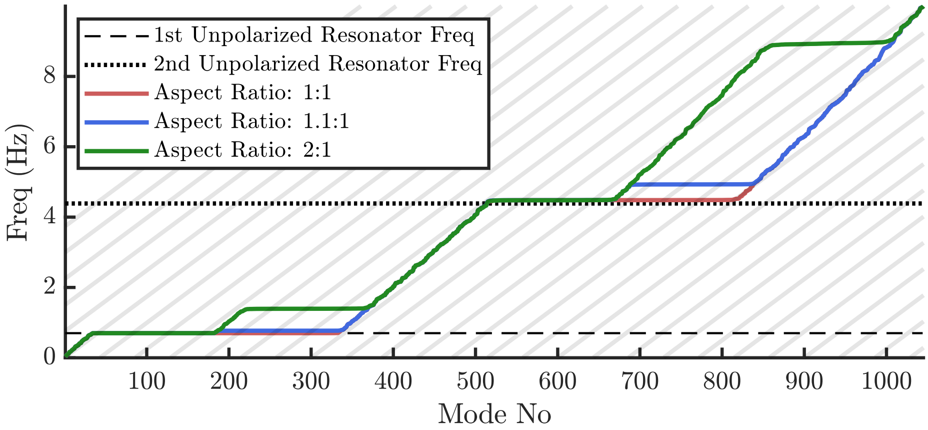

FIGURE 4.7: Polarisation causes the band gap to split. The magnitude of the split is dependent on the amount of polarisation (in this case, aspect ratio of cross-section of resonators). The slope of the grey transparent lines is given by the modal density of a uniform plate. It can be see that, outside the resonance band of the pillars, curves follow this slope. The slight departure from this trend may be explained by the discretisation approximations made when setting up the FE simulation.

direction in the $x - y$ plane. This will also be the case with a beam with a square cross-section also. However, if a beam with strictly rectangular cross-section–with unequal sides – is used, the resonators would have preferred directions where the bending stiffness would be lowest. Also, along these preferred directions, the bending stiffnesses would be different—a consequence of non-unit aspect ratio of the cross section. In the frequency spectra, this leads to “splitting” of the cluster of modes near the natural frequency of the resonators. This can be seen in Figure 4.7

4.3.4 Density of states in the elastic plate-pillar system

Modal density is a quantity that treats the number of modes as a continuously varying quantity and is frequently used within the so-called Statistical Energy Analysis (SEA). It is defined as the number of modes per unit frequency. For thin plates it is independent of frequency. Since modal density is an additive quantity, for the plate-pillar system it is basically the same as that of a regular plate with spikes or discontinuities at the location of the resonator frequencies. For N_{Res} polarised resonators, assume the resonator fundamental frequencies are $f^1_{R_1}, f^1_{R_2}$ and the first overtone or higher order is $f^2_{R_1}, f^2_{R_2}$, the modal density [158] is given by

$$\begin{aligned}\frac{\mathrm{d}N_{\mathrm{modes}}}{\mathrm{d}f} = \frac{ab}{2}\sqrt{\rho_B t/D_B} - (\rho_B t/D_B)^{1/4}\frac{a+b}{2\sqrt{2\pi f}} \\ + N_{\mathrm{Res}}\delta(f - f^1_{R_1}) + N_{\mathrm{Res}}\delta(f - f^1_{R_2}) \\ + N_{\mathrm{Res}}\delta(f - f^2_{R_1}) + N_{\mathrm{Res}}\delta(f - f^2_{R_2}).\end{aligned} \tag{4.15}$$

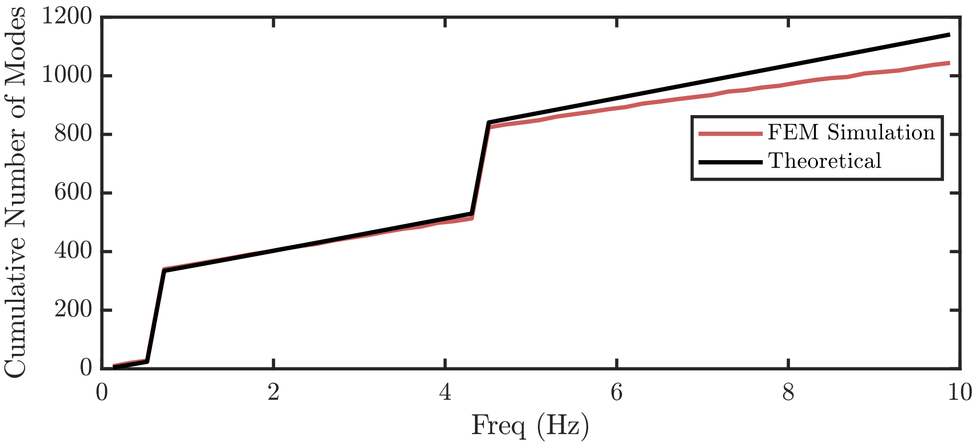

FIGURE 4.8: Cumulative number of modes in system with unpolarised resonators. The result from FEM is compared with the one proposed in this text.

For unpolarised resonators $f^1_{R_1} = f^1_{R_2}$ and $f^2_{R_1} = f^2_{R_2}$. See Figure 4.8 for a comparison of cumulative modes seen in FE simulations and that predicted by Equation 4.15. A plot of modal density where the "spikes" in density due to the resonators can be seen clearly in Figure 4.9. The effect of "polarisation" in splitting modal clusters is also apparent.

4.3.5 Engineering Chladni vector fields

When the bending stiffness of the beam is not isotropic with respect to direction of beam deflection there are "preferred" axes of deflection. These, typically, are the principal axes. Through a combination of orientation of the cross section of resonators, shape of the cross section, driving frequency and patterns of arrangement, one can perhaps produce "acoustic digital displays". This plan is currently speculative but see Figure 4.10 for an illustration of preferred axes in resonators with cross sections that are non-unity aspect ratio rectangles.

4.4 Conclusions

Arrays of rigid pillars as sonic crystals have been studied in the past [87], the motivation being construction of acoustic bands resulting from the scattering from an array of scatterers. Instead of acoustic wave propagation, here, the patterns arising from standing elastic waves were studied.

It has been shown that near the resonance frequency of the pillars represented as beams (effectively cantilevers), numerous (twice the number of beams affixed to the plate) roughly degenerate modes are seen. These modes feature low transverse

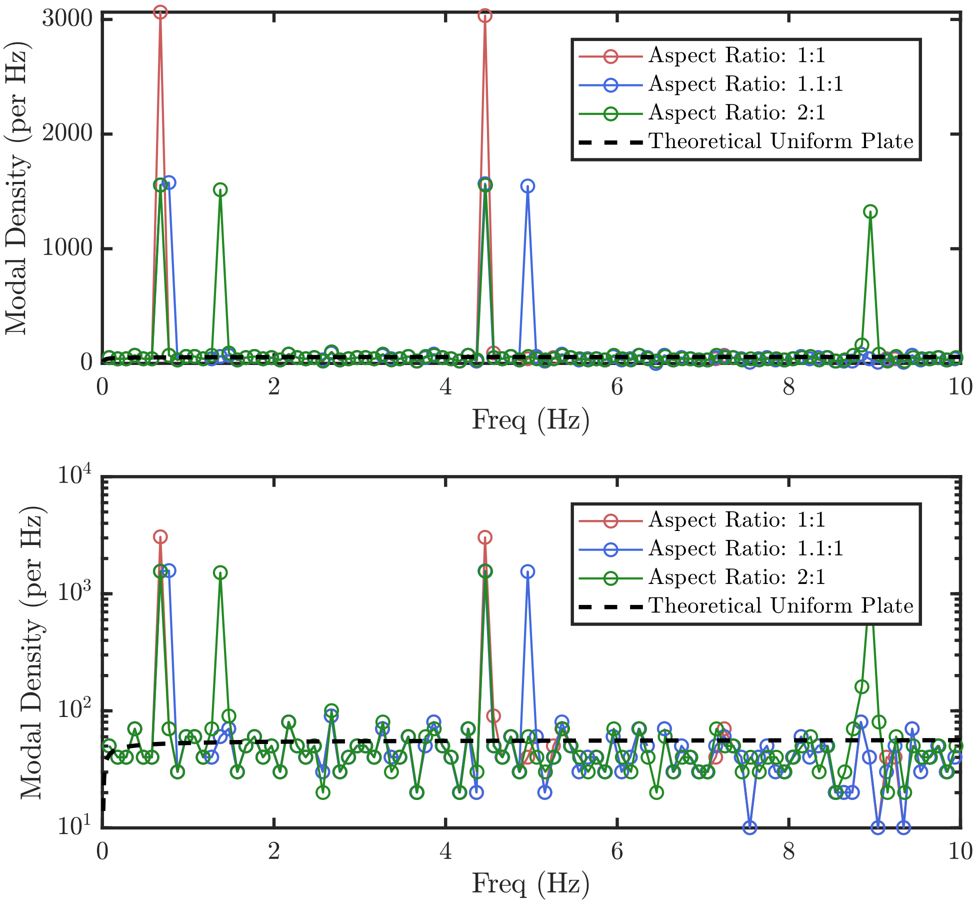

FIGURE 4.9: Effect of polarisation on modal density. Some peaks may appear merged due to frequency resolution used. (Bottom) Same plot in log scale.

deflection of the plate and higher transverse deflections of the beams in planes perpendicular to that of the plate. Taken together, they can be understood as bending modes of cantilevered beams on a non-rigid foundation albeit with very distinct spatial phase relationships in the magnitude of their tip deflections. These are reminiscent of the Chladni figures. Also shown is that even though the plate transverse deflection is minimal, the normals to the deflected plate dictate the said spatial phase of the beam tip deflections. This was done using a Rayleigh quotient based model which was developed and compared against finite element simulations.

By changing the cross-section of the beams to a rectangle of non unity aspect ratio, we introduce another ’lever’ to control the spatial phase relationship. The hypothesis posed that arises from this study is that this can form the basis of ’sonic crystal digital displays’.

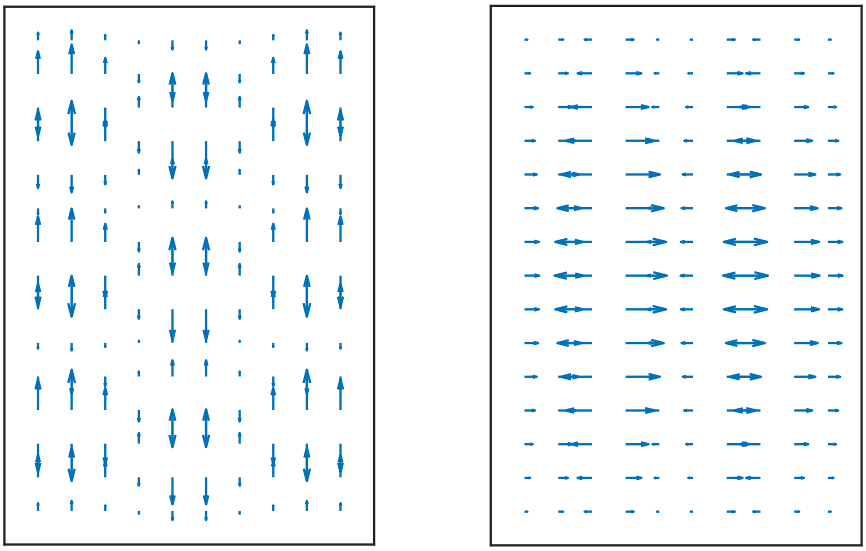

FIGURE 4.10: For resonators with rectangular cross sections with unequal sides, the two principal directions become "preferred" directions for tip deflections and the Chladni patterns of the sonic crystals are similarly modified. Shown here are typical examples of Chladni patterns in such sonic crystals. The two figure correspond to the Chladni patters seen in two different pass bands

Chapter 5

Long wave approximations for periodic structures: an industrial case study for tube-fin banks

In chapters 2 and 3, we studied the behaviour of wave propagation through a heterogeneous medium when the wavelength is much smaller than the correlation length of the heterogeneity. In two different domains – flat plates and cylindrical shells – emergence of branching patterns was reported in the presence of spatial randomness. Consider the opposite when the heterogeneity is placed closely compared to the wavelength, i.e. the correlation length of heterogeneity is much shorter than the wavelength of interest. Such situations are practically encountered frequently in industry, especially for low frequency vibration of periodically stiffened structures. When the length scale of heterogeneity in a waveguide is much smaller than the wavelength of interest, an elastic medium is expected to exhibit behaviour that resembles that of a continuum with effective properties. Detailed modelling is often computationally prohibitive, especially in a design scenario when several designs are to be assessed for their dynamical performance. Here we consider standing waves in such a waveguide, which provides us with the opportunity to represent a complex industrial assembly economically via a "*smeared properties*" model. Because such industrial assemblies are finite in size, it is convenient to consider standing waves and normal modes, rather than freely propagating waves.

Heat exchangers are often mounted onto engines and thus are exposed to substantial base excitation. Typically, they consist of parallel tubes that are nominally identical and are connected by end plates. Vibration tends to be one of the key engineering challenges in its design. An engineer designing them has to ensure that that the modal frequencies of the system meet the performance and life specifications. These specifications are often expressed in terms of bands of frequencies within which the

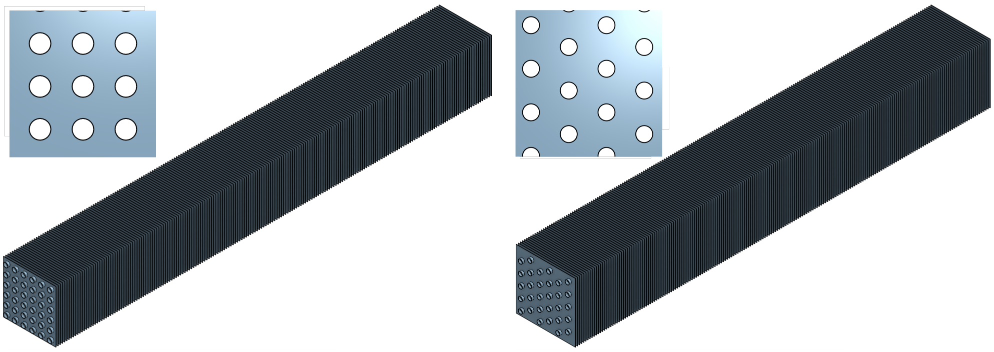

FIGURE 5.1: Schematics of tube and fin banks with tubes arranged in rectangular (left) and hexagonal (right) lattice configurations.

modal frequencies of the heat exchangers must not lie. The main functional and therefore, most critical, sub-component in traditional heat exchangers is a "bank" of tubes and fins (see Figure 5.1). Numerous identical metallic tubes are decorated with equally spaced thin metallic plates or "fins". The fins increase the surface area available for heat exchange and are usually arranged perpendicular to the tube axes.

The base excitation from the engines excites many modes of vibration in heat exchangers. However, the enclosure of heat exchangers is usually made of thick metallic plates that have resonant frequencies that are much higher than the dominant frequencies in the excitation. The long tubes, with fins contributing significant mass loading, on the other hand, can have much lower frequencies and can be appreciably excited by engine frequencies. The vibrational modes of the tube and fin bank are also called "core" modes. This chapter will focus on these vibrational modes.

Because of the complexity of tube and fin banks, closed form analytical modal analysis is impossible and hence a design engineer often resorts to conducting finite element based numerical modal analysis. This approach is not always feasible, since a full scale FE model is often computationally very expensive because there can be a few hundred to a few thousand coupled tubes and fins in a typical heat exchanger. The corresponding discretised structural models may involve thousands or millions of degrees-of-freedom, leading to a similar number of equations of motion to be solved. The problem is further aggravated when the design alternatives to be evaluated are large. This is when numerous combinations of geometric or material parameters of the structure need to be considered, while exploring a multi-dimensional design space. This difficulty is often referred to as the *curse of dimensionality*. Therefore, a detailed FE model cannot be used for iterative design changes or parametric study.

A computationally inexpensive reduced order model which captures the essential dynamics of the system for lower vibrational modes is useful, especially at early stages of design search, when accuracy of results is not paramount. Lower modes of vibration are associated with standing waves of long wavelength. For wavelength much longer than the spacing of fins, a complex tube-fin assembly can be modelled as an effective medium. Such a model would also economically provide insights into the effects of various design parameters and components which FE would be unable to provide without a multi-parametric study which would be computationally expensive. A model applicable for low frequency (or equivalently long wavelength) inspired by this need is developed here. The repetitive nature of the structural geometry within heat exchangers, regularly spaced tube and fins, are great candidates to be modelled using "homogenised" analogues which nonetheless capture the dynamic behaviour of interest. Typically, lower vibrational modes are of interest in heat exchangers.

From initial numerical experiments, two different "types" of lower vibrational modes were observed in tube-and-fin banks. Broadly, these pertain to the motion of the entire tube-and-fin bank as an effective "beam in flexure" or a "rod in torsion", depending on the mode. Energy expressions are constructed using this effective beam or shaft approximation to obtain the Rayleigh quotient based estimate of modal frequencies.

Two different types of lattice arrangements of tubes are considered - rectangular and irregular hexagonal. The rectangular lattice arrangement of tubes allows for a detailed study of the energy contributions. For such cases, we restrict ourselves to studying the "beam in flexure" type modes. However, detailed investigation is carried out to explicate the subtle contribution of the flexure of fins. Next, irregular hexagonal arrangement of tubes is considered; this is the configuration usually employed in industry. Given the more complex nature of the configuration, we provide only an elementary way to include the subtle effect of fin flexure. However, for this configuration, computationally efficient models of both "beam in flexure" and "rod in torsion" type modes is developed.

5.1 Bending modes of a tube-fin assembly grouped on a rectangular lattice

The low frequency vibrational modes of the of a tube and fin bank with tubes in a rectangular configuration (see Figure 5.2) are predominantly those in which all tubes have broadly the same transverse deflection; they will be called cooperative modes from here on (see Figure 5.3). Note that we consider the mode corresponding to the transverse vibration of the tubes along one of the principal directions of the rectangular lattice. If the vibrational modes in which the tubes execute displacements along another direction are desired, the inter-tube distances (b & d_w) can simply be interchanged; the rest of the analysis remains unchanged. A few simplifying assumptions, which will enable the use of a Rayleigh quotient approximation to estimate modal frequencies, are made. All tubes are assumed to have the same transverse deflection shape at some time instant t, $\Psi(x,t)$. Since, we are interested in

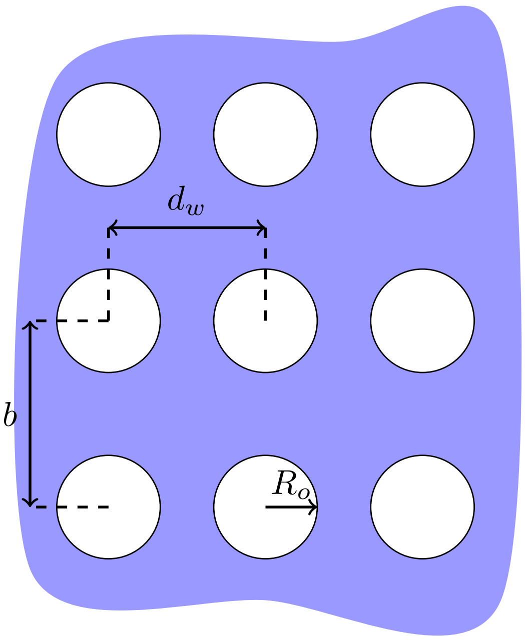

FIGURE 5.2: Tube in a rectangular lattice arrangement on the fins. Outer diameter of the tubes (R_o) is marked and so are the inter-tube distances (b and d_w). The inter-tube distance in the direction of transverse displacement of the tubes is b.

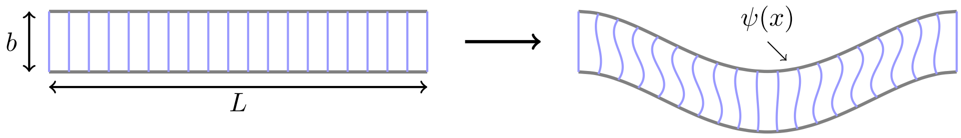

FIGURE 5.3: Deformation of tube (grey) + fin (blue) system at a lower vibrational mode for an illustrative case. Note that all the tubes have the same transverse deflection. This shape may be called $\psi(x)$.

modal vibrations, we can set $\Psi(x,t) = \psi(x)\cos(\omega t)$ where $\psi(x)$ describes the shape of the tubes which underdoes temporal sinusoidal modulation of angular frequency ω. Axial displacements are assumed to be small in both tubes and fins. Tubes are assumed to be much stiffer than fins in bending. Also in bending the fins are modelled as beams. Fins, are more accurately modelled as plates, as is the case in the FE simulations presented below. However, given the displacements they undergo in the specific case under consideration, modelling them as beams suffices.

5.1.1 Discrete Model

Consider two identical tubes with inner and outer radii of $R_\mathrm{i}, R_\mathrm{o}$ resp. and made of a material with Young's modulus E_T, material density ρ_T (see Figure 5.3 for schematic). They are parallel and let their longitudinal axes be separated by distance b. Assume that they are coupled to each other by N_F identical fins with thickness t_F and that the

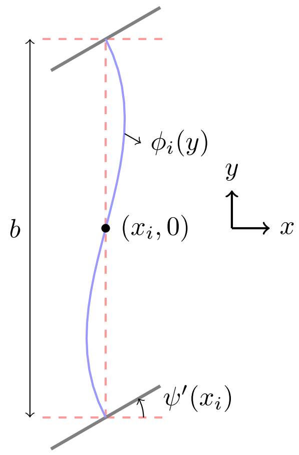

FIGURE 5.4: The deformed shape of the fins (blue) can be written in terms of the deformed shape of the tubes (grey). Red dashed lines show the undeformed shape.

fins are made of a material with Young's modulus E_{F} and material density ρ_{F}. These fins are attached to the tubes at regular intervals along their length.

To develop the approximate model, we need to first derive an expression for the deflections of the fins. Let us focus on a single fin, say the i^{th} one, which has the position x_{i} along the x axis (see Figure 5.4). The origin is on the left end of the tubes and equidistant from the longitudinal axes of the two tubes and the x axis is parallel to the tube length, oriented towards the right. Since the shape of deflection of the tubes is known ($\psi(x)$), the deflection of each fin $\Phi_i(y,t) = \phi_i(y)\cos(\omega t)$ where the shape $\phi_i(y)$ (see Figure 5.4) can be written in closed form as

$$\phi_i(y) = \frac{\psi'(x_i)b}{4}\left(\frac{y}{b/2} - \frac{y^3}{(b/2)^3}\right). \tag{5.1}$$

Using this we may write the kinetic ($T(t)$) and the potential ($U(t)$) energy terms for tubes (subscript T) and fins (subscript F) as follows:

$$\begin{aligned}
U_{\mathrm{T}}(t) &= 2\frac{1}{2}\int_0^L E_{\mathrm{T}}I_{\mathrm{T}}\left(\partial_{xx}\Psi(x,t)\right)^2 \mathrm{d}x = \left[\int_0^L E_{\mathrm{T}}I_{\mathrm{T}}\psi''^2(x)\mathrm{d}x\right]\cos^2(\omega t),\\
T_{\mathrm{T}}(t) &= 2\frac{1}{2}\int_0^L \mu_{\mathrm{T}}\left(\partial_t\Psi(x,t)\right)^2 \mathrm{d}x = \omega^2\left[\int_0^L \mu_{\mathrm{T}}\psi^2(x)\mathrm{d}x\right]\sin^2(\omega t),\\
U_{\mathrm{F}}(t) &= \sum_{i=1}^{N_{\mathrm{F}}}\frac{1}{2}\int_{-b/2}^{b/2} E_{\mathrm{F}}I_{\mathrm{F}}\left(\partial_{yy}\Phi_i(y,t)\right)^2 \mathrm{d}y = \left[\sum_{i=1}^{N_{\mathrm{F}}}\frac{1}{2}\int_{-b/2}^{b/2} E_{\mathrm{F}}I_{\mathrm{F}}\phi_i''^2(y)\mathrm{d}y\right]\cos^2(\omega t),\\
T_{\mathrm{F}}(t) &= \sum_{i=1}^{N_{\mathrm{F}}}\frac{1}{2}\mu_{\mathrm{F}}b\left(\partial_t\Psi(x_i,t)\right)^2 = \omega^2\left[\sum_{i=1}^{N_{\mathrm{F}}}\frac{1}{2}\mu_{\mathrm{F}}b\psi^2(x_i)\right]\sin^2(\omega t),
\end{aligned} \tag{5.2}$$

where, $I_{\mathrm{T}} = \frac{\pi}{4}(R_o^4 - R_i^4)$, $I_{\mathrm{F}} = d_w t_{\mathrm{F}}^3/12$, $\mu_{\mathrm{T}} = \rho_{\mathrm{T}}\pi(R_o^2 - R_i^2)$, $\mu_{\mathrm{F}} = \rho_{\mathrm{F}}t_{\mathrm{F}}(d_w b - \pi R_o^2)$ and the prime symbol ($'$) denotes differentiation. Note that rotational inertia of the fins and of the tube cross sections is ignored in the energy expressions. The distributed

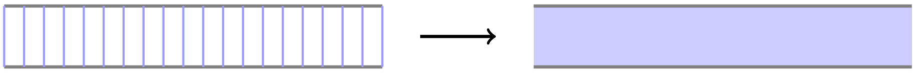

FIGURE 5.5: For typical lower modes of the tube-fin bank, the effect of the fins can be modelled as an equivalent soft shear core

interface between the tubes and fins is also assumed to be a single point (except in calculating μ_{F}).

The maximum potential and kinetic energies can be written, like in chapter 4, from the expressions above by simply dropping the squared sinusoidal terms. There, the angular modal frequency estimate can be written in terms of maximum potential and kinematic energies using the Rayleigh quotient as

$$\omega^2 = \frac{\left[\int_0^L E_{\mathrm{T}} I_{\mathrm{T}} \psi''^2(x) \mathrm{d}x\right] + \left[\sum_{i=1}^{N_{\mathrm{F}}} \frac{1}{2} \int_{-b/2}^{b/2} E_{\mathrm{F}} I_{\mathrm{F}} \phi_i''^2(y) \mathrm{d}y\right]}{\left[\int_0^L \mu_{\mathrm{T}} \psi^2(x) \mathrm{d}x\right] + \left[\sum_{i=1}^{N_{\mathrm{F}}} \frac{1}{2} \mu_{\mathrm{F}} b \psi^2(x_i)\right]}. \tag{5.3}$$

The mode shapes of a beam (with suitable boundary condition) as $\psi(x)$ can be reliably used. Then, $\phi(y)$ can be derived once $\psi(x)$ is set using Equation 5.1. Note that the evaluation of the potential and kinetic energy terms of the fins requires evaluation of N_{F} terms. Hence, the computational complexity of finding the frequency estimate scales linearly with the number of fins.

5.1.2 Smeared Model

With all the aforementioned assumptions, and plots of mode shapes (see Figure 5.3) one can see that when the distance between tubes is much smaller than their length (which is most often the case), the fins act almost like a soft core (see Figure 5.5) offering resistance to shear akin to sandwich beams [159]. The effective shear modulus due to the presence of this "apparent soft core" can be estimated. As we did previously, we shall focus on the deflection of a single fin to develop the model (see Figure 5.6). In this case, we shall first derive the effective shear modulus of the apparent soft core. Assume that the bottom tube is held fixed and a static force F parallel to the length of the tubes is applied to the end of the top tube. Assume that the separation between the tubes is b and the tubes are L_{UC} long.

In light of aforementioned assumptions we can write the shape of the deformed fin in terms of the resultant displacement at the end (say δ) and the length of the fins (b) as

$$\phi(y) = \delta \left(\frac{3}{b^2} y^2 - \frac{2}{b^3} y^3 \right). \tag{5.4}$$

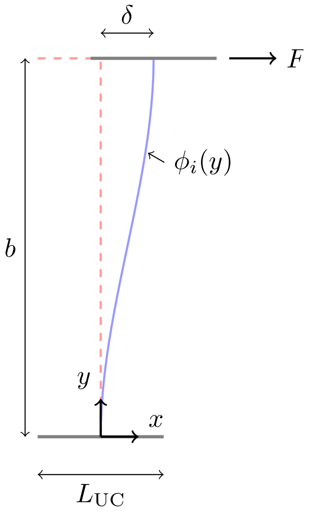

FIGURE 5.6: Deflection of a unit cell to a shearing force. This is used to find the shear modulus of the equivalent soft shear core material.

The force in terms of the displacement the bending stiffness of the fin (modelled as a beam) and δ is

$$F = -E_{\mathrm{F}} I_{\mathrm{F}} \phi'''(b) = \frac{12 E_{\mathrm{F}} I_{\mathrm{F}} \delta}{b^3}. \tag{5.5}$$

Hence, the effective shear modulus of this "apparent soft core" is,

$$G = \frac{F/A}{\delta/b} = \frac{12 E_{\mathrm{F}} I_{\mathrm{F}}}{A b^2} = \frac{12 E_{\mathrm{F}} I_{\mathrm{F}}}{L_{\mathrm{UC}} d_w b^2}. \tag{5.6}$$

For a 2 tube + N_{F} fin bank, G can be updated by simply setting,

$$L_{\mathrm{UC}} = \frac{L}{N_{\mathrm{F}} + 1}. \tag{5.7}$$

This effective shear modulus can be used to write an approximate expression for the potential energy due to fins (assuming that they constitute a soft core with shear modulus G) as,

$$U_{\mathrm{F}}(t) = \left[\frac{1}{2}\int_0^L G(b d_{\mathrm{w}}) \psi'^2(x) \mathrm{d}x\right] \cos^2(\omega t) = \frac{1}{2}\frac{12 E_{\mathrm{F}} I_{\mathrm{F}}}{b L_{\mathrm{UC}}} \int_0^L \psi'^2(x) \mathrm{d}x. \tag{5.8}$$

Finally, when $L_{\mathrm{UC}} << L$ the summation involving fin location can be approximated by an integral as

$$T_{\mathrm{F}}(t) = \omega^2 \left[\frac{1}{2}\mu_{\mathrm{F}} b \sum_{i=1}^{N_{\mathrm{F}}} \psi^2(x_i)\right] \sin^2(\omega t) \approx \omega^2 \left[\frac{1}{2}\frac{\mu_{\mathrm{F}} b}{L_{\mathrm{UC}}} \int_0^L \psi^2(x) \mathrm{d}x\right] \sin^2(\omega t). \tag{5.9}$$

It can be seen that through the aforementioned approximation the computational complexity of the evaluation of energy terms for the fins does not scale with the number of fins. Hence, this method yields a good estimate for the lower modal

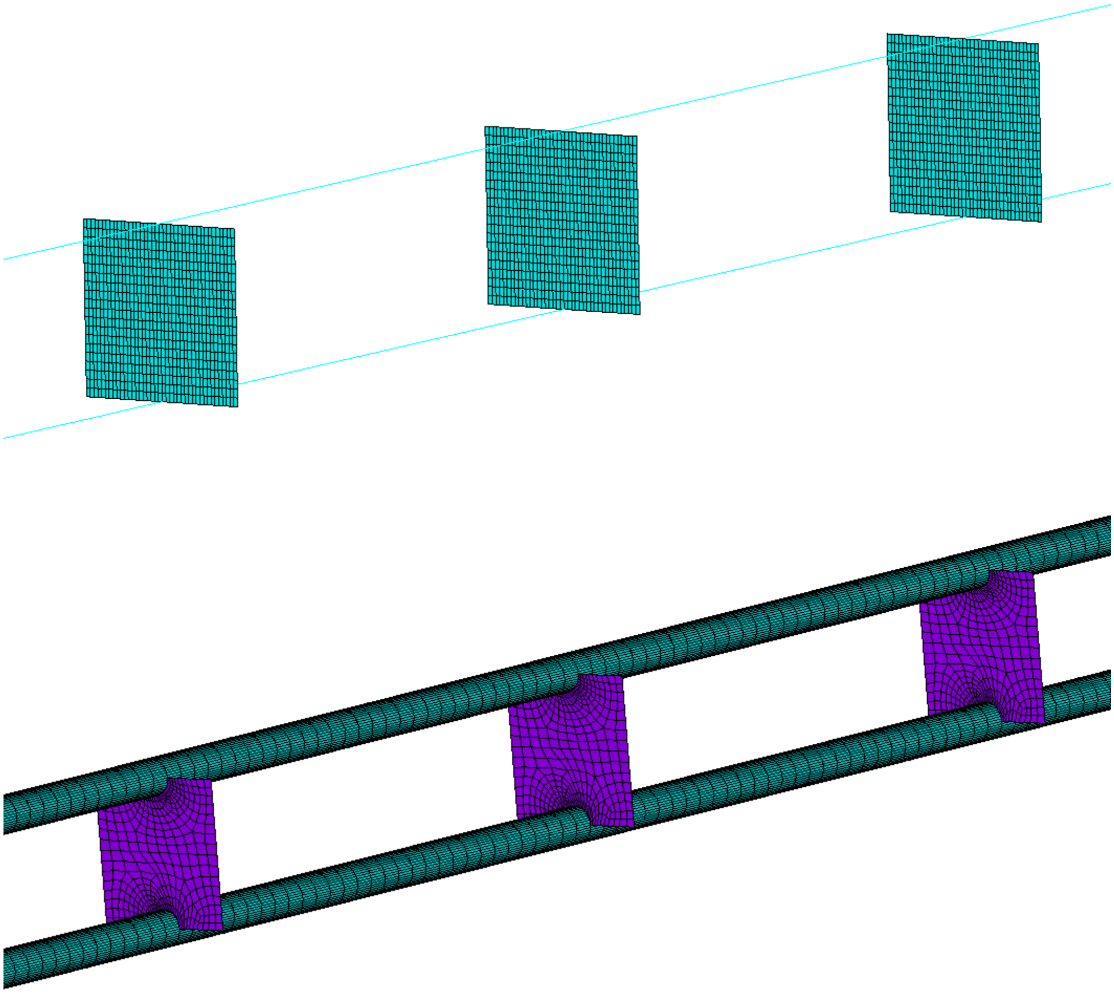

FIGURE 5.7: ANSYS Shell Beam (top): The tubes are modelled as beam elements and the fins are modelled with shell elements. ANSYS Shell (bottom): The tube and fins are both modelled with shell elements.

frequencies of the tube and fin bank at very low computational expense.

A Rayleigh quotient approach can now be applied to get an estimate of the modal frequencies.

5.1.3 Comparison of the methods

The performance of different methods for estimating modal frequencies of the tube and fin bank is summarised in Table 5.1. Here, N_{F} and N_{T} stand for number of fin and tube respectively. Here, the modes in which all the tubes have the same transverse deflection are called ”cooperative” modes. It must be noted that the computational effort required to estimate the modal frequency does not scale with the number of fins of number of fins or tubes in the smeared model. Also, the smeared method is the same as the discrete model in the limiting case of $N_{\mathrm{F}} \to \infty$. Hence, for the smeared model there is actually a case where the method becomes *more* accurate as the number

	FE	**Discrete**	**Smeared**
Method Accuracy	Highest	Intermediate	Lowest
N_{F} Scaling	$\sim \mathcal{O}(N_{\mathrm{F}}^{2.373})$[160]	$\sim \mathcal{O}(N_{\mathrm{F}})$	$\sim \mathcal{O}(1)$
N_{T} Scaling	$\sim \mathcal{O}(N_{\mathrm{T}}^{2.373})$[160]	$\sim \mathcal{O}(1)$	$\sim \mathcal{O}(1)$
Available Modes	All	Cooperative	Cooperative

TABLE 5.1: Summary of the performance of FE, discrete model and smeared model at modal frequency estimation.

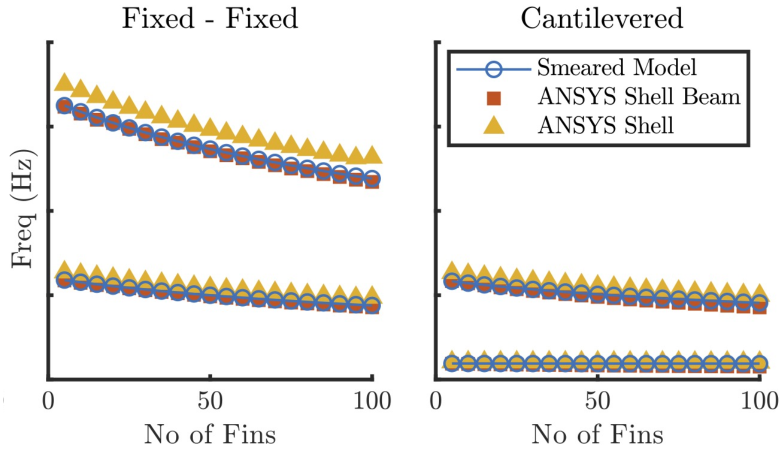

FIGURE 5.8: Comparison of modal frequency estimates of tube and fin bank in fixed-fixed (left) and cantilevered (right) boundary conditions using the presented model and two different FE simulations.

of fins increases while the computational effort required *does not change* with increasing number of fins at all!

5.1.4 Comparison with ANSYS FE predictions

The modal frequency estimates obtained from the smeared model were compared with those from a commercial FE simulation software, ANSYS [118]. There are numerous approaches one can take when modelling a tube and fin bank on ANSYS. Two of them are covered below. The first is to model the tubes as beams and the fins as shells (see Figure 5.7, top). In this case the interface between the tube and fin is a point. This is imposed due to the use of beam elements to model the tubes. Another approach is to model both the tube and fins as shell elements. This allows a more realistic modelling of the tube and fin bank including a finite curved edge being the interface of the tube and fins (see Figure 5.7, bottom). However, this also increases the computational cost involved. It can be seen from Figure 5.8 that the presented model predicts the modal frequencies quite well.

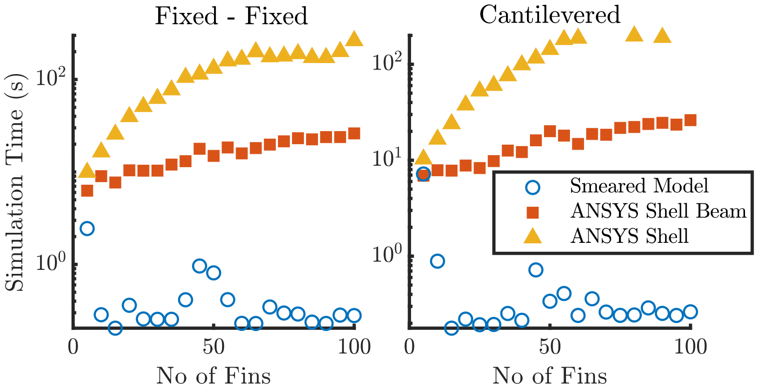

FIGURE 5.9: Comparison of computation time for modal frequency of tube and fin bank in fixed-fixed (left) and cantilevered (right) boundary conditions using the presented model and two different FE simulations. Note that the y-axis in both plots has a log scaling.

It can be seen, in Figure 5.9, from the comparison of computation time of modal frequency estimates that the ANSYS FE simulations are computationally very expensive compared to the smeared model. It is also to be noted that the computation time for the smeared model does not monotonically increase with number of fins. Note that log scaling exaggerates the variations in smaller values. Also, since the computation time reported here is for a single run, the time does not increase monotonically with number of fins as expected for the two ANSYS methods. This is likely due to local CPU loads being different while running these simulations. Computation time averaged over numerous simulations is expected to display the scaling as suggested by Table 5.1.

5.2 Lower vibrational modes for tubes in a hexagonal lattice arrangement

A similar modeling approach can be taken to find lower vibrational modes of tube and fin banks when the tubes are not arranged in a rectangular lattice. Due to the relative complexity of deflection of fins when the tubes are arranged in a non rectangular lattice, one is unable to estimate the potential energy contributions due to flexure of fins in a straightforward manner. Hence, the frequency estimate of “beam in flexure” type modes is, in the present case, the same as that of a Euler beam bending with the added mass of the fins. As the number of tubes increases, a mode which resembles a “shaft in torsion” gets lower in frequency. This mode is also studied to obtain a Rayleigh quotient based modal frequency estimate. See Figure 5.10 for a plot of the the types of modes mentioned here. Only fixed-fixed boundary condition, which closest to the case encountered in industry, is considered here.

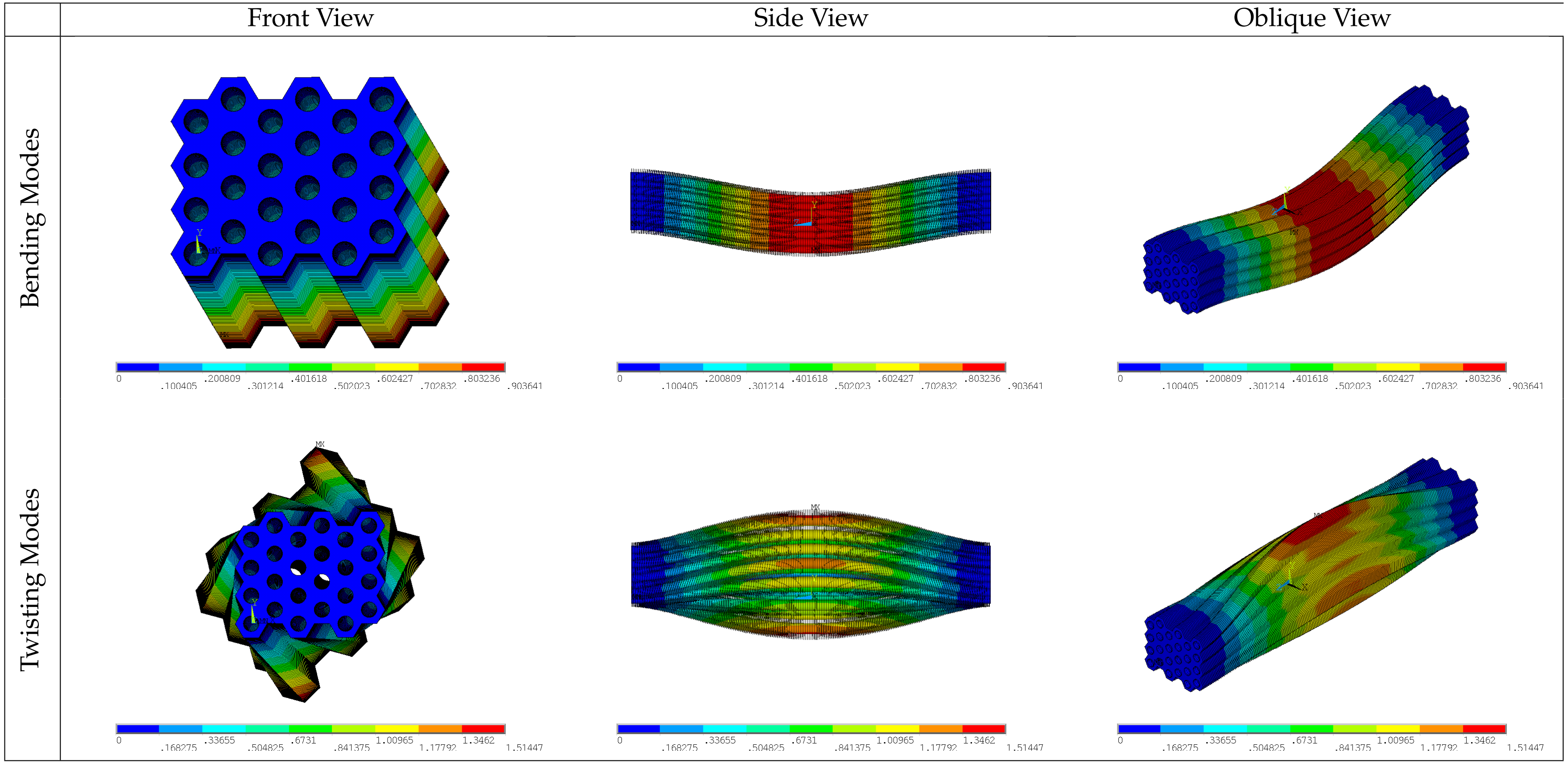
Front View
Side View
Oblique View
Bending Modes
Twisting Modes
0 .100405 .200809 .301214 .401618 .502023 .602427 .702832 .803236 .903641
0 .100405 .200809 .301214 .401618 .502023 .602427 .702832 .803236 .903641
0 .100405 .200809 .301214 .401618 .502023 .602427 .702832 .803236 .903641
0 .168275 .33655 .504825 .6731 .841375 1.00965 1.17792 1.3462 1.51447
0 .168275 .33655 .504825 .6731 .841375 1.00965 1.17792 1.3462 1.51447
0 .168275 .33655 .504825 .6731 .841375 1.00965 1.17792 1.3462 1.51447

FIGURE 5.10: Types of lower modes typically seen in fin and tube systems when the tubes are arranged in an irregular hexagonal lattice obtained using FEM simulations.

5.2.1 Bending type modes

Due to the complexity of general lattices over rectangular ones, one is unable to arrive at the contribution to the apparent shear due to flexure of fins. Hence, the bending modes can be approximated simply by Euler Bernoulli theory with additional mass due to the fins

$$f_{\mathrm{BM}} = \frac{1}{2\pi}\left((2n+1)\frac{\pi}{2}\right)^2\sqrt{\frac{(EI)_{\mathrm{tube}}}{ML^3}} \tag{5.10}$$

where $M = \rho_{\mathrm{T}} L\pi(R_o^4 - R_i^4) + N_{\mathrm{F}} A_{\mathrm{Unit}}$ and A_{Unit} is the area of one unit cell of a fin. In reality there would be two bending modes which are roughly (but not exactly) degenerate due to symmetry breaking in an irregular hexagon. The current work is unable to bring out that subtle difference in modal frequencies.

5.2.2 Twisting type modes

There is another kind of mode that appears when the tubes are in a hexagonal lattice arrangement. If one retains the idea of regarding the tube and fin bank as an effective continuum medium, these new modes are like torsional modes in a shaft. In this section, the energy expressions which are needed to construct a Rayleigh quotient based estimate of the modal frequencies are developed.

In this type of normal mode motion (see Figure 5.10), the fins effectively undergo rigid body rotations. Since, we are concerned with lower vibrational modes, we can assume that in-plane (membrane type) stresses in the fins will be negligible. This implies that in the plane of any fin, the transverse deflection of each of the tubes from its initial position is simply the product of the the angle of rotation of the fin about its own center of area/mass and the radial distance of the tube cross-section's center from the center of area/mass of the fin. Furthermore, the twist in each of the tubes at any location along the axis can be shown to be the same as the angle of rotation of the fin. Along the axial direction of the tubes, we can assume that they execute a motion described by some shape $\psi(x)$. Note that the shape of deflection of all the tubes will be identical up to a multiplicative factor; this is a consequence of assuming that the fins are only undergoing rigid body motions. Assume that the central fin (along the long axis) has the angular displacement $\Theta(t)$. Note that this fin can also be fictitious; we are only concerned about the motion at the middle of the axis. We can again use properties of rigid body rotations to write down the angular displacement in each of the fins in terms of $\Theta(t)$, $\psi(x)$ and axial locations of the fins $x_i, i = 1 \ldots N_{\mathrm{F}}$. The aforementioned properties of rigid body rotations allows, all relevant energy terms to be written in terms of one general coordinate, $\Theta(t)$. The energy terms are then used to construct and estimate the modal frequency using Rayleigh quotient.

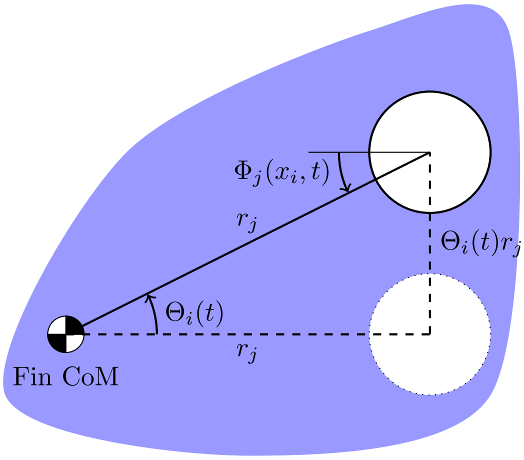

FIGURE 5.11: Rigid body rotation of fins in torsional modes. Properties of rigid body rotation allows description of tube deflection, tube twist and fin rotation by the single generalised coordinate θ.

Given the stated assumptions, fins are assumed to contribute only kinetic energy due to rotation. Meanwhile, the tubes contribute kinetic and potential energy due to transverse deflection. They also contribute potential energy due to the twist in their cross-sections. The kinetic energy due to the rotary inertia of the twisting tube cross-sections will be ignored since they will be negligibly small. The closeness of the fins in the axial direction will again be used to approximate summations along the axial length as integrals.

Assume that the central fin has an angular displacement of $\Theta(t)$ about the center of mass of the fin at time t. Since we are interested in modal vibrations, $\Theta(t)$ can be assumed to be a sinusoid of angular frequency ω and amplitude θ, .i.e. $\Theta(t) = \theta \cos(\omega t)$. By geometric compatibility and due to the absence of in-plane displacements in the fins, the deflected shape $\Psi_j(x,t)$ of the jth tube at time t is $\Psi_j(x,t) = r_j\Theta(t)\psi(x)$, where $\psi(x)$ is the shape of the transverse deflection of all the tubes and r_j is the distance of the center cross sectional area of the jth from the CoM of the fin.

Let the twist of the jth tube be given by $\Phi_j(x,t)$ at x position along the axis and time t and the angle of rotation of ith fin be $\Theta_i(t)$. Along the axial direction, the angular rotation of the fins will be modulated by the shape of deflection of the tubes. Hence, $\Theta_i(t) = \Theta(t)\psi(x_i)$. Furthermore, due to properties of rigid body rotations, at the location of fins the twist in the cross-section of tube will be the same as the angular displacement of the fin regardless of radial distance from CoM, i.e. $\Phi_j(x_i,t) = \Theta_i(t) = \Theta(t)\psi(x_i)$. Given the closeness of fins along the axis of the tubes, one can reasonable assume that the twist angle profile follows the shape $\phi(x)$. Using this assumption, we can write $\Phi_j(x,t) \approx \Theta(t)\psi(x)$.

The tube kinetic energy is the sum of contributions due to deflection of each tube where the jth tube deflects by $\Psi_j(x,t)$. Hence, the total kinetic energy in the tubes is

$$\sum_{j=1}^{N_\mathrm{T}} \frac{1}{2} \int_0^L \rho_\mathrm{T} A_\mathrm{T} (\partial_t \Psi_j(x,t))^2 \mathrm{d}x = \omega^2 \left[\frac{1}{2} \rho_\mathrm{T} A_\mathrm{T} R_\mathrm{sq} C_1 \theta^2\right] \sin^2(\omega t) \tag{5.11}$$

where $R_\mathrm{sq} = \sum_{j=1}^{N_\mathrm{T}} r_j^2, C_1 = \int_0^L \psi^2(x)\mathrm{d}x, A_\mathrm{T} = \pi(R_o^2 - R_i^2)$. The potential (strain) energy in the system due to flexure and twist of the tube. Considering them to be Euler Bernoulli beams the potential energy contribution due to flexure is

$$\sum_{j=1}^{N_\mathrm{T}} \frac{1}{2} \int_0^L E_\mathrm{T} I_\mathrm{T} (\partial_{xx} \Psi_j(x,t))^2 \mathrm{d}x = \left[\frac{1}{2} E_\mathrm{T} I_\mathrm{T} C_4 C_2 \theta^2\right] \cos^2(\omega t) \tag{5.12}$$

where $I_\mathrm{T} = \frac{\pi}{4}(R_o^4 - R_i^4), C_2 = \int_0^L \psi''^2(x)\mathrm{d}x$ and
$C_4 = \frac{1}{48} N_\mathrm{row} N_\mathrm{col} \left(4d_y^2\left(N_\mathrm{col}^2 - 1\right) + d_z^2\left(4N_\mathrm{row}^2 - 1\right)\right)$.

To write an expression for energy contribution due to twist of tubes, an expression for axial torque in the tubes is found to be $T_j(x,t) = G_\mathrm{T} J_\mathrm{T}(\partial_x \Phi_j(x,t))$ where G_T is the shear modulus of the tube material and J_T is the polar moment of area of the tube cross section. The axial torque profile turns out to be identical in all tubes regardless of position since they all rotate by the same angle. Therefore the potential energy contribution due to twist of tubes is

$$\sum_{j=1}^{N_\mathrm{T}} \frac{1}{2} \int_0^L \frac{T_j^2(x,t)}{G_\mathrm{T} J_\mathrm{T}} \mathrm{d}x = \left[\frac{1}{2} G_\mathrm{T} J_\mathrm{T} N_\mathrm{T} C_3 \theta^2\right] \cos^2(\omega t) \tag{5.13}$$

where $J_\mathrm{T} = \frac{\pi}{2}(R_o^4 - R_i^4), C_3 = \int_0^L \psi'^2(x)\mathrm{d}x$. Finally one may write the contribution from the rotation of the fins to the kinetic energy of the system as

$$\sum_{i=1}^{N_\mathrm{F}} \frac{1}{2} \rho_\mathrm{F} t_\mathrm{F} J_\mathrm{F} (\partial_t \Theta_i(t))^2 \approx \omega^2 \left[\frac{1}{2} \frac{\rho_\mathrm{F} t_\mathrm{F} J_\mathrm{F}}{L_\mathrm{UC}} C_1 \theta^2\right] \sin^2(\omega t) \tag{5.14}$$

where the polar moment of area of the fin $J_\mathrm{F} = N_\mathrm{F} J_\mathrm{Unit} + A_\mathrm{Unit} \sum_{j=1}^{N_\mathrm{T}} r_j^2$. Here, J_Unit and A_Unit are polar second moment of area and cross sectional area of one unit cell of the fin respectively. It is possible to write closed form expressions for these quantities in terms of lattice spacing but they vary with lattice type. Exact expressions for an irregular hexagonal lattice are computed using a custom script on a commercial symbolic computing software, Mathematica:

$$A_\mathrm{Unit} = d_y d_z - \pi R_o^2$$
$$J_\mathrm{Unit} = (3d_z^3 y_1 + 4d_z y_1^3 + d_z^3 y_2 + 4d_z y_1^2 y_2 + 4d_z y_1 y_2^2 + 4d_z y_2^3)/24 - \pi R_o^4/2$$

where,

$$y_1 = d_y/2 - d_z^2/(8d_y), \quad y_2 = d_y/2 + d_z^2/(8d_y).$$

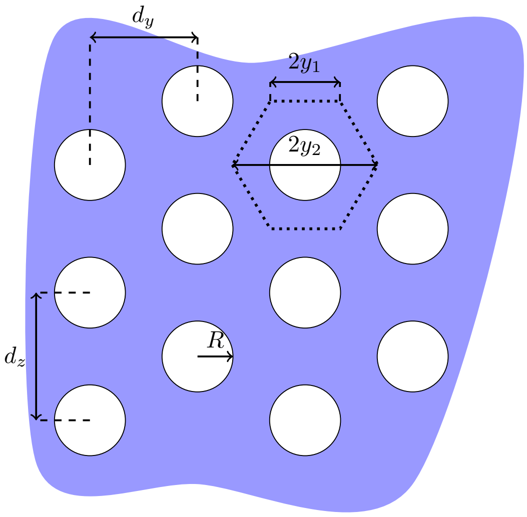

FIGURE 5.12: Geometrical parameters of a tube arrangement on fins. A unit cell of the hexagonal lattice is marked using dotted lines. Here, d_y and d_z dictate the spacing between the tubes and y_1 and y_2 are some relevant length scales of the uni cell which are used in calculating energy terms and can be written in terms of d_y and d_z.

Also an approximation ($\sum_{i=1}^{N_\mathrm{F}} \psi^2(x_i) \approx C_1/L_\mathrm{UC}$) premised on close spacing of the fins as compared to tube length is used, as used earlier. Finally, all the energy expressions can be written together and the Rayleigh quotient can be used to find estimates of the modal frequency.

$$f_\mathrm{TM} = \frac{1}{2\pi}\sqrt{\frac{\frac{1}{2}E_\mathrm{T}I_\mathrm{T}C_4C_2 + \frac{1}{2}G_\mathrm{T}J_\mathrm{T}N_\mathrm{T}C_3}{\frac{1}{2}\frac{\rho_\mathrm{F}t_\mathrm{F}J_\mathrm{F}}{L_\mathrm{UC}}C_1 + \frac{1}{2}\rho_\mathrm{T}A_\mathrm{T}C_4C_1}} \tag{5.15}$$

.

5.2.3 Finite element simulations

To test the validity of the model presented above, it is compared to finite element simulations of a tube and fin bank where the tubes are in an irregular hexagonal lattice arrangement. There simulations are carried out by modeling both the tube and fins using shell elements. The geometric parameters of the fin considered is shown in Figure 5.12.

The comparison of modal frequencies of bending type modes obtained from FE simulations and from the model are show in Figure 5.13. These are in excellent agreement which indicates that the effect of the strain energy contribution due to flexure of fins is small. This is expected to change if the fins become thicker. Similar comparison finite element simulations and the presented model for modal frequency estimate of the twisting mode are shown in Figure 5.14.

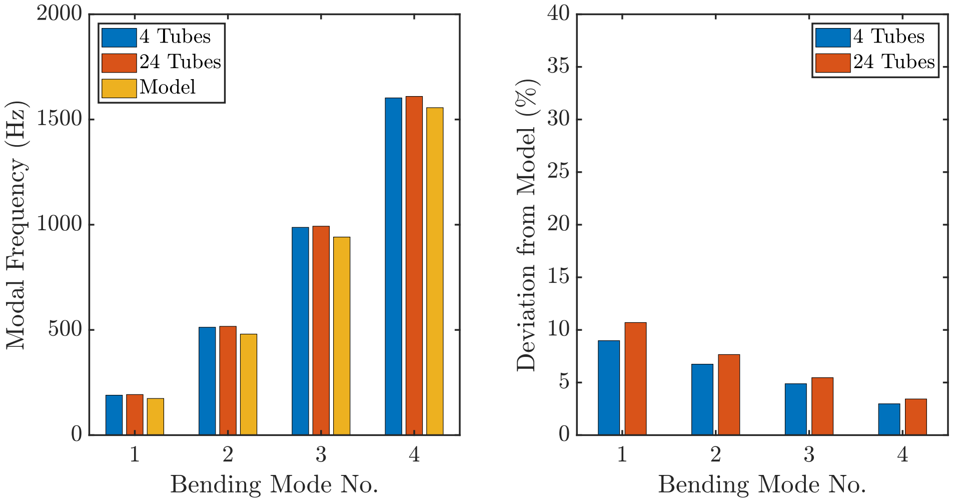

FIGURE 5.13: Comparison of bending mode frequencies estimates from presented model and finite element simulations simulations of a tube and fin bank with 4 or 24 tubes and 207 fins. We see that the presented model is within ∼ 10% of the estimates from FE.

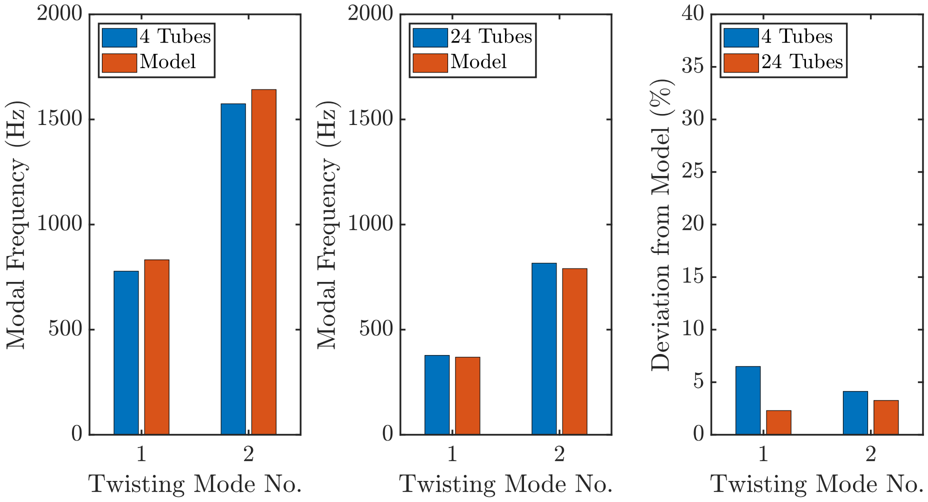

FIGURE 5.14: Comparison of twisting mode frequencies estimates from presented model and finite element simulations simulations of a tube and fin bank with 4 or 24 tubes and 207 fins. We see that the presented model is within ∼ 8% of the estimates from FE.

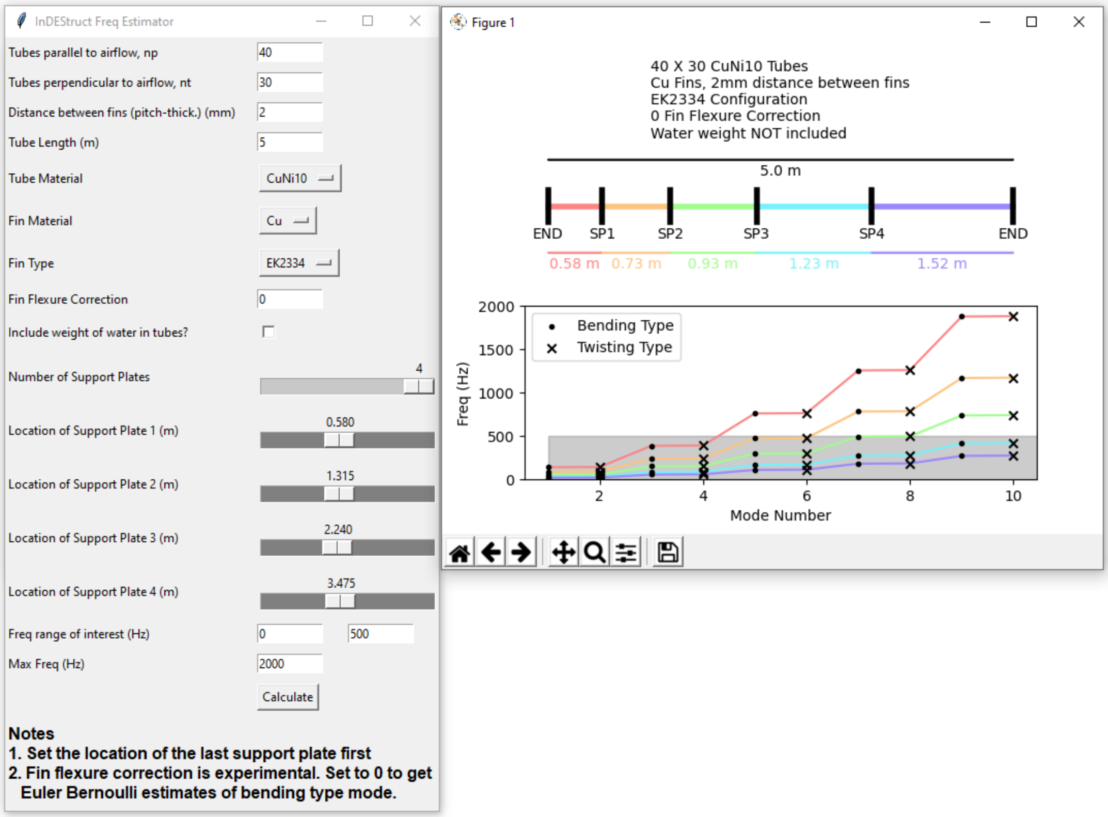
InDEStruct Freq Estimator
Figure 1
40 X 30 CuNi10 Tubes
Cu Fins, 2mm distance between fins
EK2334 Configuration
0 Fin Flexure Correction
Water weight NOT included
5.0 m
END
SP1
SP2
SP3
SP4
END
0.58 m
0.73 m
0.93 m
1.23 m
1.52 m
Bending Type
Twisting Type
Freq (Hz)
2000
1500
1000
500
0
2
4
6
8
10
Mode Number
Calculate

Tubes parallel to airflow, np: 40

Tubes perpendicular to airflow, nt: 30

Distance between fins (pitch-thick.) (mm): 2

Tube Length (m): 5

Tube Material: CuNi10

Fin Material: Cu

Fin Type: EK2334

Fin Flexure Correction: 0

Include weight of water in tubes? ☐

Number of Support Plates: 4

Location of Support Plate 1 (m): 0.580

Location of Support Plate 2 (m): 1.315

Location of Support Plate 3 (m): 2.240

Location of Support Plate 4 (m): 3.475

Freq range of interest (Hz): 0 500

Max Freq (Hz): 2000

Notes
1. Set the location of the last support plate first
2. Fin flexure correction is experimental. Set to 0 to get Euler Bernoulli estimates of bending type mode.

FIGURE 5.15: A screenshot of a Python based GUI for deployment of the presented model in industry. The GUI allows for selection of pre-set fin configurations and material combinations.

5.3 Conclusions

In this chapter, homogenisation techniques were presented to aid in modal analysis of components of a heat exchanger. Inspired by the nature of “cooperative” modes, which typify lower vibrational modes of a tube and fin bank, computationally efficient models were presented for modal analysis of such structures. It was shown that the presented reduced order models of tube & fin assemblies scale only linearly or not at all with an increase in the number of fins. When the tubes are arranged as a rectangular lattice on the fins, a sophisticated model which included the effect of flexure in fins was developed. When the tubes are arranged in a general (non-rectangular) lattice, the effect of fin flexure was not modelled but was shown to be small. To aid the use of the presented model in early design exploration phase in the industry, a Python based graphical user interface (see Figure 5.15) designed and validated. This GUI encodes the presented model with inbuilt sets of materials and geometric configuration.

Chapter 6

Conclusions and future work

In the first half of this work (Chapters 2 and 3), the existence of branched flows in waves supported by thin elastic structures is reported. While branched flows have been reported in other areas of physics this is the first observation of branched flows in the domain of elasticity. This has immediate applications in areas such as metrology and non-destructive testing.

However, the uncovering of this hitherto unknown scatting phenomenon in elasticity must be viewed in a broader light to truly appreciate the possibilities it offers. Perhaps it is helpful to consider the impact of the translation of another powerful idea from condensed matter physics to elasticity, namely periodic meta-materials.

Leveraging and transposing ideas such as Bloch-Floquet-based analysis [16] from condensed matter physics to mechanics has yielded ways to leverage spatial periodicity [107, 161, 162] to engineer the response of physical structures to waves and vibrations. Today, acoustic metamaterials [88] constitute a vibrant area of active research with numerous applications in industry [163, 164].

Similar possibilities exist with branched flows in elasticity. This is especially true if one considers recent advancements which combine spatial periodicity and branched flows [58, 59]. There are very early results suggesting that branched flows can form stable channels of electron flow and may offer paths of zero resistivity [58]. These ideas, transposed appropriately, would have numerous applications in developing efficient elastic waveguides.

In Chapter 4, the modal vibration of a pillared plate is considered. A Rayleigh quotient based model of the modal vibration is proposed and compared with FEM simulations. The observation of ”Chladni-like” patterns are reported in the tip displacements of the pillars. Pillared plates are of great interest as metamaterials [165] and as abstractions of industrial assemblies. The work presented here not only provides a simple model for study modal vibration of pillared plates but also can form the basis of further study e.g. to study mode localisation due to imperfections in the nominally identical pillars. Previous work has shed light on the role of imperfections in causing mode localisation of mechanical structures such as chain of pendula [166, 167], coupled beams [168] and bladed discs [155]. This suggests that mode localisation may be a relevant area of research in coupled tubes too since, these tubes, although manufactured to be nominally identical, would inevitably have imperfections.

Chapter 5 showed how computationally efficient analysis of modal vibration of another industrially relevant assembly i.e. fin-and-tube banks can be carried out. This was premised on an *ansatz* about the mode shape. The presented work, apart from being immediately useful in the early design stages of heat exchangers, can form the basis of further study. Immediate extensions include the study of the role of uncertainty in boundary conditions and design parameters due to manufacturing tolerances. The graphical user interface that packages the presented model also provides a platform for all future developments to be readily deployed on.

In summary, this work demonstrates why the study of the spatial variability of the dynamic response of structures remains as impactful and important as it was in the time of Ernst Chladni.

Appendix A

Details of FEM simulations

The results presented in chapter 2 and chapter 3 are predicated on more than 4000 FEM simulations each. These correspond to parametric sweeps over different values of $\langle h^2 \rangle$ (severity of randomness), L_c (correlation length), and λ (wavelength). For each combination of parameters, 80 simulations were carried to be able to confidently infer expected locations of the first caustic. Other standalone FEM simulations were also carried out for visualisation purposes. The large number of computationally expensive simulations that had to be run necessitated the use of High Performance Clusters (HPCs). Given that these simulations are numerous (> 4000), computationally intensive (20min-8hours on 64 cores) and produce large amounts of data (100s of gigabytes), some effort was made to automate as many steps as possible. In this chapter, this semi-automated "workflows" is described in brief.

The entire numerical analysis task can be broken down into the following sub-tasks:

- setting up folders for simulations with appropriate script files
- generating random thickness fields samples
- submitting simulation jobs to HPC queues
- extracting relevant data and deleting temporary files
- monitoring the progress of jobs
- extracting relevant data (mainly, Integrated Intensity; see Equation 2.15) and packaging for export from HPC to local machine
- running "one-off" simulations to produce data for visualisations

A BASH setup file (`setup.sh`) creates a folder with the following file-structure [1] for each parameter set:

---

[1] files have extensions, sub-folders do not

```
/
├── set1
│   ├── run_branch_loop1.sh
│   └── expInt.py
├── set2
│   ├── run_branch_loop2.sh
│   └── expInt.py
├── set3
│   ├── run_branch_loop3.sh
│   └── expInt.py
├── set4
│   ├── run_branch_loop4.sh
│   └── expInt.py
├── genFieldEtc.m
├── makeDLFile.sh
├── randFieldGen.m
├── fullSim.sh
└── runOneLoop.ans
```

Restrictions on the maximum time that can be requested for a single job on the IRIDIS[2] HPC necessitated the splitting up of 80 simulations in each parameter set to 4 jobs (8 jobs for small values of $\langle h^2 \rangle$). `set1`, `set2`, etc. are the sub-folders for these jobs.

To generate the random fields and to queue the jobs, the BASH file `fullSim.sh` is run manually. This script executes the `genFieldEtc.m` script on MATLAB which first creates 3 sub-folders: `AuxFiles` (to store auxiliary files), `Fields` (to store samples of the random thickness field) and `DataFiles` (to store integrated intensity data which is ultimately exported).

This script also calls the MATLAB function `randFieldGen.m` repeatedly to generate the 80 samples of the random thickness field of identical statistical properties. These are stored in the `Fields` sub-folder as CSV files. A list of parameters values is generated and stored as `params.ans` in `AuxFiles`. `zInp.csv`, a time-series data corresponding to the sharp pulse-like imposed displacement (Figure 2.9), is also generated and stored in `AuxFiles`. `fullSim.sh` then submits the 4 (or 8) jobs to the HPC by executing `run_branch_loop1.sh`, etc.

```
/
├── AuxFiles
│   ├── params.ans
│   └── zInp.csv
└── DataFiles
```

---

[2] IRIDIS is the University of Southampton's HPC

- `Fields`
  - `field1.csv`
  - `field2.csv`
  - `...`
  - `field80.csv`
- `set1`
  - `run_branch_loop1.sh`
  - `expInt.py`
- `set2`
  - `run_branch_loop2.sh`
  - `expInt.py`
- `set3`
  - `run_branch_loop3.sh`
  - `expInt.py`
- `set4`
  - `run_branch_loop4.sh`
  - `expInt.py`
- `genFieldEtc.m`
- `makeDLFile.sh`
- `randFieldGen.m`
- `fullSim.sh`
- `runOneLoop.ans`

The submitted job script (`run_loop_branch1.sh`, etc.) has a three main parts (which are performed repeatedly for different samples of the random thickness field):

- An ANSYS simulations script (`runOneLoop.ans`), written in APDL, is called. This loads the relevant parameters from `params.ans` and the applied displacement from `zInp.csv`. Also, one of the random thickness field files from `Fields` folder is loaded. Then, a transient elastodynamics simulation is run. This is the most computationally intensive step.
  The ANSYS program produces many temporary files. The time-dependent displacement fields are written onto a file with a `.out` extension. During the simulation corresponding to `field1.csv`, a file called `nodeLoc.txt` is also written to the `DataFiles` folder. This file stores the location of each node in the FEM mesh; nodes are indexed by a node number. The node numbers and locations remain the same for all the simulations in the same parameter set and hence node locations are extracted only once.

- A Python script (`expInt.py`) extracts the time dependent displacement information from the ANSYS `.out` file using the `pyansys` package. Then, these displacements are numerically integrated using the `numpy` package to calculate

the integrated intensity. This is finally written to the `DataFiles` folder as a CSV file (`integIntensity1.csv`, `integIntensity2.csv`, . . .).
Note that this entire step can also be carried out within ANSYS itself using MAPDL. However, MAPDL is much slower than Python at numerical integration and this is why, the integrated intensity data extraction step is carried out separately on Python.

- Finally, the temporary ANSYS files are deleted and the whole process is repeated for a different random thickness field sample. The current sample number is kept track of by a `loopNo.py` file.

When the jobs are running, this how a typical folder corresponding to a parameter set looks:

```
/
├── AuxFiles
│   ├── params.ans
│   └── zInp.csv
├── DataFiles
│   ├── integIntensity1.csv
│   ├── integIntensity2.csv
│   ├── integIntensity21.csv
│   ├── ...
│   └── nodeLoc.txt
├── Fields
│   ├── field1.csv
│   ├── field2.csv
│   ├── ...
│   └── field80.csv
├── set1
│   ├── run_branch_loop1.sh
│   ├── (Temporary ANSYS files)
│   ├── loopNo.py
│   └── expInt.py
├── set2
│   ├── run_branch_loop2.sh
│   ├── (Temporary ANSYS files)
│   ├── loopNo.py
│   └── expInt.py
└── set3
    ├── run_branch_loop3.sh
    ├── (Temporary ANSYS files)
    └── loopNo.py
```

    - `expInt.py`
- `set4`
  - `run_branch_loop4.sh`
  - (Temporary ANSYS files)
  - `loopNo.py`
  - `expInt.py`
- `genFieldEtc.m`
- `makeDLFile.sh`
- `randFieldGen.m`
- `fullSim.sh`
- `runOneLoop.ans`

Since, numerous jobs would be running at the same time on the HPC, a "dashboard" view of the simulation progress is desirable. The same was written in Python; progress was tracked by looking at the number of files written to the `DataFiles` folder. Figure A.1 shows a typical output of running this script.

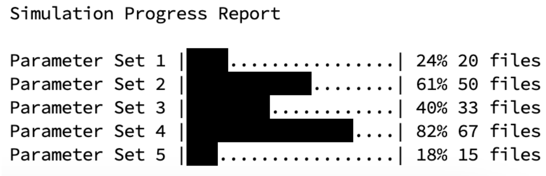

```
Simulation Progress Report

Parameter Set 1 |████................| 24% 20 files
Parameter Set 2 |████████████........| 61% 50 files
Parameter Set 3 |████████............| 40% 33 files
Parameter Set 4 |████████████████....| 82% 67 files
Parameter Set 5 |███.................| 18% 15 files
```

FIGURE A.1: A simple progress report is obtained by tracking the number of files in the `DataFiles` folders.

This bird's eye view of progress helped tremendously in keeping track of the simulations and in rectifying problems such as failed jobs. When, all the simulations were completed, the BASH script `makeDLFile.sh` was run manually. This compressed the contents of `DataFiles` into a `.zip` file for export to a local machine. Further processing to extract location of the first caustic was carried out on a local machine and so were the visualisations.

Appendix B

Tutorial: Application of Bloch's theorem in lattice vibrations

Originally developed in the area of solid state physics, a version of Bloch's theorem, relevant to the purposes of this discussion, can be stated as below[1]:

> In a periodic crystal with periodicity $\mathbf{R}$. Bloch waves $\psi(\mathbf{r})$ can be written in the form:
>
> $$\psi_{\mathbf{k}}(\mathbf{r}) = e^{i\mathbf{k}\cdot\mathbf{r}}u(\mathbf{r}), \tag{B.1}$$
>
> where $\mathbf{k}$ is the wavevector and $u(\mathbf{r})$ is a periodic function of periodicity $\mathbf{R}$.

Basically, due to the periodicity of lattice, the waves are identical on all lattice sites barring a phase modulation given by $e^{i\mathbf{k}\cdot\mathbf{r}}$. Consider the wave at $\mathbf{r}+\mathbf{R}$ with wave vector $\mathbf{k}$, then

$$\begin{aligned}\psi_{\mathbf{k}}(\mathbf{r}+\mathbf{R}) &= e^{i\mathbf{k}\cdot(\mathbf{r}+\mathbf{R})}u(\mathbf{r}+\mathbf{R}) && \text{(B.2)}\\ &= e^{i\mathbf{k}\cdot\mathbf{R}}e^{i\mathbf{k}\cdot\mathbf{r}}u(\mathbf{r}) && \text{(B.3)}\\ &= e^{i\mathbf{k}\cdot\mathbf{R}}\psi_{\mathbf{k}}(\mathbf{r}). && \text{(B.4)}\end{aligned}$$

This is an alternative statement of Bloch's theorem. Define $\mathbf{G}$ such that $\mathbf{G}\cdot\mathbf{R} = 2\pi N$, where N is an integer. Then if we insert $\mathbf{k} = \mathbf{k}' + \mathbf{G}$ in the above statement of Bloch's theorem, we get,

$$\begin{aligned}\psi_{\mathbf{k}}(\mathbf{r}+\mathbf{R}) &= e^{i(\mathbf{k}'+\mathbf{G}\cdot\mathbf{R})}\psi_{\mathbf{k}}(\mathbf{r}) && \text{(B.5)}\\ &= e^{i\mathbf{k}'\cdot\mathbf{R}}e^{i\mathbf{G}\cdot\mathbf{R}}\psi_{\mathbf{k}}(\mathbf{r}) && \text{(B.6)}\\ &= e^{i\mathbf{k}'\cdot\mathbf{R}}\psi_{\mathbf{k}}(\mathbf{r}). && \text{(B.7)}\end{aligned}$$

---

[1] This explanation borrows heavily from [16]

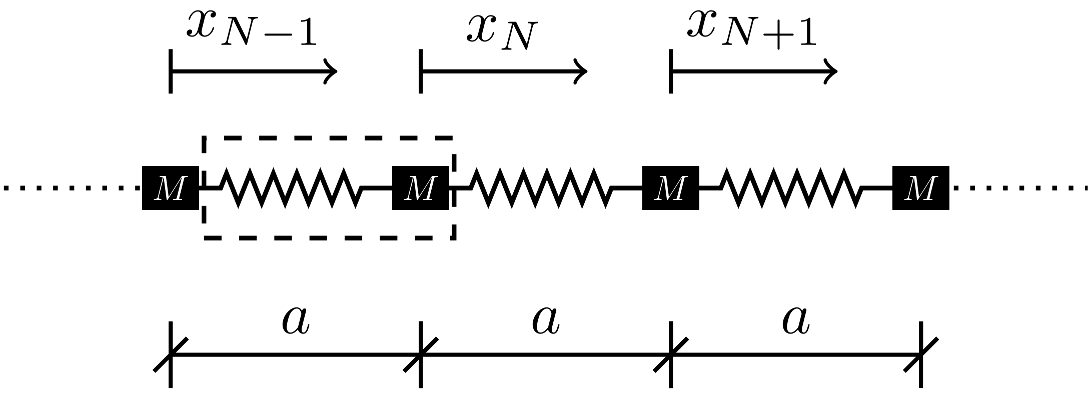

FIGURE B.1: Schematic of monatomic 1D crystal

Hence, $\psi_{\mathbf{k}}(\mathbf{r}) = \psi_{\mathbf{k}'}(\mathbf{r})$ as long as $\mathbf{k} = \mathbf{k}' + \mathbf{G}$.

B.1 1D Lattice

B.1.1 Monatomic Chain

We shall restrict ourselves to 1D problems in this section and next hence the wavevector, **k**, is simply the wavenumber, k. Waves with wave number k in 1D periodic media (with periodicity R) have the form $\psi(r) = e^{ikr}u(r)$ where $u(r)$ is a periodic function with period R. Furthermore wave solutions for wavenumbers $k + 2\pi N/R$ (where N is any integer) and wavenumber k are the same. Hence, dispersion curves are studied for $k \in [-\pi/R, \pi/R]$. This is called the first Brillouin Zone.

The crystal (see Figure B.1) has periodicity $R = a$, hence we need to study the dispersion relation for $k \in [-\pi/a, \pi/a]$. The equation of motion for mass at position N can be written as,

$$M\ddot{x}_N = -2Kx_N + Kx_{N+1} + Kx_{N-1}$$

Apply Bloch's theorem to obtain $x_{N+1} = e^{ika}x_N$, $x_{N-1} = e^{-ika}x_N$ and say $\tilde{\omega} = \omega/\omega_R$ where $\omega_R = \sqrt{K/M}$. Then the equation of motion reduces to,

$$(\tilde{\omega}^2 - 2 + e^{-ika} + e^{ika})x_N = 0.$$

For non trivial solution,

$$\begin{aligned} \tilde{\omega}^2 - 2 + e^{-ika} + e^{ika} &= 0 \\ \implies \tilde{\omega} = \sqrt{2 - 2\cos(ka)} &= 2|\sin(ka/2)| \end{aligned}$$

This yields the dispersion relation plotted in Figure B.2.

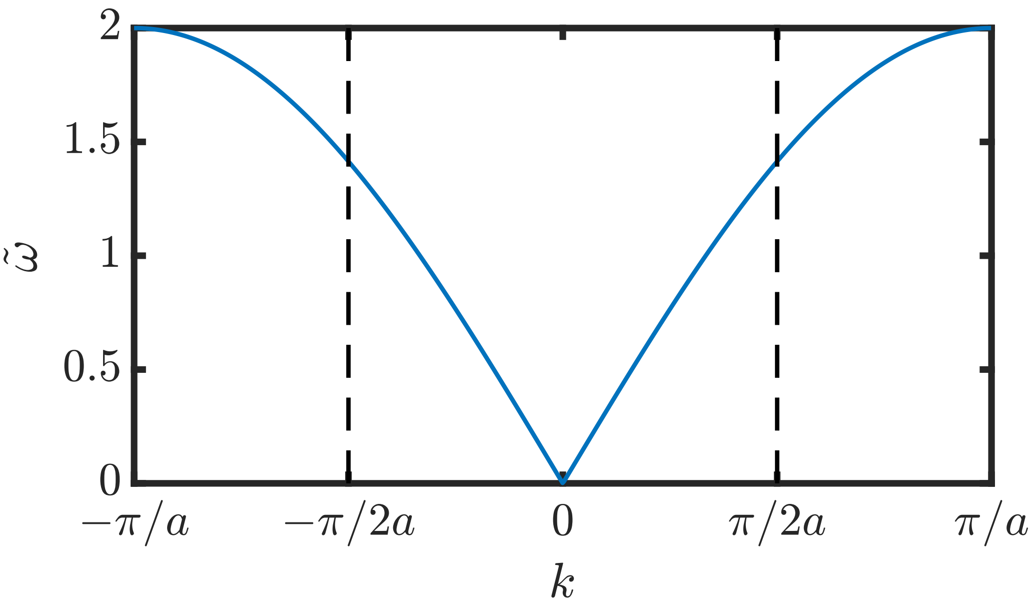

FIGURE B.2: Dispersion relation for a monatomic chain

B.1.2 Diatomic chain

The crystal (see Figure B.3) has periodicity $R = 2a$, hence we need to study the dispersion relation for $k \in [-\pi/2a, \pi/2a]$. The equations of motion for masses at position N can be written as,

$$M_1\ddot{x}_{1,N} = -2Kx_{1,N} + Kx_{2,N-1} + Kx_{2,N}$$

$$M_2\ddot{x}_{2,N} = -2Kx_{2,N} + Kx_{1,N} + Kx_{1,N+1}$$

Apply Bloch's theorem to obtain $x_{2,N-1} = e^{-2ika}x_{2,N},\ x_{1,N+1} = e^{2ika}x_{1,N}$ and say $\tilde{\omega} = \omega/\omega_R$ where $\omega_R = \sqrt{K/M_1}, \mu = M_2/M_1$. Then the equation of motion reduces to,

$$\begin{bmatrix} \tilde{\omega}^2 - 2 & 1 + e^{-2ika} \\ 1 + e^{2ika} & \mu\tilde{\omega}^2 - 2 \end{bmatrix} \begin{bmatrix} x_{1,N} \\ x_{2,N} \end{bmatrix} = 0.$$

For non-trivial solution,

$$\mu\tilde{\omega}^4 - 2(1+\mu)\tilde{\omega}^2 + 2 - 2\cos(2ka) = 0.$$

For different values of $k \in [-\pi/2a, \pi/2a]$, we will get a pair of admissible solutions ($\tilde{\omega}$ must be non-negative). Consider the dispersion relation obtained for $\mu = 1.5$. We can see from Figure B.4 that there is a span of frequencies for which there is no corresponding wave number (orange region). This is called the band gap. In reality, the wave number there is imaginary and hence corresponds to spatially decaying waves. This means that if the crystal is excited at a frequency within the stop band, no

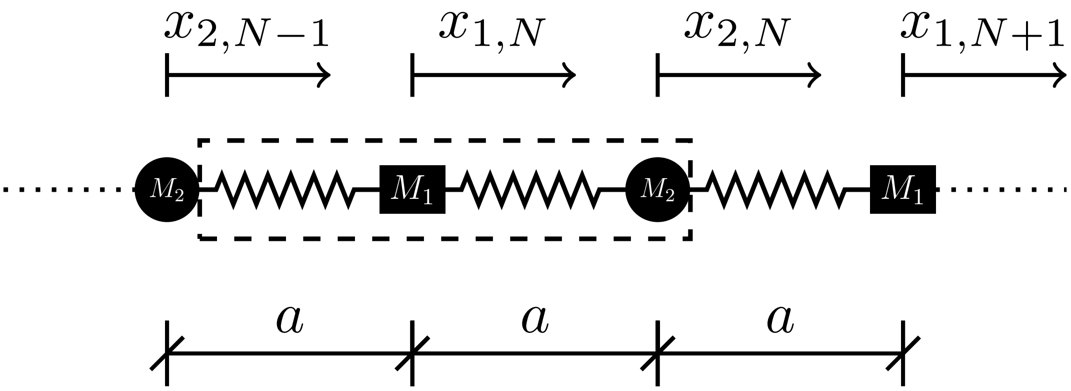

FIGURE B.3: Schematic of diatomic 1D crystal

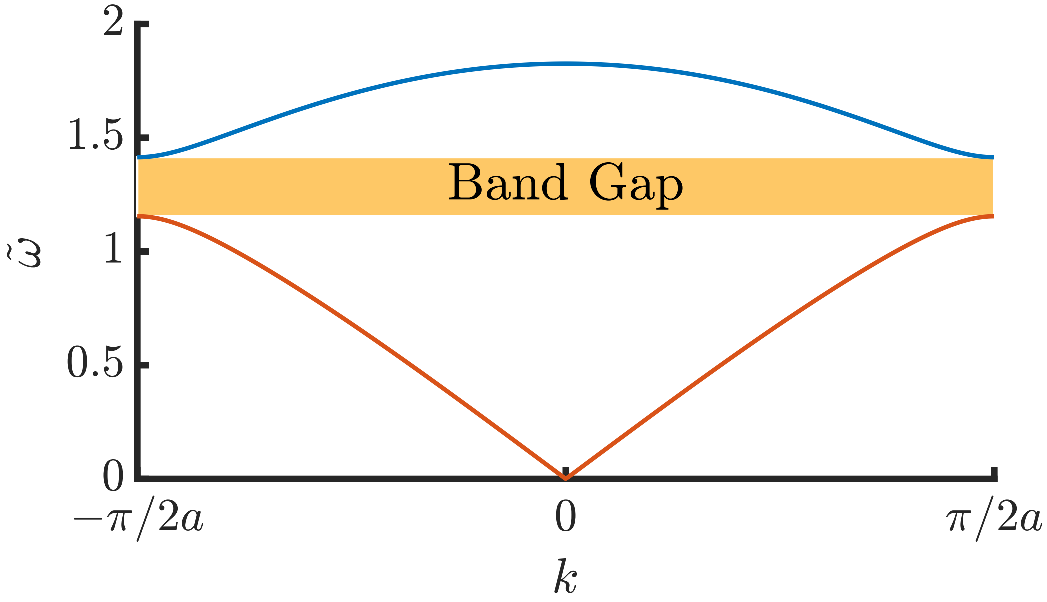

FIGURE B.4: Dispersion relation for a diatomic chain where the ratio of the masses, $\mu = 1.5$. The orange shaded region is called a band gap and no propagating waves exist in this frequency band.

waves will propagate and the excitation will die out exponentially from the point of excitation.

Monatomic chain as Diatomic chain

We can set $\mu = 1$ to obtain the dispersion curve for a monatomic chain using the formulation developed above for a diatomic chain. Note that unlike the earlier derivation for monatomic crystal the dispersion relation is plotted $k \in [-\pi/2a, \pi/2a]$ (Figure B.5). Figure B.5 is the same dispersion relation as the one in Figure B.2 except with the curves mirrored and "folded in" about the $k = \pm\pi/2a$ lines. In fact, Figure B.5 itself can be constructed by mirroring the curves in the region $k \in [0, \pi/2a]$

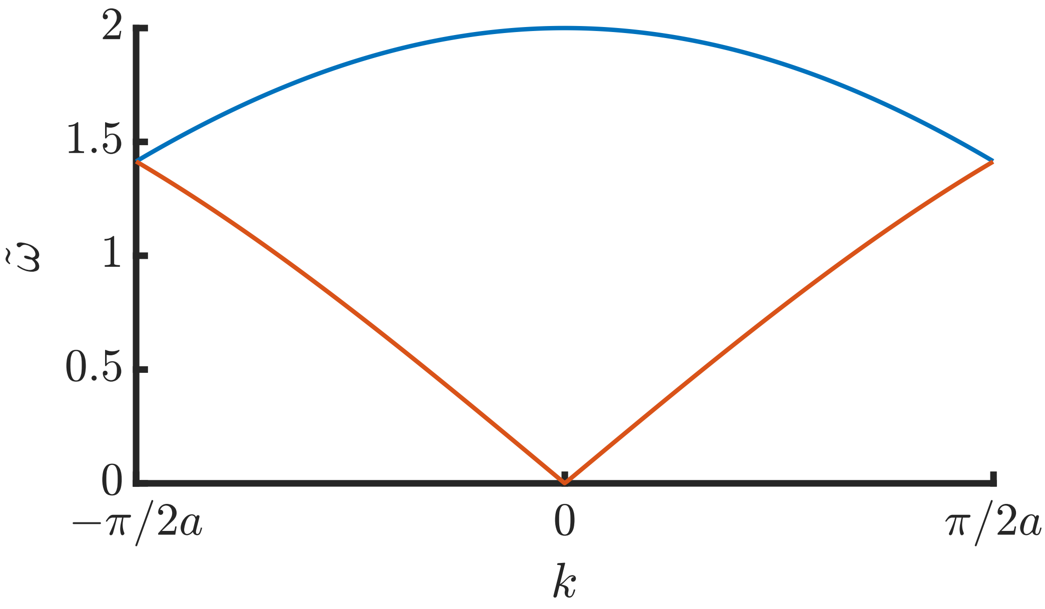

FIGURE B.5: Dispersion curve for a monatomic lattice formulated as a diatomic lattice.

about the $k = 0$ line. The region $k \in [0, \pi/2a]$ is called the irreducible Brillouin Zone (for this case, by reflection symmetry). The idea of irreducible Brillouin Zone become all the more important in the case of higher dimensional crystals where folding symmetries, similar to the one discussed above, reduce the wavevector space to be studied to understand the band structure of the said crystals.

B.2 2D Lattice

Monatomic crystal in centered square lattice configuration (see Figure B.6) is studied. With respect to a mass on the lattice, the location of the nearest and next-nearest neighbours is given by,

$$R_i = \begin{cases} L\left[\cos\left((i-1)\frac{\pi}{4}\right) \quad \sin\left((i-1)\frac{\pi}{4}\right)\right]^T, & i \in \{1,3,5,7\} \\ \sqrt{2}L\left[\cos\left((i-1)\frac{\pi}{4}\right) \quad \sin\left((i-1)\frac{\pi}{4}\right)\right]^T, & i \in \{2,4,6,8\}. \end{cases}$$

Let the spring constants be K_1^s (vertical and horizontal, red) K_2^s (diagonal, blue). Define,

$$K_i^s = \begin{cases} K_1^s, & i \in \{1,3,5,7\} \\ K_2^s, & i \in \{2,4,6,8\}. \end{cases}$$

We can write the equation of motion for the said mass as follows,

$$M\ddot{X} = \sum_{i=1}^{8} K_i^s \left((X_i - X) \cdot \hat{R}_i\right) \hat{R}_i.$$

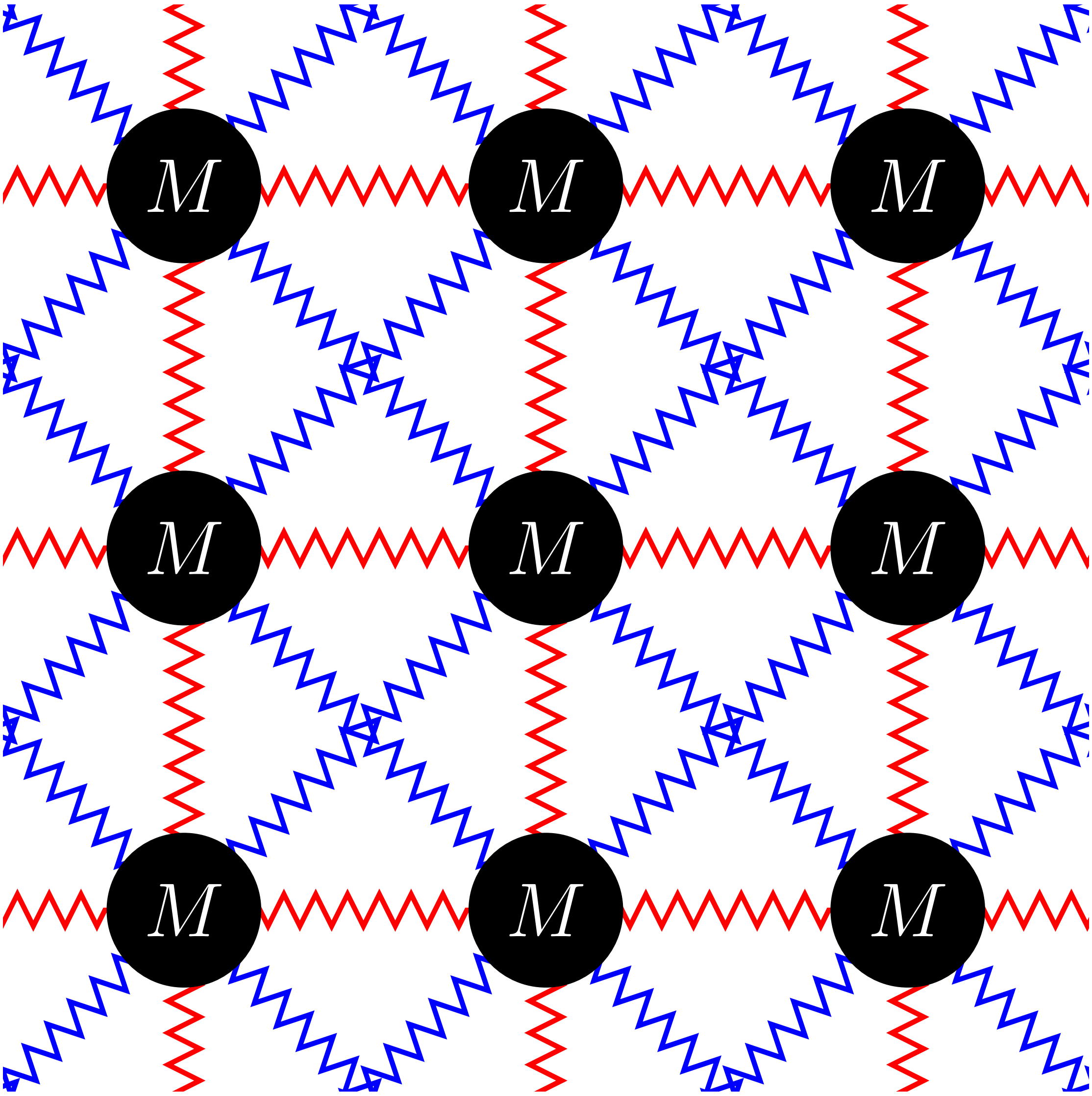

FIGURE B.6: Centered square lattice.

From application of Bloch's theorem we know that $X_i = Xe^{iK\cdot R_i}$ and use $M\ddot{X} = -M\omega^2 X$ and non-dimensionalise using $\tilde{\omega} = \omega/\sqrt{K_1^s/M}$, $K_2^s/K_1^s = \kappa$ to obtain,

$$\tilde{\omega}^2 + \sum_{i=1}^{8} \tilde{K}_i^s (e^{iK\cdot R_i} - 1)\left(X \cdot \hat{R}_i\right)\hat{R}_i = 0$$

where,

$$\tilde{K}_i^s = \begin{cases} 1, & i \in \{1,3,5,7\} \\ \kappa, & i \in \{2,4,6,8\}. \end{cases}$$

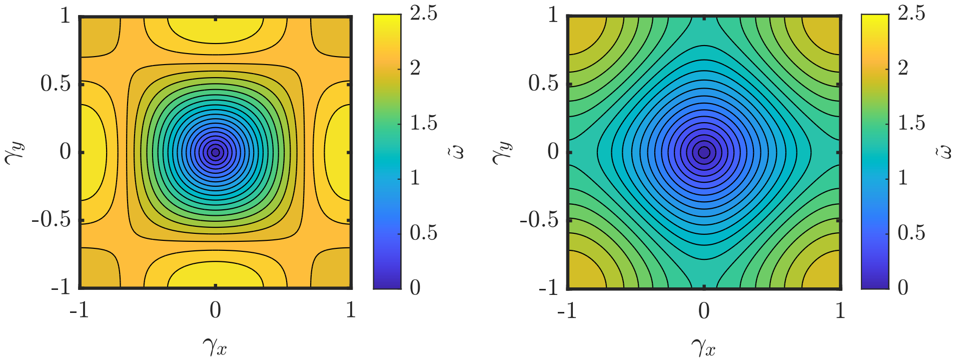

FIGURE B.7: The iso-frequency contours of the two branches of the solution of the characteristic equations. Notice that both branches have an 8 fold symmetry.

Substitute $X = [x\ y]^T, K = [k_x\ k_y]^T = \frac{\pi}{L}[\gamma_x\ \gamma_y]^T$ and rearrange into matrix form[2],

$$\begin{bmatrix} 2\cos(\pi\gamma_x)(\kappa\cos(\pi\gamma_y)+1) - 2\kappa + \tilde{\omega}^2 - 2 & -2\kappa\sin(\pi\gamma_x)\sin(\pi\gamma_y) \\ -2\kappa\sin(\pi\gamma_x)\sin(\pi\gamma_y) & 2\cos(\pi\gamma_y)(\kappa\cos(\pi\gamma_x)+1) - 2\kappa + \tilde{\omega}^2 - 2 \end{bmatrix} \begin{bmatrix} x \\ y \end{bmatrix} = 0.$$

For a non-trivial solution we require that the matrix on the LHS have a vanishing determinant. This yields,

$$(2\cos(\pi\gamma_x)(\kappa\cos(\pi\gamma_y)+1) - 2\kappa + \tilde{\omega}^2 - 2)(2\cos(\pi\gamma_y)(\kappa\cos(\pi\gamma_x)+1) - 2\kappa + \tilde{\omega}^2 - 2) \\ - (-2\kappa\sin(\pi\gamma_x)\sin(\pi\gamma_y))(-2\kappa\sin(\pi\gamma_x)\sin(\pi\gamma_y)) = 0.$$

This is the dispersion relation for the lattice of interest. Notice that while this is a quartic equation, it is quadratic in $\tilde{\omega}^2$ and hence can be solved in closed form. Since the lattice vectors are given by $L\,\hat{i},\ L\,\hat{j}$ the reciprocal lattice vectors are given by $(2\pi/L)\,\hat{j},\ (2\pi/L)\,\hat{i}$. Hence, the dispersion surface is to be plotted for the region $k_x \in [-\pi/L, \pi/L],\ k_y \in [-\pi/L, \pi/L]$. This corresponds to $\gamma_x \in [-1, 1],\ \gamma_y \in [-1, 1]$. For the purpose of illustration consider the case when $\kappa = 1/2$. The two admissible solutions of the characteristic equation are:

$$\tilde{\omega} = \sqrt{4 - \cos(\pi\gamma_y) - \cos(\pi\gamma_x)(1 + 2\cos(\pi\gamma_y))},$$
$$\tilde{\omega} = \sqrt{2 - \cos(\pi\gamma_x) - \cos(\pi\gamma_x)}.$$

Notice how the contour plots (see Figure B.7) of both branches of the frequency are 8-fold symmetric. This is can in fact be leveraged to simplify the representation of the dispersion relation. In the normalized wave vector space, $[\gamma_x\ \gamma_y]^T$, the triangular region which can be folded 8 times to regenerate the whole Brillouin zone is called the

---

[2] The intermediate steps are simple algebraic manipulations but they are tedious and hence have been skipped.

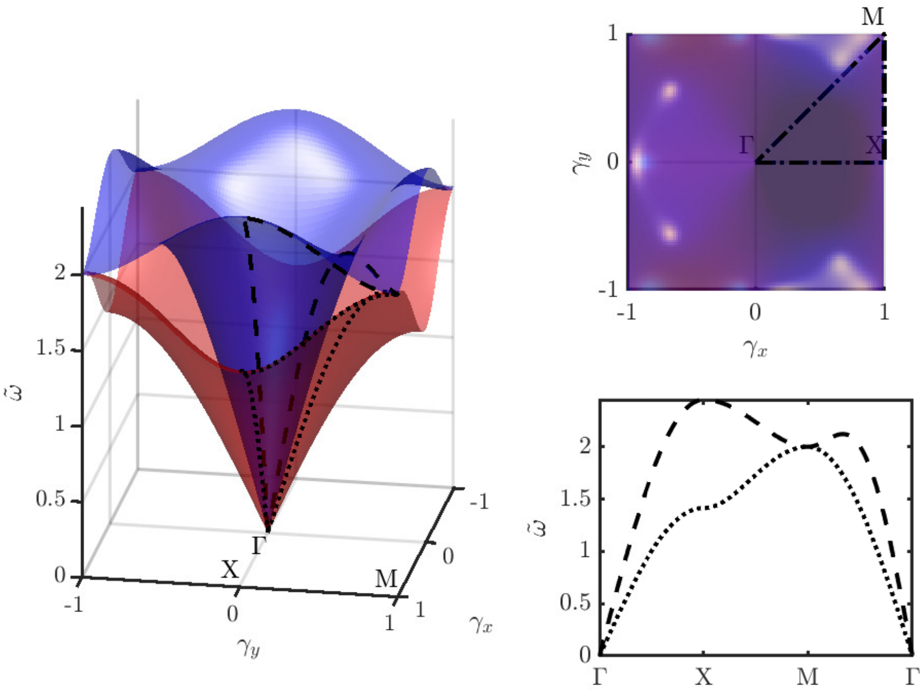

FIGURE B.8: (Left) The dispersion surface in 3D. (Right, top) Top view of the dispersion surface. (Right, bottom) Dispersion curve in the Irreducible Brillouin Zone

irreducible Brillouin zone. There are obviously eight different choices for such a region, we choose the one defined by ΓMXΓ where $\Gamma = [0\;0]^T$, $X = [1\;0]^T$, $M = [1\;1]^T$ (see Figure B.8, left). The results remain unchanged regardless of the choice of the irreducible Brillouin zone. For analysis of band gap we need to only be concerned about the maxima and minima of frequencies within the irreducible Brillouin zone. It is understood that in most cases these occur at the edges of the Brillouin zone[3]. Hence, we can have a 2D representation of the relevant (as far as stop and pass bands are concerned) portion of the dispersion relation by studying the frequencies along $\Gamma - X,\ X - M,\ M - \Gamma$ lines (see Figure B.8, right). It can be seen from the plot of the dispersion relation surface (see Figure B.8, left) how the 2D representation 'captures' the maximal and minimal frequency regions.

---

[3] There may be an intuitive way of looking at this: Since the dispersion surface has to be smooth everywhere, at least one of the components of the local gradient must vanish at the edges of the irreducible Brillouin zone. Otherwise with dispersion curve would have discontinuous changes in gradient at these edges, which would be non-physical. Since, the maxima and minima must occur at points where the gradient vanishes, it is reasonable to expect them at the edges of the irreducible Brillouin zone.

References

[1] NOAA: Natural Hazards Viewer. `https://www.ncei.noaa.gov/maps/hazards/`, 2023. Accessed: 2023-01-17.

[2] MA Topinka, BJ LeRoy, RM Westervelt, SEJ Shaw, R Fleischmann, EJ Heller, KD Maranowski, and AC Gossard. Coherent branched flow in a two-dimensional electron gas. *Nature*, 410(6825):183–186, 2001. URL `https://doi.org/10.1038/35065553`.

[3] AD Pierce. Waves on Fluid-Loaded Inhomogeneous Elastic Shells of Arbitrary Shape. *Journal of Vibration and Acoustics*, 115(4):384–390, 10 1993. ISSN 1048-9002. URL `https://doi.org/10.1115/1.2930361`.

[4] K Jose, N Ferguson, and A Bhaskar. Branched flows of flexural waves in non-uniform elastic plates. *Communications Physics*, 5(1), 2022. URL `https://www.nature.com/articles/s42005-022-00917-z`.

[5] K Jose, N Ferguson, and A Bhaskar. Branched flows of flexural elastic waves in non-uniform cylindrical shells. *PLoS ONE*, 18(5), 2023. URL `https://doi.org/10.1371/journal.pone.0286420`.

[6] RS Langley and NS Bardell. A review of current analysis capabilities applicable to the high frequency vibration prediction of aerospace structures. *Aeronautical Journal*, 102(1015):287–297, 1998. ISSN 0001-9240.

[7] SA Katifeoglou and LK Chatjigeorgiou. A shell-dynamics model for marine pipelines of large suspended length. *Ocean Systems Engineering*, 5(4):301–318, 2015. ISSN 2093-6702.

[8] J Yan, A Korobenko, X Deng, and Y Bazilevs. Computational free-surface fluid-structure interaction with application to floating offshore wind turbines. *Computers & Fluids*, 141(SI):155–174, 2016. ISSN 0045-7930.

[9] J Blachut and K Magnucki. Strength, stability, and optimization of pressure vessels: Review of selected problems. *Applied Mechanics Reviews*, 61(6), 2008. ISSN 0003-6900.

[10] D Afolabi. *Vibration of mistuned bladed disc assemblies*. PhD thesis, University of London, 1983. URL `https://www.imperial.ac.uk/media/imperial-college/research-centres-and-groups/dynamics/Afolabi-1982.pdf`.

[11] M Iqbal, A Kumar, M Murugan Jaya, and OS Bursi. Flexural band gaps and vibration control of a periodic railway track. *Scientific Reports*, 11(1):1–13, 2021. URL `https://www.nature.com/articles/s41598-021-97384-3`.

[12] M Oudich, N Gerard, Y Deng, and Y Jing. Tailoring structure-borne sound through bandgap engineering in phononic crystals and metamaterials: A comprehensive review. *Advanced Functional Materials*, 2022. ISSN 1616-301X. doi: 10.1002/adfm.202206309. URL `https://doi.org/10.1002/adfm.202206309`.

[13] RV Craster and S Guenneau. *Acoustic metamaterials: Negative refraction, imaging, lensing and cloaking*, volume 166. Springer Science & Business Media, 2012. URL `https://link.springer.com/book/10.1007/978-94-007-4813-2`.

[14] AN Norris. Acoustic cloaking. *Acoustics Today*, 11(1):38–46, 2015. URL `https://acousticstoday.org/acoustic-cloaking-andrew-n-norris-2/`.

[15] X Zhang and Z Liu. Negative refraction of acoustic waves in two-dimensional phononic crystals. *Applied Physics Letters*, 85(2):341–343, 2004. URL `https://doi.org/10.1063/1.1772854`.

[16] JD Joannopoulos, SG Johnson, JN Winn, and RD Meade. *Photonic Crystals: Molding the flow of light*. Princeton University Press, 2008. ISBN 9781400847129. URL `https://press.princeton.edu/books/ebook/9781400847129/photonic-crystals`.

[17] RV Craster, J Kaplunov, and J Postnova. High-frequency asymptotics, homogenisation and localisation for lattices. *The Quarterly Journal of Mechanics and Applied Mathematics*, 63(4):497–519, 2010.

[18] MB Amor and MHB Ghozlen. Lamb waves propagation in functionally graded piezoelectric materials by peano-series method. *Ultrasonics*, 55:10–14, 2015. URL `https://doi.org/10.1016/j.ultras.2014.08.020`.

[19] X Cao, F Jin, and I Jeon. Calculation of propagation properties of Lamb waves in a functionally graded material (fgm) plate by power series technique. *NDT & E International*, 44(1):84–92, 2011. URL `https://doi.org/10.1016/j.ndteint.2010.09.010`.

[20] SV Kuznetsov. Cauchy formalism for Lamb waves in functionally graded plates. *Journal of Vibration and Control*, 25(6):1227–1232, 2019. URL `https://doi.org/10.1177/1077546318815376`.

[21] P Pati and S Gupta. Modelling of love waves in a heterogeneous medium demarcated by functionally graded piezoelectric layer and size-dependent micropolar half-space. *Journal of Vibration Engineering & Technologies*, pages 1–22, 2021. URL `https://link.springer.com/article/10.1007/s42417-021-00330-w`.

[22] J Kaplunov, GA Rogerson, and PE Tovstik. Localized vibration in elastic structures with slowly varying thickness. *The Quarterly Journal of Mechanics and Applied Mathematics*, 58(4):645–664, 2005.

[23] PE Tovstik. Free high-frequency vibrations of anisotropic plates of variable thickness. *J. Appl. Math. Mech.*, 56:390–395, 1992.

[24] J Postnova and RV Craster. Trapped modes in 3d topographically varying plates. *IMA Journal of Applied Mathematics*, 73(6):950–963, 2008.

[25] J Postnova and Richard RV Craster. Trapped modes in topographically varying elastic waveguides. *Wave Motion*, 44(3):205–221, 2007.

[26] GH Loh, E Pei, D Harrison, and MD Monzón. An overview of functionally graded additive manufacturing. *Additive Manufacturing*, 23:34–44, 2018. URL `https://doi.org/10.1016/j.addma.2018.06.023`.

[27] S Gopalakrishnan. *Elastic wave propagation in structures and materials*. CRC Press, 2022. URL `https://doi.org/10.1201/9781003120568`.

[28] M Naebe and K Shirvanimoghaddam. Functionally graded materials: A review of fabrication and properties. *Applied materials today*, 5:223–245, 2016. URL `https://doi.org/10.1016/j.apmt.2016.10.001`.

[29] C Conlan-Smith, A Bhattacharyya, and KA James. Optimal design of compliant mechanisms using functionally graded materials. *Structural and Multidisciplinary Optimization*, 57(1):197–212, 2018. URL `https://link.springer.com/article/10.1007/s00158-017-1744-y`.

[30] A Sola, D Bellucci, and V Cannillo. Functionally graded materials for orthopedic applications–an update on design and manufacturing. *Biotechnology advances*, 34(5):504–531, 2016. URL `https://doi.org/10.1016/j.biotechadv.2015.12.013`.

[31] E Mueller, Č Drašar, J Schilz, and WA Kaysser. Functionally graded materials for sensor and energy applications. *Materials Science and Engineering: A*, 362(1-2): 17–39, 2003. URL `https://doi.org/10.1016/S0921-5093(03)00581-1`.

[32] WJ Parnell and PA Martin. Multiple scattering of flexural waves by random configurations of inclusions in thin plates. *Wave Motion*, 48(2):161–175, 2011. URL `https://doi.org/10.1016/j.wavemoti.2010.10.004`.

[33] CH Wang and F-K Chang. Scattering of plate waves by a cylindrical inhomogeneity. *Journal of Sound and Vibration*, 282(1-2):429–451, 2005. URL `https://doi.org/10.1016/j.jsv.2004.02.023`.

[34] VA Squire and TW Dixon. Scattering of flexural waves from a coated cylindrical anomaly in a thin plate. *Journal of Sound Vibration*, 236(2):367–373, 2000. URL `http://dx.doi.org/10.1006/jsvi.2000.2953`.

[35] PA Martin. *Multiple scattering: interaction of time-harmonic waves with N obstacles*. Cambridge University Press, 2006. URL `https://www.cambridge.org/gb/academic/subjects/mathematics/differential-and-integral-equations-dynamical-systems-and-co/multiple-scattering-interaction-time-harmonic-waves-ini-obstacles?format=HB&isbn=9780521865548`.

[36] CM Linton and PA Martin. Multiple scattering by random configurations of circular cylinders: Second-order corrections for the effective wavenumber. *The Journal of the Acoustical Society of America*, 117(6):3413–3423, 2005. URL `https://doi.org/10.1121/1.1904270`.

[37] SK Kanaun, VM Levin, and FJ Sabina. Propagation of elastic waves in composites with random set of spherical inclusions (effective medium approach). *Wave motion*, 40(1):69–88, 2004. URL `https://doi.org/10.1016/j.wavemoti.2003.12.013`.

[38] L Hinke, L Pichler, HJ Pradlwarter, BR Mace, and TP Waters. Modelling of spatial variations in vibration analysis with application to an automotive windshield. *Finite Elements in Analysis and Design*, 47(1):55–62, 2011. ISSN 0168-874X. URL `https://www.sciencedirect.com/science/article/pii/S0168874X10001174`.

[39] L Hinke, L Pichler, HJ Pradlwarter, BR Mace, and TP Waters. A random field model for a laminate windshield. In *Ninth International Conference on Recent Advances in Structural Dynamics*, 2006. URL `https://eprints.soton.ac.uk/42296/`.

[40] EJ Heller, R Fleischmann, and T Kramer. Branched flow. *Physics Today*, 74(12): 44–51, 2021. URL `https://doi.org/10.1063/PT.3.4902`.

[41] EJ Heller. *The semiclassical way to dynamics and spectroscopy*. Princeton University Press, 2018. ISBN 9781400890293. URL `https://press.princeton.edu/books/ebook/9781400890293/the-semiclassical-way-to-dynamics-and-spectroscopy`.

[42] VA Kulkarny and BS White. Focusing of waves in turbulent inhomogeneous media. *Physics of Fluids*, 25(10):1770–1784, 1982. ISSN 10706631. doi: 10.1063/1.863654. URL `https://doi.org/10.1063/1.863654`.

[43] A Pidwerbetsky. *Simulation and Analysis of Wave Propagation Through Random Media*. PhD thesis, Cornell University, New York, December 1988. URL `https://www.proquest.com/docview/303557295`.

[44] JM Cordes, A Pidwerbetsky, and RVE Lovelace. Refractive and diffractive scattering in the interstellar medium. *The Astrophysical Journal*, 310:737–767, 1986. URL `https://articles.adsabs.harvard.edu/pdf/1986ApJ...310..737C`.

[45] M Ewing and LJ Worzel. LONG-RANGE SOUND TRANSMISSION. In *Propagation of Sound in the Ocean*. Geological Society of America, 01 1948. ISBN 9780813710273. doi: 10.1130/MEM27-3-p1. URL `https://doi.org/10.1130/MEM27-3-p1`.

[46] R Dashen, WH Munk, KM Watson, and F Zachariasen. *Sound transmission through a fluctuating ocean*. Cambridge University Press, 2010. URL `https://www.cambridge.org/gb/academic/subjects/mathematics/fluid-dynamics-and-solid-mechanics/sound-transmission-through-fluctuating-ocean?format=PB&isbn=9780521142458`.

[47] JA Colosi, SM Flatte, and C Bracher. Internal-wave effects on 1000-km oceanic acoustic pulse propagation: Simulation and comparison with experiment. *The Journal of the Acoustical Society of America*, 96(1):452–468, 1994. URL `https://doi.org/10.1121/1.411331`.

[48] MA Wolfson and S Tomsovic. On the stability of long-range sound propagation through a structured ocean. *The Journal of the Acoustical Society of America*, 109(6): 2693–2703, 2001. ISSN 0001-4966. URL `https://doi.org/10.1121/1.1362685`.

[49] H Degueldre, JJ Metzger, T Geisel, and R Fleischmann. Random focusing of tsunami waves. *Nature Physics*, 12(3):259–262, 2016. ISSN 17452481. URL `https://doi.org/10.1038/nphys3557`.

[50] A Patsyk, U Sivan, M Segev, and MA Bandres. Observation of branched flow of light. *Nature*, 583(7814):60–65, 2020. ISSN 14764687. URL `https://doi.org/10.1038/s41586-020-2376-8`.

[51] R Höhmann, U Kuhl, H.-J Stöckmann, L Kaplan, and EJ Heller. Freak waves in the linear regime: A microwave study. *Phys. Rev. Lett.*, 104:093901, 3 2010. URL `https://doi.org/10.1103/PhysRevLett.104.093901`.

[52] JJ Metzger, R Fleischmann, and T Geisel. Statistics of extreme waves in random media. *Physical Review Letters*, 112(20):1–5, 2014. ISSN 10797114. URL `https://doi.org/10.1103/PhysRevLett.112.203903`.

[53] JJ Metzger, R Fleischmann, and T Geisel. Universal statistics of branched flows. *Physical Review Letters*, 105(2):1–4, 2010. ISSN 00319007. doi: 10.1103/PhysRevLett.105.020601. URL `https://doi.org/10.1103/PhysRevLett.105.020601`.

[54] L Kaplan. Statistics of Branched Flow in a Weak Correlated Random Potential. *Physical Review Letters*, 89(18):9–12, 2002. ISSN 10797114. doi: 10.1103/PhysRevLett.89.184103. URL `https://doi.org/10.1103/PhysRevLett.89.184103`.

[55] Gerrit Green and Ragnar Fleischmann. Branched flow and caustics in nonlinear waves. *New Journal of Physics*, 21(8):083020, 8 2019. doi: 10.1088/1367-2630/ab319b. URL `https://doi.org/10.1088/1367-2630/ab319b`.

[56] H Degueldre, JJ Metzger, E Schultheis, and R Fleischmann. Channeling of branched flow in weakly scattering anisotropic media. *Physical Review Letters*, 118(2):024301, 2017. URL `https://doi.org/10.1103/PhysRevLett.118.024301`.

[57] A Brandstötter, A Girschik, P Ambichl, and S Rotter. Shaping the branched flow of light through disordered media. *Proceedings of the National Academy of Sciences*, 116(27):13260–13265, 2019. doi: 10.1073/pnas.1905217116. URL `https://www.pnas.org/doi/abs/10.1073/pnas.1905217116`.

[58] A Daza, EJ Heller, AM Graf, and E Räsänen. Propagation of waves in high brillouin zones: Chaotic branched flow and stable superwires. *Proceedings of the National Academy of Sciences*, 118(40):e2110285118, 2021. URL `https://doi.org/10.1073/pnas.2110285118`.

[59] D Kim and EJ Heller. Bragg scattering from a random potential. *Phys. Rev. Lett.*, 128:200402, May 2022. doi: 10.1103/PhysRevLett.128.200402. URL `https://link.aps.org/doi/10.1103/PhysRevLett.128.200402`.

[60] AA Jafari and M Bagheri. Free vibration of rotating ring stiffened cylindrical shells with non-uniform stiffener distribution. *Journal of sound and vibration*, 296 (1-2):353–367, 2006. URL `https://doi.org/10.1016/j.jsv.2006.03.001`.

[61] AA Lakis and MP Paidoussis. Dynamic analysis of axially non-uniform thin cylindrical shells. *Journal of Mechanical Engineering Science*, 14(1):49–71, 1972. URL `https://doi.org/10.1243/JMES_JOUR_1972_014_009_02`.

[62] LH Donnell. Stability of thin-walled tubes under torsion. Technical report, National Advisory Committee for Aeronautics/NASA, 1935. URL `https://ntrs.nasa.gov/citations/19930091553`.

[63] AW Leissa. Vibration of shells. Technical report, National Advisory Committee for Aeronautics/NASA, 1973. URL `https://ntrs.nasa.gov/citations/19730018197`.

[64] J Kaplunov, L Kossovitch, and E Nolde. *Dynamics of thin walled elastic bodies*. Academic Press, 1998.

[65] S Germain. *Recherches sur la théorie des surfaces élastiques*. V. Courcier, 1821. URL `https://www.cambridge.org/gb/academic/subjects/mathematics/mathematical-physics/recherches-sur-la-theorie-des-surfaces-elastiques?format=PB&isbn=9781108050371`.

[66] D Ullmann. Life and work of EFF chladni. *The European Physical Journal Special Topics*, 145(1):25–32, 2007. URL `https://link.springer.com/article/10.1140/epjst/e2007-00145-4`.

[67] SS Rao. *Vibration of continuous systems*. John Wiley & Sons, 2019. ISBN 9780470117866. URL `https://onlinelibrary.wiley.com/doi/book/10.1002/9780470117866`.

[68] CJ Chapman and SV Sorokin. A wronskian method for elastic waves propagating along a tube. *Proceedings of the Royal Society A*, 477(2250):20210202, 2021. URL `https://doi.org/10.1098/rspa.2021.0202`.

[69] SV Sorokin and CJ Chapman. Reduced-order modelling of wave propagation in an elastic layer of constant curvature and thickness. *Journal of Sound and Vibration*, 433:248–264, 2018. URL `https://doi.org/10.1016/j.jsv.2018.07.018`.

[70] JW Strutt. On the scattering of light by small particles. *The London, Edinburgh, and Dublin Philosophical Magazine and Journal of Science*, 41(275):447–454, 1871. doi: 10.1080/14786447108640507. URL `https://doi.org/10.1080/14786447108640507`.

[71] JW Strutt. On the electromagnetic theory of light. *The London, Edinburgh, and Dublin Philosophical Magazine and Journal of Science*, 12(73):81–101, 1881. doi: 10.1080/14786448108627074. URL `https://doi.org/10.1080/14786448108627074`.

[72] R-S Wu and K Aki. Scattering characteristics of elastic waves by an elastic heterogeneity. *Geophysics*, 50(4):582–595, 1985. URL `https://doi.org/10.1190/1.1441934`.

[73] JW Strutt. On the light from the sky, its polarization and colour. *The London, Edinburgh, and Dublin Philosophical Magazine and Journal of Science*, 41(271): 107–120, 1871. doi: 10.1080/14786447108640452. URL `https://doi.org/10.1080/14786447108640452`.

[74] JW Strutt. On the light from the sky, its polarization and colour. *The London, Edinburgh, and Dublin Philosophical Magazine and Journal of Science*, 41(273): 274–279, 1871. doi: 10.1080/14786447108640479. URL `https://doi.org/10.1080/14786447108640479`.

[75] JW Strutt. On the transmission of light through an atmosphere containing small particles in suspension, and on the origin of the blue of the sky. *The London, Edinburgh, and Dublin Philosophical Magazine and Journal of Science*, 47(287): 375–384, 1899. doi: 10.1080/14786449908621276. URL `https://doi.org/10.1080/14786449908621276`.

[76] D Jackèl and B Walter. Modeling and rendering of the atmosphere using mie-scattering. *Computer Graphics Forum*, 16(4):201–210, 1997. doi: 10.1111/1467-8659.00180. URL `https://onlinelibrary.wiley.com/doi/abs/10.1111/1467-8659.00180`.

[77] Allan D. Pierce. Spikes on sonic-boom pressure waveforms. *The Journal of the Acoustical Society of America*, 44(4):1052–1061, 1968. doi: 10.1121/1.1911195. URL `https://doi.org/10.1121/1.1911195`.

[78] H-J Stöckmann. Chladni meets Napoleon. *The European Physical Journal Special Topics*, 145(1):15–23, 2007. URL `https://link.springer.com/article/10.1140/epjst/e2007-00144-5`.

[79] EFF Chladni. *Entdeckungen über die Theorie des Klanges*. Zentralantiquariat der DDR, 1787.

[80] TT Wu, ZG Huang, TC Tsai, and TC Wu. Evidence of complete band gap and resonances in a plate with periodic stubbed surface. *Applied Physics Letters*, 93 (11), 2008. ISSN 00036951. doi: 10.1063/1.2970992. URL `https://doi.org/10.1063/1.2970992`.

[81] Y Pennec, B Djafari-Rouhani, H Larabi, JO Vasseur, and AC Hladky-Hennion. Low-frequency gaps in a phononic crystal constituted of cylindrical dots deposited on a thin homogeneous plate. *Physical Review B - Condensed Matter and Materials Physics*, 78(10):1–8, 2008. ISSN 10980121. doi: 10.1103/PhysRevB.78.104105. URL `https://doi.org/10.1103/PhysRevB.78.104105`.

[82] K Yu, T Chen, and X Wang. Band gaps in the low-frequency range based on the two-dimensional phononic crystal plates composed of rubber matrix with

periodic steel stubs. *Physica B: Condensed Matter*, 416:12–16, 2013. ISSN 09214526. doi: 10.1016/j.physb.2013.02.011. URL `http://dx.doi.org/10.1016/j.physb.2013.02.011`.

[83] M Oudich, M Badreddine Assouar, and Z Hou. Propagation of acoustic waves and waveguiding in a two-dimensional locally resonant phononic crystal plate. *Applied Physics Letters*, 97(19):2008–2011, 2010. ISSN 00036951. doi: 10.1063/1.3513218. URL `https://doi.org/10.1063/1.3513218`.

[84] M Badreddine Assouar, M Senesi, M Oudich, M Ruzzene, and Z Hou. Broadband plate-type acoustic metamaterial for low-frequency sound attenuation. *Applied Physics Letters*, 101(17):1–5, 2012. ISSN 00036951. doi: 10.1063/1.4764072. URL `https://doi.org/10.1063/1.4764072`.

[85] M Oudich, Y Li, M Badreddine Assouar, and Z Hou. A sonic band gap based on the locally resonant phononic plates with stubs. *New Journal of Physics*, 12(8): 083049, 8 2010. doi: 10.1088/1367-2630/12/8/083049. URL `https://doi.org/10.1088/1367-2630/12/8/083049`.

[86] M Badreddine Assouar and M Oudich. Enlargement of a locally resonant sonic band gap by using double-sides stubbed phononic plates. *Applied Physics Letters*, 100(12), 2012. ISSN 00036951. doi: 10.1063/1.3696050. URL `https://doi.org/10.1063/1.3696050`.

[87] HJ Zhao, HW Guo, Bing Y Li, ZQ Deng, and RQ Liu. Flexural vibration band gaps in a double-side phononic crystal plate. *Journal of Applied Physics*, 118(4), 2015. ISSN 10897550. doi: 10.1063/1.4927627. URL `http://dx.doi.org/10.1063/1.4927627`.

[88] G Ma and P Sheng. Acoustic metamaterials: From local resonances to broad horizons. *Science Advances*, 2(2), 2016. ISSN 23752548. doi: 10.1126/sciadv.1501595. URL `https://doi.org/10.1126/sciadv.1501595`.

[89] SA Cummer, J Christensen, and A Alù. Controlling sound with acoustic metamaterials. *Nature Reviews Materials*, 1(3):16001, 2016. URL `https://www.nature.com/articles/natrevmats20161`.

[90] GS Mishuris, AB Movchan, and LI Slepyan. Waves in elastic bodies with discrete and continuous dynamic microstructure. *Philosophical Transactions of the Royal Society A*, 378(2162):20190313, 2020. URL `https://doi.org/10.1098/rsta.2019.0313`.

[91] J Munkres. Algorithms for the assignment and transportation problems. *Journal of the society for industrial and applied mathematics*, 5(1):32–38, 1957. URL `https://www.jstor.org/stable/2098689`.

[92] M Ali, A Ul-Hamid, LM Alhems, and A Saeed. Review of common failures in heat exchangers – Part I: Mechanical and elevated temperature failures. *Engineering Failure Analysis*, 109:104396, 2020. ISSN 1350-6307. doi: 10.1016/j.engfailanal.2020.104396. URL `https://www.sciencedirect.com/science/article/pii/S1350630718313852`.

[93] J Lai, T Tan, S Yang, L Lu, L Sun, and H Ming. Flow-induced vibration of tube bundles considering the effect of periodic fluid force in a rotated triangular tube array. *Annals of Nuclear Energy*, 161:108488, 2021. URL `https://doi.org/10.1016/j.anucene.2021.108488`.

[94] WA Mair and RKW Palmer. Vortex shedding from finned tubes. *Journal of Sound and Vibration*, 39(3):293–296, 1975. URL `https://doi.org/10.1016/S0022-460X(75)80082-4`.

[95] DS Weaver and JA Fitzpatrick. A review of cross-flow induced vibrations in heat exchanger tube arrays. *Journal of fluids and structures*, 2(1):73–93, 1988. URL `https://doi.org/10.1016/S0889-9746(88)90137-5`.

[96] E Longatte, F Baj, Y Hoarau, M Braza, D Ruiz, and C Canteneur. Advanced numerical methods for uncertainty reduction when predicting heat exchanger dynamic stability limits: review and perspectives. *Nuclear Engineering and Design*, 258:164–175, 2013. URL `https://doi.org/10.1016/j.nucengdes.2012.12.003`.

[97] L Chen. Curse of dimensionality. In L Liu and MT Özsu, editors, *Encyclopedia of Database Systems*, pages 717–718. Springer New York, New York, NY, 2018. ISBN 978-1-4614-8265-9. doi: 10.1007/978-1-4614-8265-9_133. URL `https://doi.org/10.1007/978-1-4614-8265-9_133`.

[98] V Babich and A Kiselev. *Elastic waves: high frequency theory*. CRC Press, 2018.

[99] LD Landau, EM Lifšic, EM Lifshitz, AM Kosevich, and LP Pitaevskii. *Theory of elasticity: volume 7*, volume 7. Elsevier, 1986. URL `https://doi.org/10.1016/C2009-0-25521-8`.

[100] AEH Love. The small free vibrations and deformation of a thin elastic shell. *Philosophical Transactions of the Royal Society of London.(A.)*, 179:491–546, 1888. URL `https://doi.org/10.1098/rsta.1888.0016`.

[101] RD Mindlin. Influence of Rotatory Inertia and Shear on Flexural Motions of Isotropic, Elastic Plates. *Journal of Applied Mechanics*, 18(1):31–38, 04 2021. ISSN 0021-8936. doi: 10.1115/1.4010217. URL `https://doi.org/10.1115/1.4010217`.

[102] AL Goldenveizer, JD Kaplunov, and EV Nolde. On timoshenko-reissner type theories of plates and shells. *International Journal of Solids and Structures*, 30(5): 675–694, 1993.

[103] AW Leissa. Vibration of plates. Technical report, National Advisory Committee for Aeronautics/NASA, 1969. URL `https://ntrs.nasa.gov/citations/19700009156`.

[104] AD Pierce. Physical Interpretation of the WKB or Eikonal Approximation for Waves and Vibrations in Inhomogeneous Beams and Plates. *The Journal of the Acoustical Society of America*, 48(1B):275–284, 1970. ISSN 0001-4966. doi: 10.1121/1.1912125. URL `https://doi.org/10.1121/1.1912125`.

[105] H-P Degueldre. *Random Focusing of Tsunami Waves*. PhD thesis, Georg-August-Universitat Gottingen, 2015. URL `http://dx.doi.org/10.53846/goediss-5365`.

[106] PW Anderson. Absence of diffusion in certain random lattices. *Physical Review*, 109(5):1492–1505, 1958. ISSN 0031899X. doi: 10.1103/PhysRev.109.1492. URL `https://doi.org/10.1103/PhysRev.109.1492`.

[107] Z Liu, X Zhang, Y Mao, YY Zhu, Z Yang, CT Chan, and P Sheng. Locally resonant sonic materials. *Science*, 289(5485):1734–1736, 2000. doi: 10.1126/science.289.5485.1734. URL `https://www.science.org/doi/10.1126/science.289.5485.1734`.

[108] A Colombi, P Roux, S Guenneau, and M Rupin. Directional cloaking of flexural waves in a plate with a locally resonant metamaterial. *The Journal of the Acoustical Society of America*, 137(4):1783–1789, 2015. URL `https://doi.org/10.1121/1.4915004`.

[109] Matthieu Rupin, Fabrice Lemoult, Geoffroy Lerosey, and Philippe Roux. Experimental demonstration of ordered and disordered multiresonant metamaterials for Lamb waves. *Phys. Rev. Lett.*, 112:234301, 2014. doi: 10.1103/PhysRevLett.112.234301. URL `https://link.aps.org/doi/10.1103/PhysRevLett.112.234301`.

[110] L Ryzhik, G Papanicolaou, and JB Keller. Transport equations for elastic and other waves in random media. *Wave Motion*, 24(4):327–370, 1996. ISSN 0165-2125. doi: 10.1016/S0165-2125(96)00021-2. URL `https://www.sciencedirect.com/science/article/pii/S0165212596000212`.

[111] E Reissner. The Effect of Transverse Shear Deformation on the Bending of Elastic Plates. *Journal of Applied Mechanics*, 12(2):A69–A77, 03 2021. ISSN 0021-8936. doi: 10.1115/1.4009435. URL `https://doi.org/10.1115/1.4009435`.

[112] JW Strutt. *The Theory of Sound*, volume 2 of *Cambridge Library Collection - Physical Sciences*. Cambridge University Press, 2011. doi: 10.1017/CBO9781139058094. URL `https://doi.org/10.1017/CBO9781139058094`.

[113] SP Timoshenko. On the transverse vibrations of bars of uniform cross-section. *The London, Edinburgh, and Dublin Philosophical Magazine and Journal of Science*, 43 (253):125–131, 1922. URL `https://www.tandfonline.com/doi/abs/10.1080/14786442208633855`.

[114] T von Kármán. Festigkeitsprobleme im maschinenbau. In *Mechanik*, pages 311–385. Springer, 1907. URL `https://link.springer.com/chapter/10.1007/978-3-663-16028-1_5`.

[115] J. Náprstek and R. Král. Multi-dimensional Fokker-Planck equation analysis using the modified finite element method. *Journal of Physics: Conference Series*, 744(1), 2016. ISSN 17426596. doi: 10.1088/1742-6596/744/1/012177.

[116] JJ Metzger. *Branched Flow and Caustics in Two-Dimensional Random Potentials and Magnetic Fields*. PhD thesis, Georg-August-University Goettingen, 2010. URL `http://dx.doi.org/10.53846/goediss-2917`.

[117] S Barkhofen, JJ Metzger, R Fleischmann, U Kuhl, and HJ Stöckmann. Experimental observation of a fundamental length scale of waves in random media. *Physical Review Letters*, 111(18):1–5, 2013. ISSN 00319007. doi: 10.1103/PhysRevLett.111.183902. URL `https://doi.org/10.1103/PhysRevLett.111.183902`.

[118] ANSYS, Inc. Ansys academic research mechanical, 2020. Release 20.2.

[119] NM Newmark. A method of computation for structural dynamics. *Journal of the engineering mechanics division*, 85(3):67–94, 1959. URL `https://ascelibrary.org/doi/10.1061/JMCEA3.0000098`.

[120] T-Y Huang, C Shen, and Y Jing. Membrane-and plate-type acoustic metamaterials. *The Journal of the Acoustical Society of America*, 139(6):3240–3250, 2016. URL `https://doi.org/10.1121/1.4950751`.

[121] AG Guex, N Di Marzio, D Eglin, M Alini, and T Serra. The waves that make the pattern: A review on acoustic manipulation in biomedical research. *Materials Today Bio*, 10:100110, 2021. URL `https://doi.org/10.1016/j.mtbio.2021.100110`.

[122] LH Donnell. A discussion of thin shell theory. In *Proceedings of the 5th International Congress of Applied Mechanics*, pages 66–70. John Wiley New York, 1938.

[123] KM Mushtari. Certain generalizations of the theory of thin shells. *Izv. Fiz. Mat. Ob-va. Pri Kaz. Un-te*, 11(8):28–56, 1938.

[124] KM Mushtari. On the stability of cylindrical shells subjected to torsion. *Trudy Kazanskego aviatsionnugo inatituta*, 2, 1938.

[125] AEH Love. *A treatise on the mathematical theory of elasticity*. Cambridge university press, 2013. URL `https://www.cambridge.org/gb/academic/subjects/mathematics/historical-mathematical-texts/treatise-mathematical-theory-elasticity-4th-edition?format=PB&isbn=9781107618091`.

[126] S Timoshenko and S Woinowsky-Krieger. *Theory of plates and shells*, volume 2. McGraw-hill New York, 1959.

[127] E Reissner. A new derivation of the equations for the deformation of elastic shells. *American Journal of Mathematics*, 63(1):177–184, 1941. URL `https://doi.org/10.2307/2371288`.

[128] PM Naghdi and JG Berry. On the Equations of Motion of Cylindrical Shells. *Journal of Applied Mechanics*, 21(2):160–166, 06 2021. ISSN 0021-8936. doi: 10.1115/1.4010859. URL `https://doi.org/10.1115/1.4010859`.

[129] VZ Vlasov. Basic differential equations in general theory of elastic shells. *Prikladnaia Matematika I Mekhanika*, 8, 1951. URL `https://ntrs.nasa.gov/citations/20050028489`.

[130] VZ Vlasov. General theory of shells and its application in engineering. 1964.

[131] Yi-Yuan Yu. Free Vibrations of Thin Cylindrical Shells Having Finite Lengths With Freely Supported and Clamped Edges. *Journal of Applied Mechanics*, 22(4): 547–552, 1955. ISSN 0021-8936.

[132] W Soedel. *Vibrations of shells and plates*. CRC Press, 2004. ISBN 9780429216275. URL `https://doi.org/10.4324/9780203026304`.

[133] JE Greenspon. Vibrations of a thick-walled cylindrical shell— comparison of the exact theory with approximate theories. *The Journal of the Acoustical Society of America*, 32(5):571–578, 1960. URL `https://doi.org/10.1121/1.1908148`.

[134] Y-Y Yu. Vibrations of thin cylindrical shells analyzed by means of Donnell-type equations. *Journal of the Aerospace Sciences*, 25(11):699–715, 1958. URL `https://doi.org/10.2514/8.7849`.

[135] PM Naghdi and RM Cooper. Propagation of elastic waves in cylindrical shells, including the effects of transverse shear and rotatory inertia. *The Journal of the Acoustical Society of America*, 28(1):56–63, 1956. URL `https://doi.org/10.1121/1.1908222`.

[136] AN Norris and DA Rebinsky. Membrane and Flexural Waves on Thin Shells. *Journal of Vibration and Acoustics*, 116(4):457–467, 10 1994. ISSN 1048-9002. URL `https://doi.org/10.1115/1.2930449`.

[137] AD Pierce. Wave propagation on thin-walled elastic cylindrical shells. In MF McCarthy and MA Hayes, editors, *Elastic Wave Propagation*, volume 35 of *North-Holland Series in Applied Mathematics and Mechanics*, pages 205–210. North-Holland, 1989. URL `https://doi.org/10.1016/B978-0-444-87272-2.50034-8`.

[138] VV Bolotin. *Random vibrations of elastic systems*, volume 8. Springer Science & Business Media, 2013. URL `https://doi.org/10.1007/978-94-017-2842-3`.

[139] XM Zhang, GR Liu, and KY Lam. Vibration analysis of thin cylindrical shells using wave propagation approach. *Journal of Sound and Vibration*, 239(3):397–403, 2001. ISSN 0022-460X. URL `https://doi.org/10.1006/jsvi.2000.3139`.

[140] F Pellicano. Vibrations of circular cylindrical shells: Theory and experiments. *Journal of Sound and Vibration*, 303(1):154–170, 2007. ISSN 0022-460X. URL `https://doi.org/10.1016/j.jsv.2007.01.022`.

[141] N Ege, B Erbaş, J Kaplunov, and N Noori. Asymptotic corrections to the low-frequency theory for a cylindrical elastic shell. *Zeitschrift für angewandte Mathematik und Physik*, 74(2):43, 2023.

[142] N Ege, B Erbaş, J Kaplunov, and N Noori. Low-frequency vibrations of a thin-walled functionally graded cylinder (plane strain problem). *Mechanics of Advanced Materials and Structures*, 30(6):1172–1180, 2023.

[143] J Kaplunov, LI Manevitch, and VV Smirnov. Vibrations of an elastic cylindrical shell near the lowest cut-off frequency. *Proceedings of the Royal Society A: Mathematical, Physical and Engineering Sciences*, 472(2189):20150753, 2016.

[144] JO Morsbøl, SV Sorokin, and N Peake. A wkb approximation of elastic waves travelling on a shell of revolution. *Journal of Sound and Vibration*, 375:162–186, 2016. ISSN 0022-460X. URL `https://doi.org/10.1016/j.jsv.2016.04.001`.

[145] AN Norris. Rays, beams and quasimodes on thin shell structures. *Wave Motion*, 21(2):127–147, 1995. ISSN 0165-2125. URL `https://doi.org/10.1016/0165-2125(94)00048-A`.

[146] G Green and R Fleischmann. Branched flow and caustics in nonlinear waves. *New Journal of Physics*, 21(8):083020, 2019. URL `https://doi.org/10.1088/1367-2630/ab319b`.

[147] AD Pierce. Variational formulations in acoustic radiation and scattering. In AD Pierce and RN Thurston, editors, *Physical Acoustics*, volume 22 of *Physical*

Acoustics, pages 195–371. Academic Press, 1993. doi: 10.1016/B978-0-12-477922-8.50007-8. URL `https://www.sciencedirect.com/science/article/pii/B9780124779228500078`.

[148] H Risken. *Fokker-planck equation*. Springer, 1996. ISBN 978-3-642-61544-3. URL `https://doi.org/10.1007/978-3-642-61544-3`.

[149] CM Hutchins. The acoustics of violin plates. *Scientific American*, 245(4):170–187, 1981. URL `https://www.scientificamerican.com/article/the-acoustics-of-violin-plates/`.

[150] IM Firth. Physics of the guitar at the helmholtz and first top-plate resonances. *The Journal of the Acoustical Society of America*, 61(2):588–593, 1977. URL `https://doi.org/10.1121/1.381302`.

[151] CV Raman. The indian musical drums. In *Proceedings of the Indian Academy of Sciences-Section A*, volume 1, pages 179–188. Springer, 1934. URL `https://link.springer.com/article/10.1007/BF03035705`.

[152] N-E Molin and L Zipser. Optical methods of today for visualizing sound fields in musical acoustics. *Acta Acustica united with Acustica*, 90(4):618–628, 2004. ISSN 1610-1928. URL `https://www.ingentaconnect.com/content/dav/aaua/2004/00000090/00000004/art00006`.

[153] I Solodov, D Derusova, and M Rahammer. Thermosonic chladni figures for defect-selective imaging. *Ultrasonics*, 60:1–5, 2015. URL `https://doi.org/10.1016/j.ultras.2015.02.007`.

[154] RL Powell and KA Stetson. Interferometric vibration analysis by wavefront reconstruction. *Journal of the Optical Society of America*, 55(12):1593–1598, Dec 1965. doi: 10.1364/JOSA.55.001593. URL `https://doi.org/10.1364/JOSA.55.001593`.

[155] D Afolabi. A note on the rogue failure of turbine blades. *Journal of Sound and Vibration*, 122(3):535–545, 1988. ISSN 10958568. doi: 10.1016/S0022-460X(88)80100-7. URL `https://doi.org/10.1016/S0022-460X(88)80100-7`.

[156] M Pastor, M Binda, and T Harčarik. Modal assurance criterion. *Procedia Engineering*, 48:543–548, 2012. URL `https://doi.org/10.1016/j.proeng.2012.09.551`.

[157] HW Kuhn. The hungarian method for the assignment problem. *Naval research logistics quarterly*, 2(1-2):83–97, 1955. URL `https://doi.org/10.1002/nav.3800020109`.

[158] A Parrinello and GL Ghiringhelli. Modal density of rectangular structures in a wide frequency range. *Journal of Sound and Vibration*, 419:380–389, 2018. ISSN 0022-460X. doi: 10.1016/j.jsv.2018.01.030. URL `https://www.sciencedirect.com/science/article/pii/S0022460X18300385`.

[159] D Zenkert. *The handbook of sandwich construction*. Engineering Materials Advisory Services, 1997. URL `https://www.diva-portal.org/smash/get/diva2:1366187/FULLTEXT01.pdf`.

[160] J Alman and VV Williams. A refined laser method and faster matrix multiplication. In *Proceedings of the 2021 ACM-SIAM Symposium on Discrete Algorithms (SODA)*, pages 522–539. SIAM, 2021. URL `https://doi.org/10.1137/1.9781611976465.32`.

[161] PA Deymier. *Acoustic Metamaterials and Phononic Crystals*, volume 173 of *Springer Series in Solid-State Sciences*. Springer Berlin Heidelberg, Berlin, Heidelberg, 2013. ISBN 9783642312328. doi: 10.1007/978-3-642-31232-8. URL `https://doi.org/10.1007/978-3-642-31232-8`.

[162] R Martínez-Sala, J Sancho, JV Sánchez, V Gómez, J Llinares, and F Meseguer. Sound attenuation by sculpture. *Nature*, 378(6554):241, 1995. URL `https://doi.org/10.1038/378241a0`.

[163] JU Surjadi, L Gao, H Du, X Li, X Xiong, NX Fang, and Y Lu. Mechanical metamaterials and their engineering applications. *Advanced Engineering Materials*, 21(3):1800864, 2019. doi: 10.1002/adem.201800864. URL `https://onlinelibrary.wiley.com/doi/abs/10.1002/adem.201800864`.

[164] N Gao, Z Zhang, J Deng, X Guo, B Cheng, and H Hou. Acoustic metamaterials for noise reduction: A review. *Advanced Materials Technologies*, 7(6):2100698, 2022. doi: 10.1002/admt.202100698. URL `https://onlinelibrary.wiley.com/doi/abs/10.1002/admt.202100698`.

[165] Y Jin, Y Pennec, B Bonello, H Honarvar, L Dobrzynski, B Djafari-Rouhani, and MI Hussein. Physics of surface vibrational resonances: pillared phononic crystals, metamaterials, and metasurfaces. *Reports on Progress in Physics*, 84(8): 086502, sep 2021. doi: 10.1088/1361-6633/abdab8. URL `https://dx.doi.org/10.1088/1361-6633/abdab8`.

[166] CH Hodges and J Woodhouse. Vibration isolation from irregularity in a nearly periodic structure: Theory and measurements. *The Journal of the Acoustical Society of America*, 74(3):894–905, 1983. URL `https://doi.org/10.1121/1.389847`.

[167] CH Hodges and J Woodhouse. Confinement of vibration by one-dimensional disorder, II: A numerical experiment on different ensemble averages. *Journal of*

Sound and Vibration, 130(2):253–268, 1989. ISSN 0022-460X. doi: 10.1016/0022-460X(89)90553-1. URL https://www.sciencedirect.com/science/article/pii/0022460X89905531.

[168] CH Hodges and J Woodhouse. Confinement of vibration by one-dimensional disorder, I: Theory of ensemble averaging. *Journal of Sound and Vibration*, 130(2): 237–251, 1989. ISSN 0022-460X. doi: 10.1016/0022-460X(89)90552-X. URL https://www.sciencedirect.com/science/article/pii/0022460X8990552X.